Josef Ehgartner, M.Sc.

Development of luminescent oxygen and pH sensors for microfluidic applications

DISSERTATION

zur Erlangung des akademischen Grades
Doktor der technischen Wissenschaft
eingereicht an der
Technischen Universität Graz

Betreuer

Assoc.Prof. Dipl.-Chem. Dr.rer.nat. Torsten Mayr
Institut für Analytische Chemie und Lebensmittelchemie
Technische Universität Graz

Graz, September 2016

II

"An infrared photon walks into a bar and says is it hot in here or is it just me."

Brian Malow

IV

EIDESSTATTLICH ERKLÄRUNG

Ich erkläre an Eides statt, dass ich die vorliegende Arbeit selbstständig verfasst, andere als die angegebenen Quellen/Hilfsmittel nicht benutzt, und die den benutzten Quellen wörtlich und inhaltlich entnommenen Stellen als solche kenntlich gemacht habe. Das in TUGRAZonline hochgeladene Textdokument ist mit der vorliegenden Dissertation identisch.

Graz, am ....
                                                                (Unterschrift)

AFFIDAVIT

I declare that I have authored this thesis independently, that I have not used other than the declared sources/resources, and that I have explicitly indicated all material which has been quoted either literally or by content from the sources used. The text document uploaded to TUGRAZonline is identical to the present doctoral thesis.

Graz, ...
                                                                (Signature)

Kurzfassung Mikrofluidische Systeme eröffnen neue Möglichkeiten in der Entwicklung analytischer Geräte, Nanomaterialien und der Zellkultivierung. Das wissenschaftliche Vorankommen ist allerdings oftmals erschwert, da zuverlässige und miniaturisierte Sensorsysteme in diesen Bereichen dringend benötigt werden, aber selten vorhanden sind. Aufgrund dieser Tatsache wurden auf Lumineszenz basierende Sensorsysteme entwickelt. Die Sensoren sind mit langwelligem Licht (> 600 nm) anregbar, emittieren im nahen Infrarot und können zur Bestimmung der Sauerstoffkonzentration und des pH Werts eingesetzt werden. Sie bieten den Vorteil, dass sie eine hohe Helligkeit, eine hohe Fotostabilität und ein schnelles Ansprechen aufweisen. Zudem ist langwelliges Licht weniger schädlich für Zellen als UV Strahlung oder blaues Licht. Dies ist vorteilhaft, da pH- und Sauerstoffsensoren vor allem in Zellkulturen benötigt werden. Das erste entwickelte Sensorsystem erlaubt die Bestimmung von gelöstem Sauerstoff in mikrofluidischen Geräten und besteht aus integrierten Sensorschichten, die über ein Messgerät basierend auf Lebenszeitmessungen der Lumineszenz in der Frequenzdomäne ausgelesen werden. Der Sauerstoffgehalt kann mit einer Auflösung von 0.06-0.22 hPa (entspricht ca. 3 – 9 µg/L gelöstem Sauerstoff) bestimmt werden. Ein auf diesem Sensor basierender und weiterentwickelter Sensor wurde zur Bestimmung des Sauerstoffgehalts in einem Leber-am-Chip System und einem mikrofluidischen Biosensor zur Detektion von Pestiziden eingesetzt. Das zweite entwickelte Sensorsystem besteht aus Sauerstoff und pH empfindlichen Nanosensoren, die über ein miniaturisiertes Messgerät ausgelesen werden, das simultan die Sauerstoffkonzentration und den pH Wert bestimmen kann. Hierzu wurde ein Messalgorithmus entwickelt. Der Sauerstoffgehalt kann mit einer Auflösung zwischen 0.5-8.0 hPa (entspricht ca. 0.02-0.32 mg/L) je nach vorhandener Sauerstoffkonzentration bestimmt werden. Der pH Wert lässt sich innerhalb des dynamischen Bereichs der pH Nanosensoren zwischen pH 6 und pH 9 mit einer Auflösung von 0.03-0.1 pH Einheiten bestimmen. Die Nanosensoren wurden in einem weiteren Forschungsprojekt eingesetzt, das sich mit der Verfügbarkeit des Sauerstoffs in mikrofluidischen Tropfensystemen zur Zellkultivierung von industriell wichtigen Mikroorganismen beschäftigt hat. Die dritte Entwicklung ist ein bildgebendes Sensorsystem und besteht aus Sensorschichten, die über eine kombinierte 2-CCD Farb- und Nahinfrarotkamera ausgelesen werden. Die Sensoren ermöglichen Einzel- oder Doppelbestimmung der Sauerstoffkonzentration und/oder des pH Werts im sichtbaren um im nahen infraroten Spektralbereich. Ähnliche Sensoren wurden in einem anderen Forschungsprojekt eingesetzt, das die Veränderungen der Sauerstoffdurchlässigkeit von Eichenfässern während der Weinreifung untersucht hat. Die entwickelten Sensorsysteme sind wertvolle Analysegeräte, die es verschiedensten ForscherInnen ermöglichten, Antworten auf wissenschaftliche Fragestellungen zu finden.

Abstract Microfluidic systems create new possibilities for the development of analytical devices, nanomaterials and cell culture techniques. The scientific advance in these fields is often hampered because reliable and miniaturized sensor systems do not exist. This urgent need motivated us and led to the development of long-wavelength (> 600 nm) excitable and near infrared emissive luminescent sensor systems for monitoring of oxygen and/or pH in microfluidic devices. The developed sensors offer the advantage of showing a high brightness, a high photostability, a fast response and less background fluorescence or scattering from polymer chips or biological matter (cells, proteins etc.). Moreover, long-wavelength excitation is less harmful to cells in comparison to UV or blue light. This fact is of great importance for oxygen and pH sensors because both analytes are key parameters for monitoring and controlling cell growth and thus are mainly used in cell culture applications. The first developed measurement set-up allows oxygen measurements in microfluidic platforms and consists of integrated oxygen sensor films which are read out by a robust device that performs luminescent lifetime measurements in the frequency domain. The fabrication and patterning of sensor layers down to a size of 100 µm in diameter is performed via automated airbrush spraying and was used for the integration into silicon-glass microreactors. The set-up enables the determination of oxygen up to a resolution of 0.06-0.22 hPa (approx. 3 – 9 µg/L of dissolved oxygen). An adapted version of this set-up was used to determine dissolved oxygen concentrations in a liver-on-a-chip platform and in a microfluidic biosensor for pesticide detection. The second developed system consisted of oxygen and pH sensitive nanosensors and a read-out device which enables simultaneous sensing of pH and oxygen by using a modified dual lifetime referencing algorithm. The nanosensors can be used without an integration step and are of particular interest for droplet based microfluidic applications. The set-up enables the determination of oxygen up to a resolution of 0.5-8.0 hPa (approx. 0.02-0.32 mg/L of dissolved oxygen) depending on the existing oxygen levels. The pH value can be determined at a resolution of 0.03-0.1 pH units within the dynamic range of the sensors which ranges from pH 6 to pH 9. This range is an interesting measurement window for cell based applications. The nanosensors were applied in a different study to monitor the oxygen availability during the incubation of biotechnological relevant microorganisms in microfluidic droplets. The third developed system consists of planar sensor films and a 2-CCD colour near infrared camera which enables low cost ratiometric imaging of oxygen, pH and both parameters simultaneously in the visible and in the near infrared spectral region. Similar ratiometric oxygen sensors were applied in a different study to predict the oxygen diffusivity of oak wood during red wine barrel aging. All presented set-ups were valuable tools for other researchers and allowed them to answer scientifically relevant questions.

VIII

Danksagung zum Rätseln
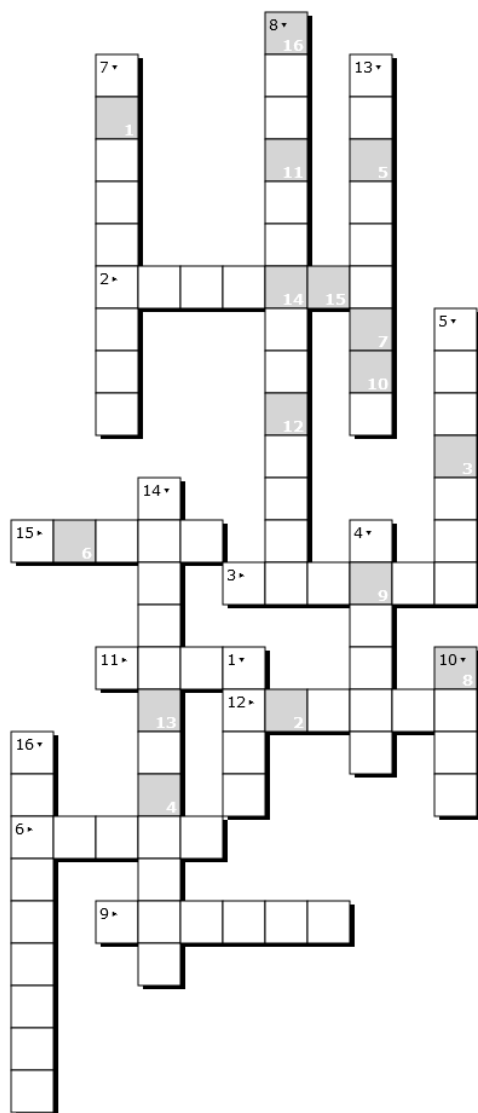
1. Das beste Team der Welt.
2. Ein verrückter Tornado der über meine Dissertation wütete.
3. Platzsparende Persönlichkeit voller Tatendrang und Liebenswürdigkeiten.
4. Jedi Meisterin und erste Anlaufstelle des jungen Padawans.
5. Freibeuter der Meere, der gerade die Gegend um die Galapagos Inseln unsicher macht.
6. Des Captains Steuermann, der kein Abenteuer und keine Reise scheut.
7. Menschlicher Teilchenbeschleuniger mit unglaublichen Fähigkeiten.
8. Österreichische Antwort auf John Lennon & Yoko Ono.
9. Deutsche Beachvolleyballgröße in Graz lebend.
10. Kochwunder im Land der lauwarmen Cervisia.
11. Liebevoller Ursprung meines Lebens.
12. Ehemalige Fußballgröße des SV Hinterbergs und nun Student.
13. Es gibt nur einen Meister, ... heißt er.
14. Was Superman & Lois Lane können, können die beiden schon lange.
15. Dieser Name steht für Zweierlei. Der eine steht auf Karpfen und der andere auf Häuser.
16. Wer dachte Garfield liebt Lasagne, hat sie noch nicht kennengelernt.

X

Danksagung (Auflösung des Rätsels)

Es ist ein großes Glück, wenn Bezeichnungen wie Arbeitskollegin oder Arbeitskollege gleichbedeutend sind mit Freundin oder Freund. Deshalb bin ich sehr froh bei euch gelandet zu sein und möchte euch allen danken. Es ist einfach herrlich mit euch gemeinsam zu arbeiten, zu lachen, zu plaudern, zu essen oder zu sporteln. Diese wunderschöne Zeit wäre allerdings nie passiert, wenn mir Torsten nicht die Möglichkeit dazu gegeben hätte. Danke lieber Tosten dafür, für deine Freundschaft, für die vielen lehrreichen Erfahrungen, die ich als Teil deiner Arbeitsgruppe sammeln durfte und für deine Unterstützung während meines Doktorates. Zudem möchte ich mich bei Birgit, Fips und Marion bedanken. Ihr habt mich während der gesamten Zeit auf unterschiedliche Arten unterstützt und begleitet und ich durfte viele schöne Sachen von euch lernen. Meinen Freunden abseits des Institutes möchte ich auch besonders danken. Ihr seid die Quelle vieler Freuden. Im Speziellen möchte ich Roman, Flo, Norbert & Selena, Thomas & Sarah, Dian, Michi und Martin erwähnen. Uns verbinden viele schöne Erlebnisse und ich hoffe es kommen noch viele dazu. Ich danke auch meiner Mama, Chrisi, Alexander und allen anderen Familienmitglieder, für ihre Liebe die sie mir entgegenbringen. Meinem Bruder Alexander möchte ich noch besonders danken. Du bist ein wunderbar neugieriger, talentierter und lustiger Mensch, der seinem alten Bruder auch hin und wieder einmal zu einem Fifa oder Lasertron Erfolg verhilft. Das Beste kommt bekanntlich zum Schluss und das bist Du Christina. Durch dich gewann mein Leben an Tiefe. Mit deinen vielen Talenten und deiner ansteckenden Art, sich zu freuen, bereicherst du tagtäglich mein Leben.

Danke, dass ihr so seid wie ihr seid!

Table of contents

"The secret of getting ahead is getting started. The secret of getting started is breaking your complex overwhelming tasks into small manageable tasks, and starting on the first one."

Mark Twain

Part I

Introduction

"My religion is nature. That's what arouses those feelings of wonder and mysticism and gratitude in me."

Oliver Sacks

1 Outline and scope of the thesis

Luminescent chemical sensors have already proven their usefulness for microfluidic applications thanks to various reasons such as their ease in miniaturization, their simple fabrication and integration into microfluidic chips or their ability for contactless readout. Therefore, the following thesis focuses on the development of measurement systems based on luminescent chemical sensors for the determination of oxygen and pH within microfluidic platforms. Herein, we aimed to improve the existing luminescent sensor technology by integrating, optimizing and characterizing new sensor systems for microfluidic applications. We focused not only on the sensor materials, we combined advanced sensor materials with accurate readout devices to create whole measurement systems. Furthermore, our developed sensor materials are compatible with commercially available readout devices in order to increase the accessibility for other researchers.

The first chapter, the introduction, provides a brief insight into microfluidics, refers to publications and reviews on luminescent chemical sensors for microfluidic platforms and addresses recent needs of different microfluidic fields for analytical detection tools. The aim of the introduction is to guide the reader's eye to these emerging needs and considerations during the development of microfluidic sensor systems and to provide a very condensed overview over these topics.

In the main part of my thesis three peer-reviewed publications are presented. The first publication deals with the integration, patterning and readout of oxygen sensors in silicon-glass based microreactors and features an airbrush spray-coating integration technique. The second publication presents a measurement system consisting of core-shell nanosensors and a readout device for the simultaneous determination of oxygen and pH within microreactors. The third publication introduces an imaging set-up based on a 2-CCD colour near infrared camera and planar sensor foils for the determination of the oxygen partial pressure, the pH value and for the simultaneous detection of both parameters.

A summary of co-authored publications with comments is presented at the end. The co-authored publications use the knowledge and techniques of our presented work for different applications such as cell culture experiments in microfluidic droplets, oxygen measurements within a microfluidic organ-on-a-chip device, biosensing of pesticides within a microfluidic chip or to predict the diffusivity of oxygen in oak wood during the aging process of red wine in barrels.

2 Luminescent chemical sensors & microfluidics

2.1 What is microfluidics and how is it connected to analytical chemistry?

According to George M. Whitesides, *microfluidics is the science and technology of systems that process or manipulate small amounts of fluids (≤ µL), using channels with dimensions in the micrometre range or below* [1]. This miniaturized length scale obviously allows the use of very small quantities of samples and reagents for different purposes and measurably changes fluid physics in comparison to the macroscale. In contrast to the macroscopic world, laminar flow occurs within microfluidics, which means that two fluids will flow side by side without eddies, and lateral mixing just happens by diffusion. On one hand this fact and other phenomena are useful and enable predictable diffusion kinetics, on the other hand simple operations such as mixing two fluids can be very difficult in microfluidics. The review *Microfluidics: Fluid physics at the nanoliter scale* from Squires and Quake explains these contradictions from day-to-day human experiences with fluids [2].

Microfluidics originates from four fields namely molecular analysis, biodefence, molecular biology and microelectronics [1]. Since 1975, analytical chemists fabricate miniaturized analytical devices [3] and in 1990 the concept of miniaturized total chemical analysis systems was proposed by Manz et al.[4]. Since then, all kinds of micro total analysis systems (µTAS) [3,5,6], also called lab-on-a-chip devices, were developed and therefore analytical chemistry has extensively contributed to the advancements in microfluidics. Thus, microfluidics provide a great toolbox for the development of analytical devices. I refer the interested reader to articles and reviews on materials for microfluidic devices [7–10], their fabrication techniques [11–16] and to a relatively new topic namely paper based microfluidic devices [17–20] in order to get an overview of the ongoing progress within this technology. In general, materials commonly used for microfluidic devices are polymers (for example PDMS, PS, PMMA or COC) which have mostly replaced the first generation materials silicon and glass. More recently the microfluidic community shows an increased interest in hydrophobically patterned paper thanks to its appealing properties for the development of portable low-cost point-of-care devices.

Unfortunately for many scientists and businessmen around the world, microfluidics is still searching for a 'killer application' and microfluidic techniques often have not matched the initial enthusiasm surrounding a particular area such as in mainstream biology research [21]. However, microfluidics is an useful tool with unique possibilities for different fields such as biomedical research [21], 3D cell culturing [22], microbiology [23,24], systems biology [25] or organic synthesis [26]. What can be learned and improved from

former studies is the necessity of more collaboration between the different disciplines (for example engineers, chemists, physicists and biologists) in order to address and solve the right problems with microfluidics. This would probably support the development of better suited, simpler and more accepted microfluidic solutions.

2.2 Luminescent chemical sensors and their use in microfluidics

According to IUPAC, *a chemical sensor is a device that transforms chemical information, ranging from the concentration of a specific sample component to total composition analysis, into an analytically useful signal. The chemical information, mentioned above, may originate from a chemical reaction of the analyte or from a physical property of the system investigated* [27]. Within this definition a chemical sensor consists of a receptor and a transducer. The receptor transforms the chemical information into a form of energy which may be measured by the transducer. The transducer is transforming this energy into a useful analytical signal. In the case of a luminescent chemical sensors the operating principle is based on luminescence. Within this thesis the term luminescent is used as synonym for photoluminescence. Although it may seem a bit imprecise, it is common sense in most publications to do so.

In general, a luminescent sensors consist of an indicator dye immobilized in an appropriate matrix (for example a polymeric film or nanoparticle) and a readout unit. The latter typically consists of a light source for excitation (for example a LED), optical components (for example lenses, optical filters or fibres), a photodetector (for example a photodiode), other opto-electronic parts and an output unit. The indicator dye is excited by the light source and shows a selective luminescence response to a targeted analyte. This response is guided by the optics to the optoelectronics and transformed into an electronic signal which is further processed by the output unit.

Common measurement concepts for luminescent sensors in microfluidic devices (see Fig. 2.1) are the integration of sensor layers (also named film or coating) [28] or the use of
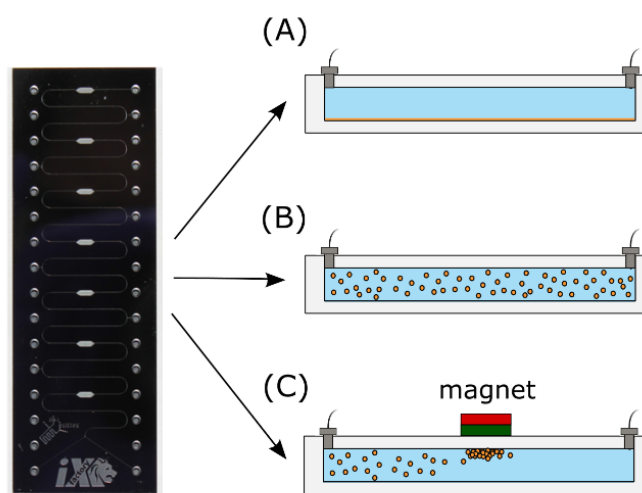
Figure 2.1 Common measurement concepts for luminescent sensors in microfluidic devices; integrated sensors film (A), sensor-particles (B) or magnetic sensor-particles (C).

sensor particles [29–32]. The latter can have magnetic properties which can be used to form sensing layers *in-situ* by magnets [33]. Nevertheless, the integration of luminescent sensor layers is the most common concept in the literature.

A recent review from Pfeiffer and Nagl gives an overview on microfluidic platforms with integrated luminescent sensors [28]. The review summarizes the different integration methods, readout techniques and applications. A common way to integrate luminescent sensors into microfluidic devices is the deposition of sensor coatings, which can be done by a variety of techniques such as blade-, dip-, spin-coating [28], inkjet printing [34–37] or airbrush spraying [38]. The latter was recently demonstrated by us and is presented within this thesis. Readout is usually performed outside of the chip by intensity based or lifetime based methods [39,40] either as single point measurement or imaging measurement [28]. Further information about luminescence sensing in microfluidics can be found in the already mentioned review [28] or in the dissertation from Birgit Ungerböck [41].

At present most luminescent sensors in microfluidics are used to monitor oxygen, pH or temperature (physical luminescent sensor) [28,42]. I refer the interested reader to reviews on oxygen [42,43], pH [44] and temperature sensing [45] for detailed information about the sensing mechanism, different dyes, matrices or readout techniques. Luminescent temperature sensors have been used for on chip temperature measurements [28]. Oxygen and pH sensors have mostly been used for cell culture experiments in microfluidics because the concentration of dissolved oxygen and the pH value are key parameters for monitoring and controlling cell growth [46]. Recent reports demonstrated another promising field, namely the use of fluorescent pH sensors for continuous electrophoretic separation of biomolecules in microfluidic chips via free flow isoelectric focussing [36,47].

Other analytes are hardly explored and were mostly presented at a proof of concept level [28] possibly because issues such as selectivity, brightness, response time or photostability of the used sensors are limiting their area of application. However, even for the common analytes such as pH and oxygen or temperature luminescent sensing technology in microfluidics has to become easier accessible for other fields such as biology, medicine or microbiology and in addition more time should be spent on the training of inexperienced sensor users.

2.3 Considerations for luminescent chemical sensors in microfluidics

The aim of analytical chemists can possibly be summarized by the challenge to develop accurate, precise, robust and reliable tools (for example systems, devices, methods or protocols) for solving analytical questions and most of the time this goal is just reached by slow approximation steps. Luminescent chemical sensors have already touched this

goal for certain applications such as oxygen sensing in aqueous solutions and for others (for example glucose sensing) they are on the way of becoming more reliable. Some general conclusions out of these developments can be drawn and are summarized below.

'Ideal' sensors do not exist and any sensor has its own limitations. Important parameters when designing a new sensor are the photophysical properties of the used luminescent dyes (absorption, emission and brightness), their photostabilities and the properties of the sensor matrix. The plural word 'dyes' was chosen because often two or more dyes (for example an indicator and a reference dye) are used within a sensor. Absorption and emission spectra of the dyes should fulfil certain requirements, for example they should show a large Stokes shift, should be compatible with the readout unit and the microfluidic chip material, and should be located in a spectral region where less background disturbances occur. Sample constituents such as living tissue or proteins often cause unwanted scattering, absorption or emission of light and thus disturb the measurement. A common way to circumvent this is the usage of near infrared emitting dyes. A recent review gives an overview of existing dyes for different applications such as oxygen, pH or metal ion sensing [48].

Another important parameter is the luminescence brightness (BS). It is per definition the product of the luminescence quantum yield (QY) and the molar absorption coefficient (ε). High brightness is very important for microfluidic applications because the measuring area within microfluidic chips is limited. The molar absorption coefficient should be preferably above 80 000 $M^{-1}\,cm^{-1}$ and the quantum yield should rather exceed 20 % in order to reach an acceptable brightness.

Every luminescent dye suffers from photostability issues depending on the used light intensities and excitation intervals during the measurement. Dyes ensuring a good photostability should preferably be used (for example porphyrins, aza-BODIPYs [48]) and photobleaching experiments should be performed carefully for the whole sensor and not only for the dye itself in order to characterize the system precisely.

The sensor matrix (for example a polymeric film or nanoparticle) is another important parameter. It co-determines the sensor performance by creating a defined and stable environment for immobilized dyes and protects them from undesired interactions with other sample components. Furthermore, the matrix should show a good adhesion to the used microfluidic chip material (for example PDMS, COC, PS or glass). Additionally, adjustment of the matrix properties can be used to tune sensing characteristics such as the dynamic range, response time or sensitivity. The direct use of luminescent dyes without a sensing matrix is problematic because they are often less stable without protection, harmful to cells and undesired interactions lead to unpredictable measurement signals. Dyes can either be covalently immobilized or physically entrapped within a matrix. Covalent coupling would be the preferred method because leaching of

the dye hardly occurs. However, the synthesis of such sensor materials is not trivial and often time consuming. The entrapment of lipophilic dyes in hydrophobic polymers often also completely eliminates leaching (at least in aqueous solutions) and is usually easier to implement.

Processability and stability of a sensor (mostly influenced by the sensor matrix) are other important parameters especially for microfluidic applications. Integrated sensors are typically deposited within a microfluidic chip before closing it, the so-called chip bonding. The bonding procedure may vary according to the chip material however, elevated temperatures or chemicals are commonly used. The sensor materials should tolerate these conditions although compromises have to be made most of the time.

Moving away from the sensing chemistry, the handling of a sensor is also of great importance especially when other researchers are using the developed sensing tools. Every sensor has its own calibration protocols and limitations; for example most luminescent sensors are cross sensitive to the temperature which is a common source of inaccuracies during measurements. Obviously, a thorough sensor characterization is an essential and time consuming part during sensor development in order to identify and admit the significant limitations of one´s sensor. Furthermore, preparation of standard operating procedures and conduction of training course for inexperienced users are indispensable for the establishment of reliable sensor systems. It is a long and probably unreachable way to the 'ideal' sensor. Nevertheless this way will be full of interesting research and findings.

2.4 Perspective on luminescent chemical sensors in microfluidics

Microfluidics is still growing and emerging fields such as organs-on-chips [22] or droplet microfluidics [24] have an increased demand for analytical detection tools. The online monitoring of process parameters such as oxygen, pH, glucose or lactate is an important factor for the establishment of reliable and verifiable protocols for different microfluidic applications such as cell culturing.

Luminescent oxygen sensing tools are reliable and available for aqueous media. However, optimization steps of these tools are often necessary in order to match the specific analytical requirements of different microfluidic applications. Microfluidic research would greatly benefit from an increased accessibility of reliable oxygen sensor systems because researchers from different fields (for example engineers, physicist, biologists or microbiologists) have only limited access to these tools at the moment.

Similar to oxygen, pH sensing technology exists though the access for other researchers is even more restricted because there are less systems commercially available. Therefore, easy accessible sensor system are urgently needed for microfluidic applications.

Unfortunately, luminescent pH sensors still suffer from limitations such as small measuring ranges, restricted stabilities or cross sensitivity to ionic strength, which make pH sensors more prone to errors compared to oxygen sensors. Novel pH sensors provide improvements for these challenges, but they still need optimization and adaption before being ready for use in microfluidic applications. A recent min-review summarizes the current state of the art of oxygen and pH sensors for bioprocess monitoring from millilitre to benchtop scale and provides an insight into existing technologies [46].

At the moment luminescent sensing of other analytes in microfluidics is still in its infancy. This situation will hopefully change in the near future and a couple of new luminescent sensors such as an organic solvent resistant oxygen sensor, a glucose sensor or a potassium sensor are hopefully available soon for microfluidic platforms. The future of microfluidics is certainly entangled with the ability to measure reliably at this tiny scale. Therefore, the development of sensing tools is an important requirement for the progress of microfluidics. Luminescent sensors are one possibility to achieve this goal and will play a role for sure. However, the progress of scientist in developing powerful sensor systems will possibly decide how important their role will be.

2.5 List of abbreviations

μTAS   micro total analysis system
CCD   charge coupled device
COC   cyclic olefin copolymer
IUPAC   International Union of Pure and Applied Chemistry
LED   light emitting diode
nL   nanoliter
PDMS   polydimethylsiloxane
PMMA   poly(methyl methacrylate)
PS   polystyrene

2.6 References

(1) Whitesides, G. M. *Nature*, **2006**, *442* (7101), 368–373.
(2) Squires, T. M.; Quake, S. R. *Rev. Mod. Phys.*, **2005**, *77* (3), 977–1026.
(3) Reyes, D. R.; Iossifidis, D.; Auroux, P.-A.; Manz, A. *Anal. Chem.*, **2002**, *74* (12), 2623–2636.
(4) Manz, A.; Graber, N.; Widmer, H. M. *Sensors and Actuators B: Chemical*, **1990**, *1* (1-6), 244–248.

(5) Culbertson, C. T.; Mickleburgh, T. G.; Stewart-James, S. A.; Sellens, K. A.; Pressnall, M. *Analytical chemistry*, **2014**, *86* (1), 95–118.

(6) Patabadige, D. E. W.; Jia, S.; Sibbitts, J.; Sadeghi, J.; Sellens, K.; Culbertson, C. T. *Analytical chemistry*, **2016**, *88* (1), 320–338.

(7) McDonald, J. C.; Duffy, D. C.; Anderson, J. R.; Chiu, D. T.; Wu, H.; Schueller, O. J. A.; Whitesides, G. M. *Electrophoresis*, **2000**, *21* (1), 27–40.

(8) Becker, H. *Talanta*, **2002**, *56* (2), 267–287.

(9) Ren, K.; Chen, Y.; Wu, H. *Current opinion in biotechnology*, **2014**, *25*, 78–85.

(10) Berthier, E.; Young, E. W. K.; Beebe, D. *Lab on a chip*, **2012**, *12* (7), 1224–1237.

(11) Au, A. K.; Huynh, W.; Horowitz, L. F.; Folch, A. *Angewandte Chemie (International ed. in English)*, **2016**, *55* (12), 3862–3881.

(12) Guckenberger, D. J.; Groot, T. E. de; Wan, A. M. D.; Beebe, D. J.; Young, E. W. K. *Lab on a chip*, **2015**, *15* (11), 2364–2378.

(13) Ho, C. M. B.; Ng, S. H.; Li, K. H. H.; Yoon, Y.-J. *Lab on a chip*, **2015**, *15* (18), 3627–3637.

(14) Temiz, Y.; Lovchik, R. D.; Kaigala, G. V.; Delamarche, E. *Microelectronic Engineering*, **2015**, *132*, 156–175.

(15) Becker, H.; Gartner, C. *Analytical and bioanalytical chemistry*, **2008**, *390* (1), 89–111.

(16) Knowles, K. M.; van Helvoort, A. T. J. *International Materials Reviews*, **2013**, *51* (5), 273–311.

(17) Hu, J.; Wang, S.; Wang, L.; Li, F.; Pingguan-Murphy, B.; Lu, T. J.; Xu, F. *Biosensors & bioelectronics*, **2014**, *54*, 585–597.

(18) Cate, D. M.; Adkins, J. A.; Mettakoonpitak, J.; Henry, C. S. *Analytical chemistry*, **2015**, *87* (1), 19–41.

(19) Yamada, K.; Henares, T. G.; Suzuki, K.; Citterio, D. *Angewandte Chemie (International ed. in English)*, **2015**, *54* (18), 5294–5310.

(20) Yetisen, A. K.; Akram, M. S.; Lowe, C. R. *Lab on a chip*, **2013**, *13* (12), 2210–2251.

(21) Sackmann, E. K.; Fulton, A. L.; Beebe, D. J. *Nature*, **2014**, *507* (7491), 181–189.

(22) Bhatia, S. N.; Ingber, D. E. *Nature biotechnology*, **2014**, *32* (8), 760–772.

(23) Guo, M. T.; Rotem, A.; Heyman, J. A.; Weitz, D. A. *Lab on a chip*, **2012**, *12* (12), 2146–2155.

(24) Kaminski, T. S.; Scheler, O.; Garstecki, P. *Lab on a chip*, **2016**, *16* (12), 2168–2187.

(25) Liu, Y.; Lu, H. *Current opinion in biotechnology*, **2016**, *39*, 215–220.

(26) Gutmann, B.; Cantillo, D.; Kappe, C. O. *Angewandte Chemie (International ed. in English)*, **2015**, *54* (23), 6688–6728.

(27) Hulanicki, A.; Glab, S.; Ingman, F. *Pure and Applied Chemistry*, **1991**, *63* (9).

(28) Pfeiffer, S. A.; Nagl, S. *Methods Appl. Fluoresc.*, **2015**, *3* (3), 34003.

(29) Funfak, A.; Cao, J.; Wolfbeis, O. S.; Martin, K.; Köhler, J. M. *Microchim Acta*, **2009**, *164* (3-4), 279–286.

(30) Ungerböck, B.; Pohar, A.; Mayr, T.; Plazl, I. *Microfluid Nanofluid*, **2013**, *14* (3-4), 565–574.

(31) Mahler, L.; Tovar, M.; Weber, T.; Brandes, S.; Rudolph, M. M.; Ehgartner, J.; Mayr, T.; Figge, M. T.; Roth, M.; Zang, E. *RSC Adv*, **2015**, *5* (123), 101871–101878.

(32) Cao, J.; Nagl, S.; Kothe, E.; Köhler, J. M. *Microchimica Acta*, **2015**, *182* (1), 385–394.

(33) Ungerbock, B.; Fellinger, S.; Sulzer, P.; Abel, T.; Mayr, T. *The Analyst*, **2014**, *139* (10), 2551–2559.

(34) Thete, A. R.; Gross, G. A.; Henkel, T.; Koehler, J. M. *Chemical Engineering Journal*, **2008**, *135* (Supplement 1), 327–332.

(35) Thete, A. R.; Gross, G. A.; Koehler, J. M. *The Analyst*, **2009**, *134* (2), 394–400.

(36) Herzog, C.; Beckert, E.; Nagl, S. *Analytical chemistry*, **2014**, *86* (19), 9533–9539.

(37) Poehler, E.; Herzog, C.; Suendermann, M.; Pfeiffer, S. A.; Nagl, S. *Eng. Life Sci.*, **2015**, *15* (3), 276–285.

(38) Ehgartner, J.; Sulzer, P.; Burger, T.; Kasjanow, A.; Bouwes, D.; Krühne, U.; Klimant, I.; Mayr, T. *Sensors and Actuators B: Chemical*, **2016**, *228*, 748–757.

(39) McDonagh, C.; Burke, C. S.; MacCraith, B. D. *Chemical reviews*, **2008**, *108* (2), 400–422.

(40) Collier, B. B.; McShane, M. J. *Journal of Luminescence*, **2013**, *144*, 180–190.

(41) Birgit Ungerböck, Dissertation, *Integration of Luminescent Chemical Sensors into Miniaturized Devices,* University of Technology Graz, Graz, 2014.

(42) Grist, S. M.; Chrostowski, L.; Cheung, K. C. *Sensors (Basel)*, **2010**, *10* (10), 9286–9316.

(43) Quaranta, M.; Borisov, S. M.; Klimant, I. *Bioanalytical reviews*, **2012**, *4* (2-4), 115–157.

(44) Wencel, D.; Abel, T.; McDonagh, C. *Anal. Chem.*, **2014**, *86* (1), 15–29.

(45) Wang, X.-d.; Wolfbeis, O. S.; Meier, R. J. *Chemical Society reviews*, **2013**, *42* (19), 7834–7869.

(46) Demuth, C.; Varonier, J.; Jossen, V.; Eibl, R.; Eibl, D. *Applied microbiology and biotechnology*, **2016**, *100* (9), 3853–3863.

(47) Poehler, E.; Herzog, C.; Lotter, C.; Pfeiffer, S. A.; Aigner, D.; Mayr, T.; Nagl, S. *The Analyst*, **2015**, *140* (22), 7496–7502.

(48) Christoph Staudinger and Sergey M Borisov. *Methods and Applications in Fluorescence*, **2015**, *3* (4), 1–37.

"It is the tension between creativity and skepticism that has produced the stunning and unexpected findings of science."

Carl Sagan

Part II

First-authored publications in peer-reviewed journals

"Not Everything that is Measurable Matters and Not Everything that Matters is Measurable."

Ian Bache

3 Online analysis of oxygen inside silicon-glass microreactors with integrated optical sensors

Authors: Josef Ehgartner [a], Philipp Sulzer [a], Tobias Burger [a], Alice Kasjanow [b], Dominique Bouwes [b], Ulrich Krühne [c], Ingo Klimant [a] and Torsten Mayr [a]

[a] Institute of Analytical Chemistry and Food Chemistry, Graz University of Technology, Stremayrgasse 9/3, 8010 Graz, Austria.
[b] iX-factory GmbH, 44263 Dortmund, Germany.
[c] Centre for Process Engineering and Technology, Department of Chemical and Biochemical Engineering, Technical University of Denmark, Søltofts plads, 2800 Kgs. Lyngby, Denmark.

Abstract A powerful online analysis set-up for oxygen measurements within microfluidic devices is presented. It features integration of optical oxygen sensors into microreactors, which enables contactless, accurate and inexpensive readout using commercially available oxygen meters via luminescent lifetime measurements in the frequency domain (phase shifts). The fabrication and patterning of sensor layers down to a size of 100 μm in diameter is performed via automated airbrush spraying and was used for the integration into silicon-glass microreactors. A novel and easily processable sensor material is also presented and consists of a polystyrene- silicone rubber composite matrix with embedded palladium(II) or platinum(II) *meso*-tetra(4-fluorophenyl) tetrabenzoporphyrin (PdTPTBPF and PtTPTBPF) as oxygen sensitive dye. The resulting sensor layers have several advantages such as being excitable with red light, emitting in the near-infrared spectral region, being photostable and covering a wide oxygen concentration range. The trace oxygen sensor (PdTPTBPF) in particular shows a resolution of 0.06–0.22 hPa at oxygen concentrations lower than 20 hPa (< 2% oxygen) and the normal range oxygen sensor (PtTPTBPF) shows a resolution of 0.2–0.6 hPa at low oxygen concentrations (< 50 hPa) and 1–2 hPa at ambient air oxygen concentrations. The sensors were integrated into different silicon-glass microreactors which were manufactured using mass production compatible processes. The obtained microreactors were applied for online monitoring of enzyme transformations, including D-alanine or

D-phenylalanine oxidation by D-amino acid oxidase, and glucose oxidation by glucose oxidase.

3.1 Introduction

Microfluidic platforms are useful tools for studying organic reactions [1], enzyme kinetics [2–4] and cells [5–8] at micro- or nanoscale. The small volumes of such devices allow a view behind the scenes of bulk characteristics of molecules, enzymes and cells. Faced with decreasing dimensions, however, analytical chemists are challenged to find new methods to determine analytes accurately. The integration of luminescent chemical sensors into microfluidic devices can be one useful technique for obtaining online and real-time analytical data at this miniaturized scale [9,10]. Luminescent oxygen sensors are highly suited for microfluidic applications due to their high sensitivity, ability of contactless readout, ease of miniaturization, ease of integration and their low cost [11]. Moreover, optical oxygen sensors do not need a reference element and do not deplete oxygen during the measurement in comparison to electrochemical sensors. Nonetheless, ground state triplet oxygen is transformed into reactive excited state singlet oxygen during the quenching process of the luminescent oxygen sensors [12–14]. The excited state singlet oxygen can react with its surrounding environment and therefore can bias the investigated system in the microscale [15].

One of the first publications dealing with the integration of a luminescent oxygen sensor into a silicon based microfluidic device was from Sin et al. [16]. They developed a cell culture system for mammalian cells and machined a 3 mm x 3 mm x 0.15 mm recess into the bottom plate of the chip which was filled with a resin-adsorbed ruthenium(II) complex as oxygen indicator dye and poly(dimethylsiloxane) (PDMS) to obtain an oxygen sensor patch. The oxygen sensor was chosen as a proof-of-concept integrated sensor and used to monitor the adequate oxygen supply for the cells. In another study Thorsen et al. [17,18] showed the integration of a sensor layer consisting of platinum(II) octaethyl-porphyrin-ketone and polystyrene into a PDMS-based microfluidic differential oxygenator for cell culture. A sensor solution was manually pipetted onto etched glass slides, the solvent was evaporated and the functionalized glass slide was bonded by an oxygen plasma treatment to a structured PDMS layer. The same sensor chemistry was used by Nock et al. [19,20] to integrate a patterned sensor film within a PDMS-based microfluidic device. The patterning process included spin-coating of the sensor film onto a glass slide and patterning either by soft-lithography with PDMS stamps and reactive ion etching in an oxygen plasma [19] or a process based on a sacrificial metal layer and plasma patterning of the spin-coated sensor layer [20]. Etzkorn et al. fabricated oxygen sensor rings on glass wafers by spin coating in combination with a photopatterning process [21]. The sensors were used to determine the oxygen consumption

rates of single cells in glass microwell arrays. Another study introduced oxygen sensor beads in microwells. The adherence of the sensor beads to the glass well was achieved by slightly melting them [22]. Commercially available oxygen sensor patches were also integrated into microbioreactors for monitoring oxygen during microbial fermentations [23–25]. In other studies prefabricated spin coated sensor layers containing a platinum(II)-porphyrin complex were used in microfluidic devices for regulating oxygen levels [26, 27] and for cell culture [28]. In another study a similar sensor chemistry was integrated into microfluidic channels of a PDMS-glass-based microscale reactor [29]. The oxygen sensor was spin-coated onto a glass substrate which already contained microchannels. The sensing layer outside of the microchannels was removed with a razor blade, prior to assemble the microscale reactor. Grist et al. used a laser cutter system to pattern oxygen sensing films [30]. Spin-coated polystyrene films were structured by the laser cutter and the unwanted bulk film was removed by aqueous lift-off/peeling. In another study, we reported recently the introduction of oxygen-sensitive conjugated polymer nanoparticles into microfluidic devices [31]. As described above, integration and patterning of oxygen sensor layers into microfluidic devices were often accomplished by spin coating of a sensor solution onto a substrate in combination with the removal of the surplus bulk material. In further reports optical chemical sensors for other analytes like pH were also incorporated by inkjet printers into microfluidic devices [32–35]. Herein, we demonstrate that airbrush spraying in combination with stencils is a promising alternative to incorporate patterned oxygen sensing layers into microfluidic devices. Moreover, we adapted commercially available oxygen meters to make them ready for use in microfluidic applications. The presented oxygen sensor layers are an improvement to former reports because they show a higher brightness (BS = ε * quantum yield), are excitable with red light, emit in the near infrared (a spectral region where fewer compounds emit) and are fully compatible with the used oxygen meters [36]. Furthermore, we tested our set-up in silicon-glass microreactors for online monitoring of oxygen by different oxygen depleting enzyme reactions.

3.2 Experimental

3.2.1 Materials

Palladium(II) and platinum(II) *meso*-tetra(4-fluorophenyl) tetrabenzoporphyrin (PdTPTBPF and PtTPTBPF, respectively; chemical structures Supplementary Information SI Fig. 3.1) were synthesized in-house according to the literature procedure [37]. Polystyrene (PS; average molecular weight = 250 000 g/mol) was purchased from Fisher Scientific (www.fishersci.com), chloroform and α-D(+)-glucose monohydrate were bought from Roth (www.carl-roth.de). Silicone rubber ELASTOIL®

E4 was obtained from Wacker (www.wacker.com). D-phenylalanine, D-alanine, D- amino acid oxidase from porcine kidney, glucose oxidase from *Aspergillus niger*, catalase from bovine liver and poly(ethylene glycol) (PEG 6000, av. MW= 6000) were purchased from Sigma Aldrich, gases for calibration from Linde (www.linde-gas.at).

The microreactors were manufactured using batch-production compatible processes. The general steps of the production process are described below (Fig. 3.1). The designed microreactors consist of a silicon part with microfluidic structures and a glass part with integrated oxygen sensors and access holes. Silicon wafers were structured by a photolithography process followed by dry etching. The use of silicon together with dry etching allowed the production of microfluidic structures with aspect ratios up to 1:20 and a nearly perpendicular channel-profile, which is not possible with glass.

A silicon wafer (crystal orientation = 100) with a thickness of 675 µm was coated with a positive photoresist (ma-P 1240). The photoresist had a layer thickness of 4 µm and was baked for 2 min at 95 °C. This photoresist is highly stable in dry etching processes. An UV-lithography was performed with a mask aligner from Suss Microtec (www.suss.com) with a dose of 110 mJ/cm². Alignment marks in the channel design will guarantee an accurate positioning of the access holes in the glass wafer. After developing for 2 min in a beaker with mr-D 526 developer the wafer was rinsed with deionized water for 2 min. The Bosch process was applied for the etching to reach a channel depth of 200 µm. The etching was performed in a deep reactive
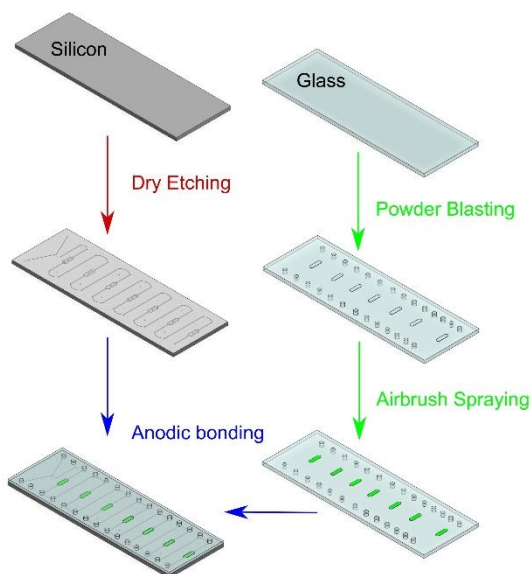
Figure 3.1 Schematic overview of the chip-manufacturing process.

ion etcher (Alcatel AMS 110). The etch gasses SF_6/C_4F_8 (400/200 sccm) were alternately introduced for 2.5 s at a power of 2000 W in a capacitive coupled plasma of 50 W. After etching the wafer, the resist was removed in an oxygen plasma. The resist stripping was done in a plasma etcher from PVA TePla (www.pvatepla.com) with 200 sccm oxygen at 500 W for 15 min. The depth was measured with a profiler. In parallel, a stencil mask for the sensor areas was fabricated. A silicon wafer (crystal orientation = 100) with a thickness of 300 µm was coated with the positive photo-resist (ma-P 1240) and processed as described above. During the dry etching, trenches were etched, which were the openings for the spray-coating procedure (described below). Before the stencil mask was

used, the fluidic access holes were fabricated into the glass wafer. Therefore either powder blasting or laser drilling can be applied. A photolithography process was required as described above for powder blasting. The holes have a diameter of 1.5 mm. Subsequently, the stencil mask was positioned on the alignment marks on top of the glass wafer and fixed with tape (Kapton® or UV removable tape). In the next step, the sensing areas were spray-coated as described below. After integration of the sensing area, the tape can be easily removed and the stencil mask can be reused for the next spraying process. The silicon wafer and the glass wafer were anodic bonded using a CB8 wafer bonder from Suss Microtec. During this process step, the microfluidic channels were closed. To secure the functionality of the sensors, the bond temperature was decreased to 180 °C but the bonding time had to be increased. The anodic bonding was realized at 1000 V and a pressure of 5 kN within 4 h. The wafers were diced after bonding into microreactor chips in the size of microscopic slides (75.5 mm × 25.5 mm) to achieve compatibility of the microfluidic modules with standard laboratory equipment. A DAD 3350 dicing tool from Disco (www.discoeurope.com) with a dicing blade of 300 μm was used.

3.2.2 Integration and characterization of the oxygen sensors

Sensor dye (PdTPTBPF or PtTPTBPF; 0.45 mg), silicone rubber (30 mg) and polystyrene (15 mg) were dissolved in chloroform (1.5 g) to obtain a sensor "cocktail". Silicone rubber was added because of its better adherence properties for glass compared to polystyrene. This "cocktail" was deposited onto glass wafers with photomasks as stencils using an in-house developed computerized numerical control (CNC) air-brush spraying device (SI Fig. 3.2). The spraying device consists of an airbrush (EFBE Spritzautomat 1/2L, 0.2 mm nozzle diameter, www.efbe-airbrush.de) fixed to an x-y-z table actuated by stepper motors (two-phase-stepper-motor, www.isel-gmbh.com). The motors are controlled by a Triple Beast Driver (www.benezan-electronics.de), which also drives a fourth axis extension for the airbrush needle valve and a solenoid valve (SMC) for airflow switching. The opening of the airbrush needle valve in combination with the opening time determines the amount of deposited material. The spraying procedure was automated by using G-Code and LinuxCNC (www.linuxcnc.org). The sensor films were cured at 60 °C for 24 hours. Layer thicknesses were determined on a Bruker DekTak XT surface profiler. After curing, the sensor layers were gas-phase calibrated in an in-house developed temperature controlled calibration chamber. Two mass flow controller instruments (Read Y smart series) by Vögtlin instruments (www.voegtlin.com) were used to obtain gas mixtures of defined oxygen partial pressures (pO_2). Compressed air, 2% (v/v) oxygen in nitrogen and nitrogen were used as calibration gases. The calibration gas was passed through a stainless steel coil which was dipped into a temperature-

controlled water bath before reaching the calibration chamber. The sensor layers were calibrated again after the bonding procedure to study its influence on the sensor material.
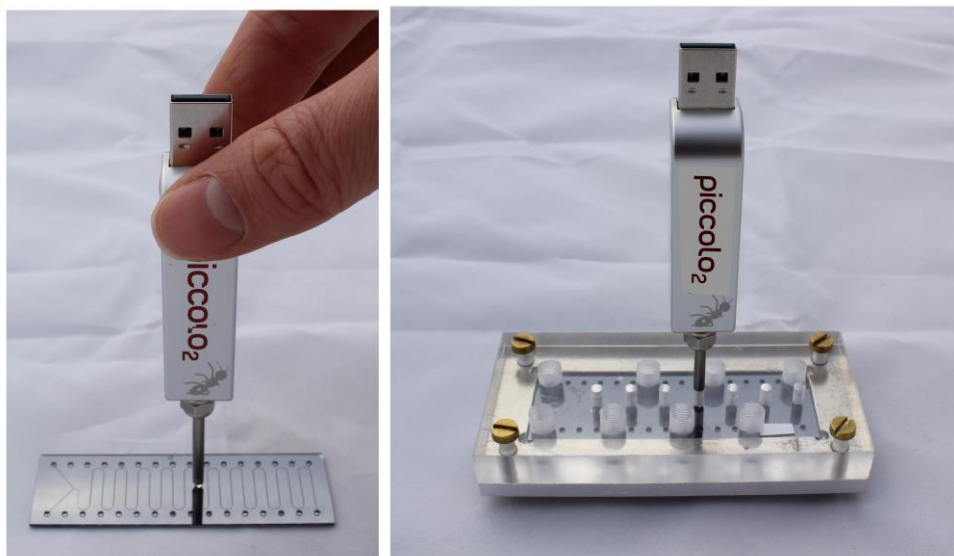
Figure 3.2 Measurement set-up consisting of the USB oxygen meter, the microfluidic chip and the in-house developed chip holder.

3.2.3 Online monitoring of enzyme reactions

Microreactors were connected via an in-house developed chip holder (Fig. 3.2 and SI Fig. 3.3) to syringe pumps (Cavro® Centris pumps from Tecan, www.tecan.com) which were operated by a specially written Lab VIEW program (www.ni.com/labview) we developed for this purpose. The oxidations of D-alanine and D-phenylalanine by D- amino acide oxidase, and glucose oxidation by glucose oxidase were used as model reactions. Therefore, D-alanine (35.4 mg, 100mM), D-phenylalanine (65.6 mg, 100mM) and D-amino acid oxidase (2.1 mg) were thus each dissolved in 4 mL of 100 mM TRIS buffer, pH 8.3 containing PEG 6000 (50 mg). α-D(+)-glucose monohydrate (500 mg, 50 mM) and glucose oxidase (2.5 mg for the enzyme cascade with catalase, otherwise 0.9 mg) were dissolved each in 50 mL of 10 mM phosphate buffer, pH 7.0 containing sodium chloride (130 mM) and PEG 6000 (600 mg). The oxidation of glucose was carried out in the absence or presence of catalase (approx. 4 mg in 50 mL of 10 mM phosphate buffer containing 130 mM NaCl and 600 mg PEG 6000). A two point calibration of the oxygen sensors was performed with air saturated water and deoxygenated water before the analysis. The microreactors were also purged with buffer containing 1% w/w PEG 6000 prior to the measurement to minimize non-specific binding of the enzymes to the surface. The microreactor contained two main inlets each connected to a separate

syringe pump. One inlet was used to introduce the enzyme solution into the chip and the other to introduce the substrates. The catalase solution was introduced over a lateral inlet by a third syringe pump. The channels of the used microreactor were 200 μm or 400 μm deep and 100 μm or 200 μm wide. The flow rate during the oxidation of the amino acids was 0.6 μL/s (0.3 μL/s for each pump). Different flow rates (1.2 μL/s, 0.8 μL/s, 0.4 μL/s, 0.2 μL/s) were applied for the oxidation of glucose. All syringe pumps were operated at a flow rate of 0.1 μL/s for the catalase experiment. All enzyme reactions were carried out at room temperature. The oxygen measurements within the microreactor were carried out either with a 4-channel optical oxygen meter (FireStingO2) connected to optical fibres (Plastic fibre cable, simplex fibre 1mm, PE-jacket 2.2 mm, www.ratioplast.com) or with a USB oxygen meter (Piccolo2) connected to a stainless steel tube including an optical plastic fibre (2 mm in diameter); both devices were obtained from Pyroscience (www.pyro-science.com). The optical fibre for the USB oxygen meter was adapted with a GRadient INdex (GRIN lens, www.grintech.de) to enhance the signal intensities, especially for smaller sensor layers. The lens was attached in front of the fibre. The modulation frequency of the optical oxygen meter was set to 4000 Hz for PtTPTBPF and to 400 Hz for PdTPTBPF. The intensity of the LED varied according to the sensor size but was generally set ≤ 60% and the amplification of signal was typically set ≤ 400x.

3.3 Results and Discussion

We aimed to develop an analysis set-up based on optical sensors for the quantitative determination of oxygen. The development involved the following steps: (i) integration of sensor structures into silicon-glass microreactors, (ii) characterization of sensors, (iii) modification of measurement devices, and (iv) testing of the set-up.

3.3.1 Integration and characterization of oxygen sensors

Airbrush spraying was used to produce sensor films with different shapes and sizes, because similar to inkjet printing, it allows selective deposition and patterning of optical sensors at various positions along a microfluidic chip. The smallest sensor spots sprayed with stencils had diameters of 100 μm (Fig. 3.3) and spots sprayed without stencils had diameters of 2 mm. We obtained homogeneous sensor layers and used on average 2 μl sensor cocktail per spot (2 mm in diameter). In principle, one third of this volume would also lead to sufficient sensor signals. The airbrush spraying set-up can be used with sensor "cocktails" containing volatile solvents and is not prone to clogging when the sensor solution is sufficiently diluted. Sensor solutions should contain less than 2% w/w of polystyrene (molecular weight = 250 000 g/mol) to reliably operate the spraying system if chloroform is used as solvent. In addition, the used CNC airbrush spraying set-

up can be programmed which is a helpful step for obtaining reproducible sensor layers. The thickness of the produced films can be adjusted by the number of spraying repetitions or by adjusting the opening of the needle valve. Our produced sensor layers had on average a thickness of 2.2 ± 0.2 µm (n = 7, spraying repetitions = 20), but also sensor layers with a thickness of approx. 0.5 µm provide sufficient signals with the used sensor cocktail. We deposited the sensing layers onto glass. The sensor material consisted of a polystyrene- silicone rubber composite matrix with the oxygen indicator dye physically entrapped. The addition of silicone rubber increases the adherence to glass due to its increased hydrophilicity compared to a common polystyrene matrix. The composite material exhibits additionally similar sensing properties for oxygen compared to polystyrene. The calibration curves of the new composite material and common polystyrene matrices are comparable (SI Fig. 3.4). We thus assume that the indicator dye is mostly entrapped in the polystyrene domains of the composite due to the low solubility of our indicator dyes in silicones [38].
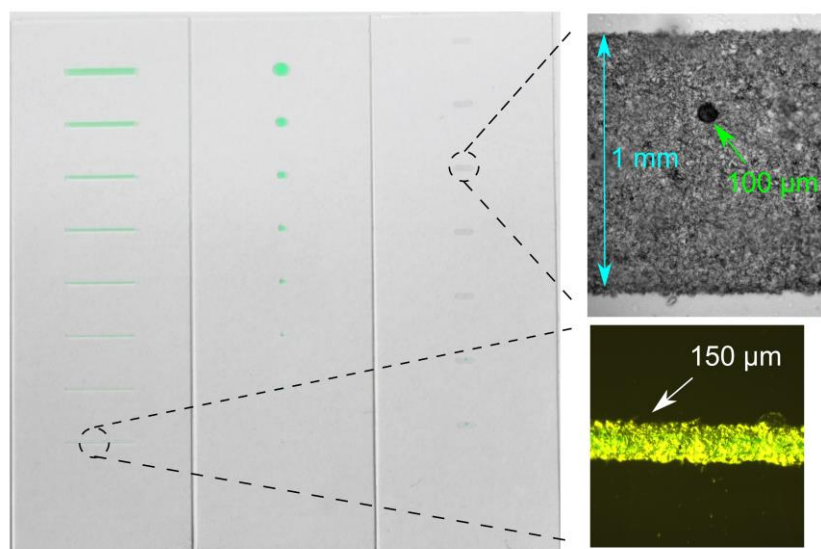
Figure 3.3 Sensing lines or spots ranging from 1000 µm to 100 µm in width or diameter and microscopic bright-field images of a 100 µm sensor spot integrated into a 1 mm wide sensing area and of a 150 µm wide sensor line. Lines and spots were prepared by airbrush spraying in combination with stencils. Microscopic bright-field images were taken with a monochromatic camera (spot) or a colour camera (line).

Stern-Volmer calibration curves of the new sensing material are shown in Fig. 3.4. The calibration curves were recorded in replicates (n=3). The error bars in Fig. 3.4 (hardly noticeable) reflect the variation of a single sensor layer calibrated three times. The relative standard deviations (RSD) are < 0.5%. Calibration curves of independently manufactured sensing layers combined in one calibration (n = 3 for PdTPTBPF and n = 8 PtTPTBPF) are shown in SI Fig. 3.5. Their relative standard deviations (RSD) are < 5% and reflect the variation of the manufacturing process. A simple two point

calibration procedure is typically sufficient to achieve high accuracy. The two-site model was used to fit the calibration data [39] (equation 1).

$$\frac{I_0}{I} = \frac{\tau_0}{\tau} = \left(\frac{f_1}{1+K_{SV,1} \cdot pO_2} + \frac{f_2}{1+K_{SV,2} \cdot pO_2} \right)^{-1} \quad (3.1)$$

The ratio I_0/I in the model was replaced by τ_0/τ where τ is the lifetime of the oxygen indicator dye at a certain pO_2-value, therefore the two-site model has no physical significance. The lifetime τ_0 represents the lifetime under deoxygenated conditions, where the oxygen indicator is in its unquenched state. The lifetimes were calculated from the phase shift $\Delta\phi$ recorded by the oxygen meter according to the equation $\tau = \tan(\Delta\phi)/(2*\pi*f)$, where f is the modulation frequency. The calibration parameters are shown in table 1.

Table 3.1 Calibration parameters for the sensing layers at 20 °C.

	$K_{SV,1}$ / * 10^{-3} hPa^{-1}	$K_{SV,2}$ / * 10^{-3} hPa^{-1}	f_1
PtTPTBPF	17.4	2.03	0.821
PdTPTBPF	110.8	21.1	0.638

The resolution of the measurement set-up for the normal range oxygen sensor (PtTPTBPF) was about 0.2-0.6 hPa at low oxygen concentrations (< 50 hPa) and about 1 - 2 hPa at ambient air oxygen concentrations (approx. 204 hPa at 980 mbar air pressure). The trace range oxygen sensor (< 20 hPa; PdTPTBPF) showed a resolution of about 0.06-0.22 hPa. The resolution was calculated by inserting the upper and lower limit of a calibration point (mean value ± the standard deviation) into equation (3.1), the equation was solved for pO_2 and the difference was calculated out of these values. The limit of detection was 0.08 hPa for the normal range oxygen sensor and 0.009 hPa for the trace range oxygen sensor [$\tau_0/(\tau_0 \pm 3*\sigma)$]. Anodic bonding of the glass-silicon microreactors was performed at a temperature of approx. 180 °C and calibration before and after bonding revealed that the sensor materials became more sensitive after bonding (SI Fig. 3.5). We assume that the composite matrix became more permeable for oxygen due to the increased temperature during the bonding process. Nevertheless this does not have a significant impact on the sensor performance. In addition, the size of the sensing areas had no significant influence on the calibration function (SI Fig. 3.6 - 3.7).
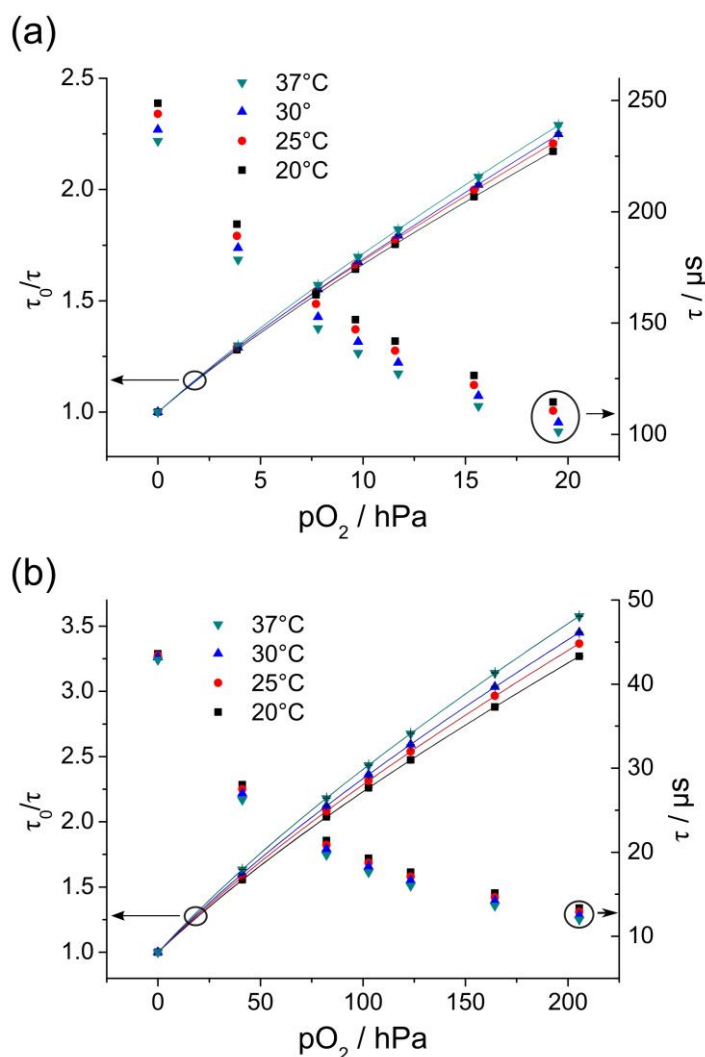
Figure 3.4 Stern-Volmer calibration curves (left Y-axis) and luminescent lifetimes (right Y-axis) (n = 3 measurements) for the integrated trace range [PdTPTBPF, (a)] and normal range [PtTPTBPF, (b)] oxygen optodes at 20 °C, 25 °C, 30 °C and 37 °C. Lines indicate a fit according to equation 3.1.

PdTPTBPF and PtTPTBPF were used because of their high brightness, excellent photostability and ideal spectral properties [36]. These dyes are excitable with red light, emit in the near infrared and therefore fulfil all the spectral requirements given by the used oxygen meters. Photostability tests of sensor spots (PtTPTBPF, 100 µm in diameter) revealed that illumination with a USB oxygen meter (Piccolo2) equipped with a focusing lens at maximum LED intensity resulted in no signal drift over more than 32 000 measurements points (corresponds to 9 hours of continuous measurement at a measurement frequency of 1 measurement point per second, SI Fig. 3.8). Long-wavelength (above 600 nm) excitable and emissive indicators offer the advantage of less background fluorescence or scattering from polymer chips or biological matter (cells,

proteins etc.). Moreover, excitation with red-light is less harmful to cells in comparison to UV or blue light.

3.3.2 Modification of measurement devices

The high brightness of the used dyes is beneficial for microfluidic applications because read out can be performed with standard optical fibres although the sensor areas are typically < 1 mm^2. In addition, we modified a commercially available USB oxygen meter (Piccolo2) with a gradient index lens to enhance the signal intensities by a factor of approx. 20 for smaller sensing areas (< 0.05 mm^2). Furthermore, the Piccolo2 with the lens gave excellent signal-to-noise ratios of more than 500 for a sensor spot (200 µm in diameter) in close proximity (distance < 0.5 mm, SI Fig. 3.11). This set-up thus offers the possibility of measuring even smaller sensor structures. Note that with decreasing sensor spot size the positioning of the measurement device requires more accurate and sophisticated set-ups. The advantage of the gradient index lens is that it focuses the excitation light exactly onto a sensing spot and thus enhances the signal intensities. The focused excitation light has approximately a diameter of 80 µm (SI Fig. 3.9). Further, we studied the influence of the distance between the measurement fibre and a sensor spot on the signal intensity (SI Fig. 3.10-3.11). The distance between different fibres and sensor spots (200 µm or 1.4 mm in diameter) in water was adjusted by a xyz-micromanipulator and the signal intensities were recorded. Fibres with small diameters or fibres equipped with a lens provide high signal intensities at distances close to the sensor spot, but the collection of the emission light is less effective when the distances become longer. Hence, these systems are better suited for sensor spots which are in close proximity to the fibre/lens. The FireStingO2 oxygen meter offers the possibility that up to four sensor spots can be measured simultaneously compared to the Piccolo2 which scores with its smaller dimensions instead. In principle all of the used oxygen meters offer the advantage of being small, inexpensive and allowing accurate readout via luminescent lifetime measurements in the frequency domain, which is less prone to errors than intensity based methods. The benefit of luminescence lifetime measurements is that changes in the measurement conditions (alignment of the readout device, variations in the thickness of the sensor layer, variations of the intensity of the excitation light or of the incident light) do not result in significant signal changes compared to intensity measurements.

Figure 3.5 Different types of microreactors. Microreactor 1 contained 7 chambers each containing a sensor spot with a diameter of 100 μm, 200 μm or 300 μm. In microreactor 2 the chambers were fully covered by oxygen sensors and microreactor 3 contained the oxygen sensor along the straight microfluidic structures of the channels.

3.3.3 Online monitoring of enzyme reactions

The performance of the sensor- and measurement systems was tested in different glass-silicon microreactors (named *Microreactor 1-3)*. We used two model reactions to deplete the oxygen concentrations within the microreactors namely the oxidation of *beta*-D-glucose to D-glucono-*1,5*-lactone and hydrogen peroxide by glucose oxidase or the oxidation of D-amino acids to a 2-oxo carboxylate, ammonia and hydrogen peroxide by D-amino acid oxidase.

  Microreactor 1 (channel dimensions: 200 μm deep, 100 μm wide; volume: 11.8 μL, Fig. 3.5) contained 7 chambers (dimensions: length 3.5 mm, width 1mm). Each chamber contained a sensing spot (PtTPTBPF) with a diameter of either 100 μm, 200 μm or 300 μm. This demonstrates the miniaturization of the sensor areas. The response time (t_{90}) of these sensing set-ups to a rapid change in oxygen concentration from air saturation to anoxic conditions was approx. 3 s and determined by introducing gaseous nitrogen into the chip. The modified USB-oxygen meter was used as read out device to monitor the oxidation of glucose to D-glucono-δ-lactone and hydrogen peroxide by glucose oxidase at different flow rates [1.2 μL/s, 0.8 μL/s, 0.4 μL/s, 0.2 μL/s; Fig. 3.6 (a)]. The measurement was performed at a 100 μm spot (in diameter) at the fifth chamber

(counted from the inlets). The oxygen concentrations decreased within the microreactor with decreasing flow rate due to the longer residence time of the enzyme which is consuming the oxygen. Furthermore, the pumps stopped and refilled their syringes with either enzyme- or glucose solution before changing to a new flow rate. During this time (approx. 10-30 seconds) the glucose oxidase depleted the oxygen within the chamber which can be monitored online with our set-up [Fig. 3.6 (a)]. Each flow rate was repeated three times and the oxygen concentrations were calculated out of the plateaus. The oxygen concentrations were 119.8 ± 0.7 hPa at 1.2 μL/s, 91.2 ± 0.5 hPa at 0.8 μL/s, 27.3 ± 0.5 hPa at 0.4 μL/s and < 0.6 hPa at 0.2 μL/s.
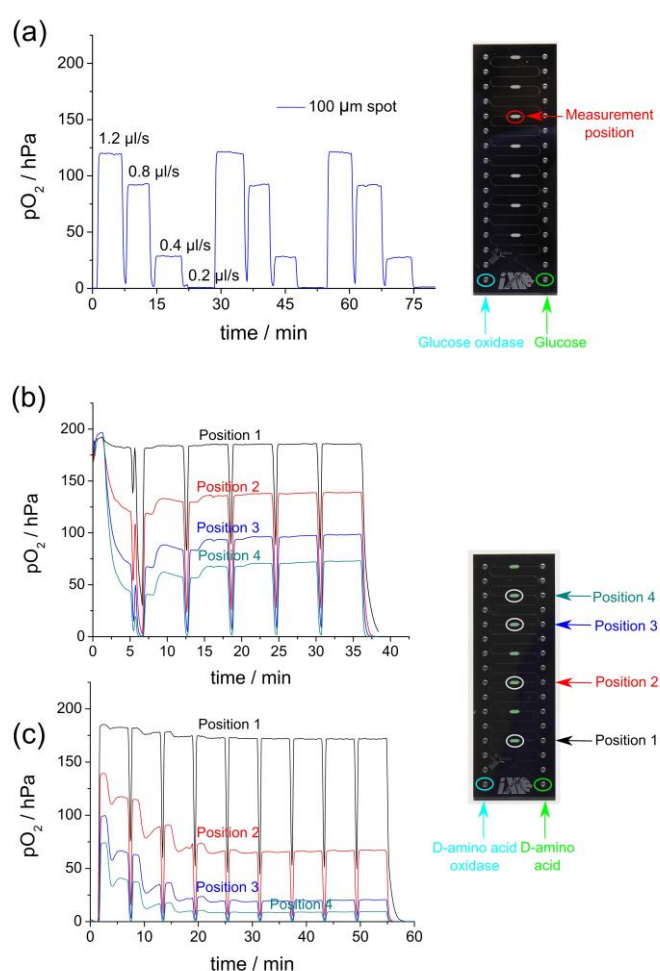
Figure 3.6 Oxidation of glucose (a) to D-glucono-δ-lactone and hydrogen peroxide at flow rates of 1.2 μL/s, 0.8 μL/s, 0.4 μL/s and 0.2 μL/s were performed in microreactor 1. Oxidations of D-alanine (b) and D-phenylalanine (c) by D-amino acid oxidase at a flow rate of 0.6 μL/s were carried out in microreactor 2. All reactions were performed at room temperature.

Microreactor 2 possessed the same characteristics (channel dimensions, response time, PtTPTBPF) as *microreactor 1* but the chambers were fully covered by the oxygen sensor. These sensor chambers allow an easier alignment of the read out system and exhibit

higher signal intensities. Hence the read out could be performed by optical fibres (1 mm in diameter) connected to the 4-channel oxygen meter (FirestingO2). The set-up was used for online monitoring of the oxidation of D-alanine and D-phenylalanine by D-amino acid oxidase [Fig. 3.6 (b) and (c)]. The oxygen depletion was simultaneously determined at four sensing spots which were chosen randomly. The microreactor was first flushed with water and then D-alanine and D-amino acid oxidase were introduced over two separate inlets at a flow rate of 0.6 µL/s (0.3 µL/s per pump). The pumps had to be refilled every 5.6 minutes indicated by the oxygen depletion within the microreactor due to the consumption of oxygen by the enzyme. After approx. 8-15 min (depending on the measurement position) the system (pumps, tubes, solutions and microreactor) was stable and provided consistent oxygen concentrations. After 40 min D-alanine was replaced by D-phenylalanine [6(c)] and it required 20-25 min until the signal was stabilized again. This stabilization time of the microreactor is a function of the fluidic conditions (flow rate, channel geometry) and thus can be adjusted by changing these parameters. The oxygen concentrations for D-alanine and D-phenylalanine are shown in SI Table 1. As expected, D-phenylalanine is oxidized faster than D-alanine [40].

 Microreactor 3 (channel dimensions: 400 µm deep, 200 µm wide, volume: 27.6 µL) did not contain sensing chambers and the oxygen sensor (PtTPTBPF) was directly integrated into the straight microfluidic structures with a width of 200 µm. Its response time (t_{90}) was about 3 s and determined by introducing gaseous nitrogen into the chip. Read out was performed by the 4-channel oxygen meter connected to optical fibres. An enzyme cascade reaction using glucose oxidase to deplete oxygen and catalase to reproduce oxygen was carried out in *microreactor 3* [Fig. 3.7 (a)] and additionally in a modified version of *microreactor 2* [Fig. 3.7 (b)] which contained PdTPTBPF and PtTPTBPF oxygen sensing layers. In detail the first three chambers of the modified version contained the PdTPTBPF sensors and the other four contained the PtTPTBPF sensors. The oxygen concentrations were simultaneously determined at four sensing areas (Fig. 3.7). Glucose and glucose oxidase were introduced separately over the two main inlets and catalase over a lateral inlet after the first two measurement areas. The third pump with catalase solution was switched on and off alternately (I and II in Fig. 3.7) to see the difference when the catalase is present/absent. It can be seen from Fig. 3.7 that the oxygen concentrations decrease from the first to the second measurement position. At the third position the oxygen concentration is increased when the third pump was switched on because of the introduction of air saturated catalase solution into the microreactor. At the fourth measurement position the oxygen levels are decreased again even when the third pump is switched on because the glucose oxidase is consuming the oxygen faster than the catalase can reproduce it. We indirectly tested the function of the catalase in

another experiment by introducing just air saturated buffer over the lateral inlet and confirmed that the oxygen concentration at the third and fourth measurement position without catalase is significantly lower. The oxygen concentrations at different measurement positions are shown in SI Table 2. As mentioned above the syringe pumps had to be refilled and therefore stopped pumping. The peak at approximately 10 min in Fig. 3.7 (a) derived because catalase was introduced into the microreactor while the two other pumps stopped for refilling.

The enzyme reactions demonstrate that this measurement set-up is ideally suited for online monitoring of oxygen within microfluidic devices. The oxygen impermeability of the glass-silicon microreactor is beneficial compared to devices from PDMS or other polymeric materials because it avoids disturbing the oxygen intake from the surrounding chip material. Our microreactor system thus enables the investigation of oxygen depletion reactions within microfluidic devices and provides a useful tool for determining kinetic parameters at µ-scale in the future.
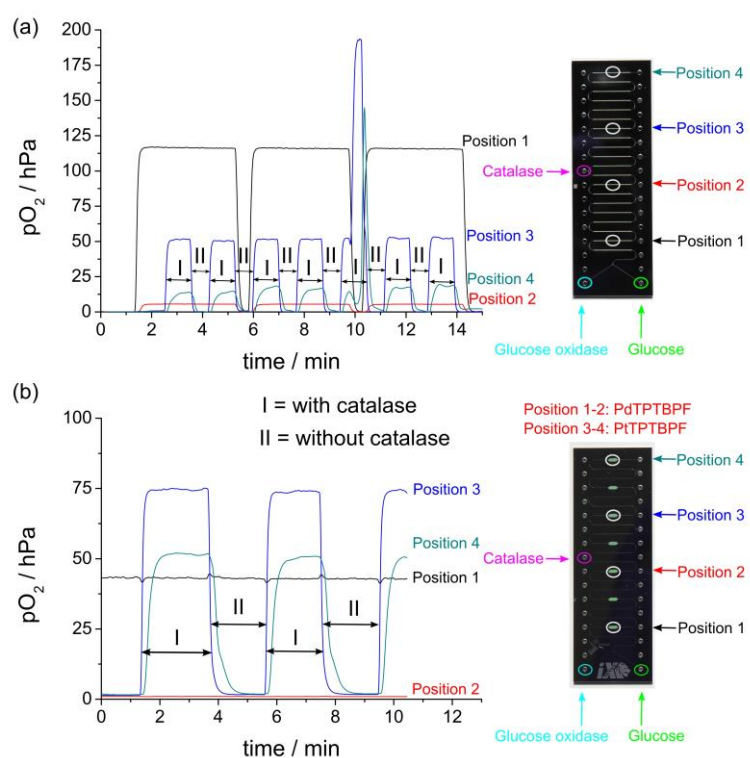
Figure 3.7 Oxidation of glucose by glucose oxidase to D-glucono-δ-lactone and hydrogen peroxide, which was alternating reconverted into oxygen by adding catalase. Reactions were performed at room temperature in microreactor 3 (a) and a modified version of microreactor 2 (b). Pumps were operated at a flow rate of 0.1 µL/s.

3.4 Conclusion

In summary, we report a powerful measurement-set up for microfluidic applications consisting of NIR-emitting optical oxygen sensors and an inexpensive and robust readout via commercially available oxygen meters adapted with gradient index lenses to enhance the signal intensities. The set-up enables the determination of oxygen up to a resolution of 0.06-0.22 hPa (approx. 3-9 µg/l of dissolved oxygen). Furthermore, the sensitivity of the sensor can be easily adjusted by the integration of different oxygen indicator dyes. Moreover, the integration and patterning of sensor layers into microreactors was demonstrated by automated airbrush spraying, a versatile method. Our fabricated microreactors consisted of silicon-glass composites, contained integrated oxygen sensor down to a size of 100 µm in diameter and were used to monitor enzyme reactions. In contrast to common polymeric chip materials, silicon and glass offer the advantage of being impermeable for oxygen and therefore the effect of the bulk material on the oxygen concentration is negligible. The microreactors can be used in future for kinetic studies of oxygen consuming or producing enzyme reactions, cell based respiration measurements or organ-on-chip applications.

3.5 References

(1) Fletcher, Paul D. I.; Haswell, S. J.; Pombo-Villar, E.; Warrington, B. H.; Watts, P.; Wong, Stephanie Y. F.; Zhang, X. *Tetrahedron*, **2002**, *58* (24), 4735–4757.

(2) Peterson, D. S.; Rohr, T.; Svec, F.; Fréchet, Jean M. J. *Anal. Chem.*, **2002**, *74* (16), 4081–4088.

(3) Seong, G. H.; Heo, J.; Crooks, R. M. *Anal. Chem.*, **2003**, *75* (13), 3161–3167.

(4) Kerby, M. B.; Legge, R. S.; Tripathi, A. *Analytical chemistry*, **2006**, *78* (24), 8273–8280.

(5) Lee, Harry L T; Boccazzi, P.; Ram, R. J.; Sinskey, A. J. *Lab Chip*, **2006**, *6* (9), 1229–1235.

(6) Mehta, G.; Lee, J.; Cha, W.; Tung, Y.-C.; Linderman, J. J.; Takayama, S. *Anal. Chem.*, **2009**, *81* (10), 3714–3722.

(7) Lam, Raymond H W; Kim, M.-C.; Thorsen, T. *Anal. Chem.*, **2009**, *81* (14), 5918–5924.

(8) Lee, K. S.; Boccazzi, P.; Sinskey, A. J.; Ram, R. J. *Lab on a chip*, **2011**, *11* (10), 1730–1739.

(9) Pfeiffer, S. A.; Nagl, S. *Methods Appl. Fluoresc.*, **2015**, *3* (3), 34003.

(10) Sun, S.; Ungerböck, B.; Mayr, T. *Methods Appl. Fluoresc.*, **2015**, *3* (3), 34002.

(11) Grist, S. M.; Chrostowski, L.; Cheung, K. C. *Sensors (Basel)*, **2010**, *10* (10), 9286–9316.

(12) Demas, J. N.; Diemente, D.; Harris, E. W. *J. Am. Chem. Soc.*, **1973**, *95* (20), 6864–6865.

(13) Timpson, C. J.; Carter, C. C.; Olmsted, J. *J. Phys. Chem.*, **1989**, *93* (10), 4116–4120.

(14) Fuller, Z. J.; Bare, W. D.; Kneas, K. A.; Xu, W.-Y.; Demas, J. N.; DeGraff, B. A. *Anal. Chem.*, **2003**, *75* (11), 2670–2677.

(15) Ungerbock, B.; Fellinger, S.; Sulzer, P.; Abel, T.; Mayr, T. *The Analyst*, **2014**, *139* (10), 2551–2559.

(16) Sin, A.; Chin, K. C.; Jamil, M. F.; Kostov, Y.; Rao, G.; Shuler, M. L. *Biotechnol. Prog.*, **2004**, *20* (1), 338–345.

(17) Vollmer, A. P.; Probstein, R. F.; Gilbert, R.; Thorsen, T. *Lab Chip*, **2005**, *5* (10), 1059–1066.

(18) Lam, Raymond H W; Kim, M.-C.; Thorsen, T. *Anal. Chem.*, **2009**, *81* (14), 5918–5924.

(19) Nock, V.; Blaikie, R. J.; David, T. *Lab Chip*, **2008**, *8* (8), 1300–1307.

(20) Nock, V.; Alkaisi, M.; Blaikie, R. J. *The 35th International Conference on Micro- and Nano-Engineering (MNE)*, **2010**, *87* (5–8), 814–816.

(21) Etzkorn, J. R.; Wu, W.-C.; Tian, Z.; Kim, P.; Jang, S.-H.; Meldrum, D. R.; Jen, A. K.-Y.; Parviz, B. A. *J. Micromech. Microeng.*, **2010**, *20* (9), 95017.

(22) Molter, T. W.; McQuaide, S. C.; Suchorolski, M. T.; Strovas, T. J.; Burgess, L. W.; Meldrum, D. R.; Lidstrom, M. E. *Sensors and actuators. B, Chemical*, **2009**, *135* (2), 678–686.

(23) Zanzotto, A.; Szita, N.; Boccazzi, P.; Lessard, P.; Sinskey, A. J.; Jensen, K. F. *Biotechnology and bioengineering*, **2004**, *87* (2), 243–254.

(24) Szita, N.; Boccazzi, P.; Zhang, Z.; Boyle, P.; Sinskey, A. J.; Jensen, K. F. *Lab on a chip*, **2005**, *5* (8), 819–826.

(25) Zanzotto, A.; Boccazzi, P.; Gorret, N.; Van Dyk, Tina K; Sinskey, A. J.; Jensen, K. F. *Biotechnology and bioengineering*, **2006**, *93* (1), 40–47.

(26) Thomas, P. C.; Halter, M.; Tona, A.; Raghavan, S. R.; Plant, A. L.; Forry, S. P. *Anal. Chem.*, **2009**, *81* (22), 9239–9246.

(27) Thomas, P. C.; Raghavan, S. R.; Forry, S. P. *Anal. Chem.*, **2011**, *83* (22), 8821–8824.

(28) Ungerbock, B.; Charwat, V.; Ertl, P.; Mayr, T. *Lab Chip*, **2013**, *13* (8), 1593–1601.

(29) Gitlin, L.; Hoera, C.; Meier, R. J.; Nagl, S.; Belder, D. *Lab Chip*, **2013**, *13* (20), 4134–4141.

(30) Grist, S. M.; Oyunerdene, N.; Flueckiger, J.; Kim, J.; Wong, P. C.; Chrostowski, L.; Cheung, K. C. *Analyst*, **2014**, *139* (22), 5718–5727.

(31) Lasave, L. C.; Borisov, S. M.; Ehgartner, J.; Mayr, T. *RSC Adv*, **2015**, *5* (87), 70808–70816.

(32) Thete, A. R.; Gross, G. A.; Henkel, T.; Koehler, J. M. *Chemical Engineering Journal*, **2008**, *135* (Supplement 1), 327–332.

(33) Thete, A. R.; Gross, G. A.; Koehler, J. M. *The Analyst*, **2009**, *134* (2), 394–400.

(34) Herzog, C.; Beckert, E.; Nagl, S. *Analytical chemistry*, **2014**, *86* (19), 9533–9539.

(35) Poehler, E.; Herzog, C.; Suendermann, M.; Pfeiffer, S. A.; Nagl, S. *Eng. Life Sci.*, **2015**, *15* (3), 276–285.

(36) Borisov, S. M.; Nuss, G.; Klimant, I. *Anal. Chem.*, **2008**, *80* (24), 9435–9442.

(37) Borisov, S. M.; Zenkl, G.; Klimant, I. *ACS Appl. Mater. Interfaces*, **2010**, *2* (2), 366–374.

(38) Müller, B. J.; Burger, T.; Borisov, S. M.; Klimant, I. *Sensors and Actuators B: Chemical*, **2015**, *216*, 527–534.

(39) Demas, J. N.; DeGraff, B. A.; Xu, W. *Anal. Chem.*, **1995**, *67* (8), 1377–1380.

(40) D'Aniello, A.; Vetere, A.; Petrucelli, L. *Comparative Biochemistry and Physiology Part B: Comparative Biochemistry*, **1993**, *105* (3–4), 731–734.

3.6 Supplementary Information
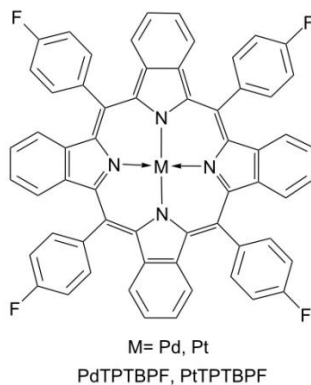
SI Figure 3.1 Chemical structures of the used oxygen indicator dyes palladium(II) and platinum(II) meso-tetra(4-fluorophenyl) tetrabenzoporphyrin (PdTPTBPF and PtTPTBPF).
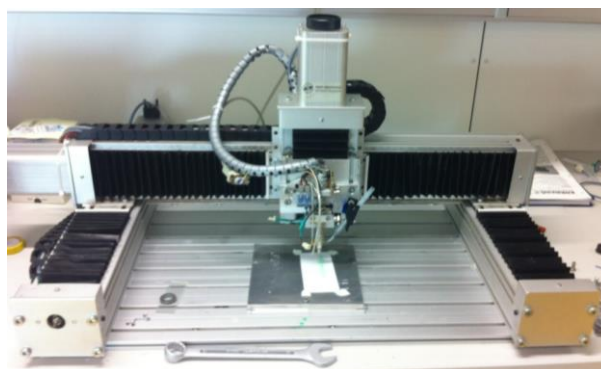
SI Figure 3.2 Computerized numerical control (CNC) air-brush spraying device. The spraying device consists of an airbrush (EFBE Spritzautomat 1/2L) fixed to an x-y-z table actuated by stepper motors.
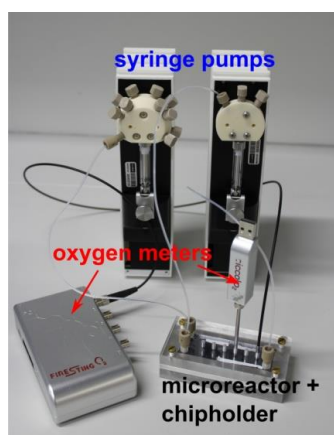
SI Figure 3.3 Measurement set-up consisting of the microreactor, chip holder, syringe pumps, FirestingO2 equipped with a 1 mm fibre and a Piccolo2.
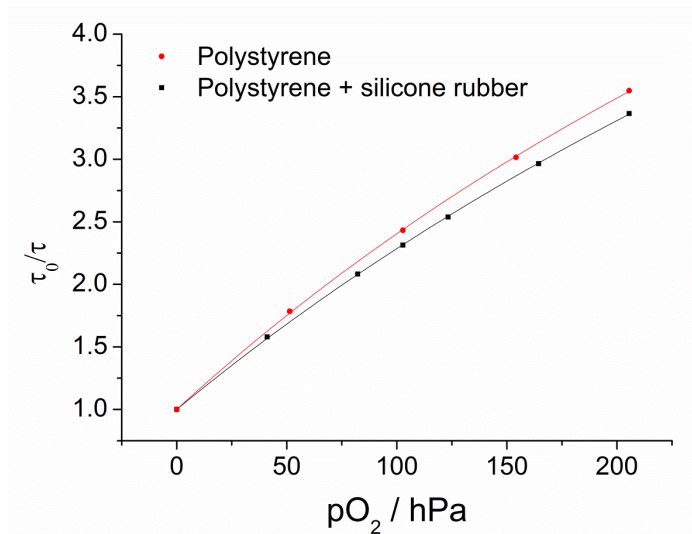
SI Figure 3.4 Calibration curves for PtTPTBPF based sensors at room temperature. The dye was incorporated into a polystyrene matrix and into a polystyrene/silicone rubber composite matrix.
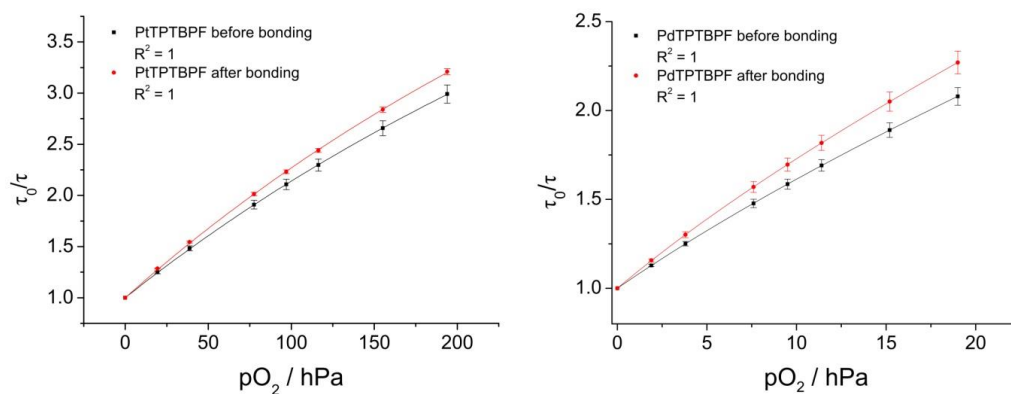
SI Figure 3.5 Calibration curves of independently manufactured sensing layers combined in one calibration (n = 8 for PtTPTBPF and n = 3 for PdTPTBPF) before and after bonding at room temperature.
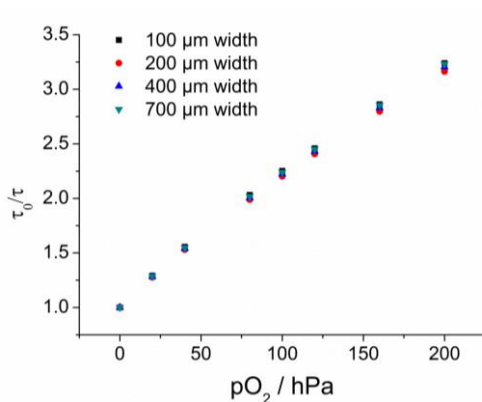
SI Figure 3.6 Calibration points of different sensor lines (PtTPTBPF, various sizes) at room temperature.
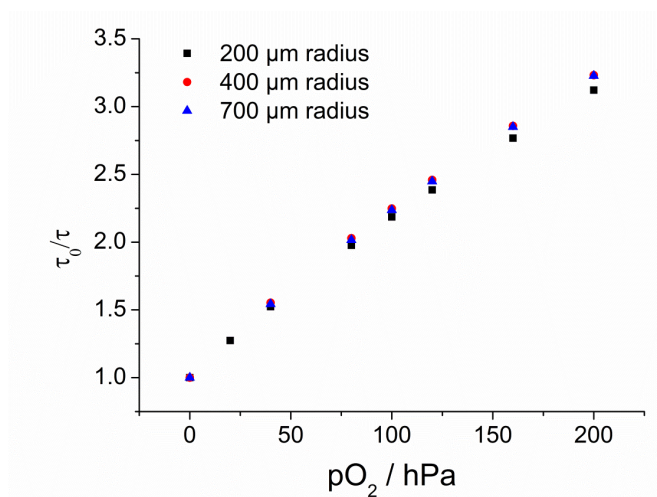
SI Figure 3.7 Calibration points of different sensor spots (PtTPTBPF, various sizes) at room temperature.
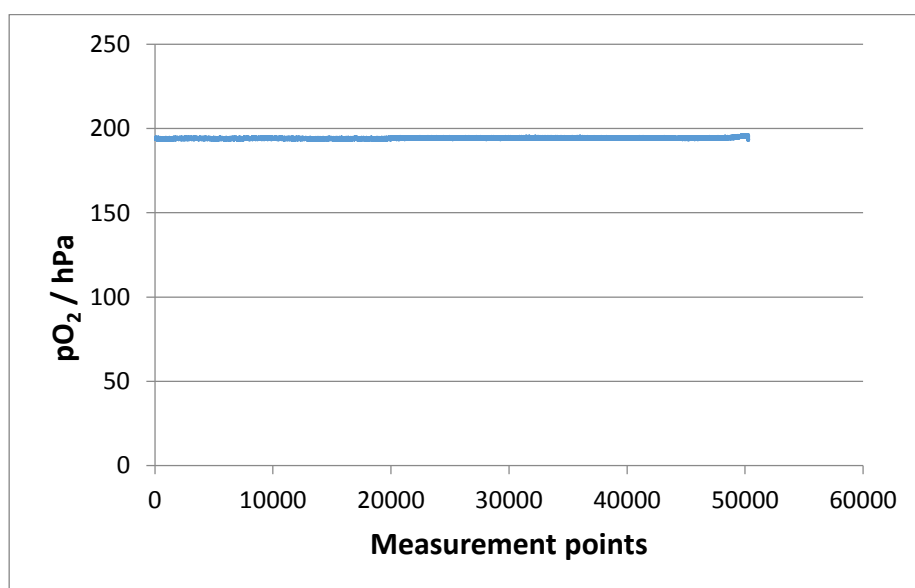
SI Figure 3.8 Long term measurement of a 100 µm sensor spot with an USB oxygen meter (Piccolo2) equipped with a focusing lens at an LED intensity of 100%. Oxygen partial pressure was calculated from phase shift measurements.
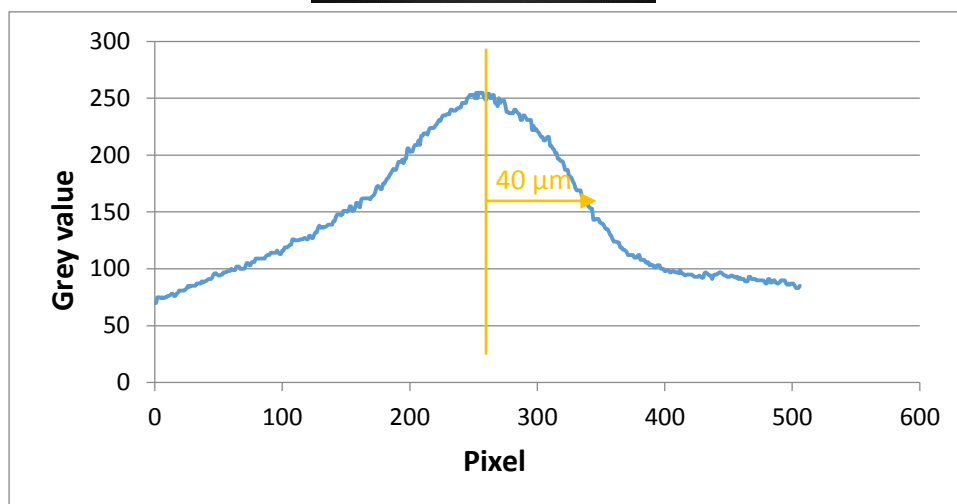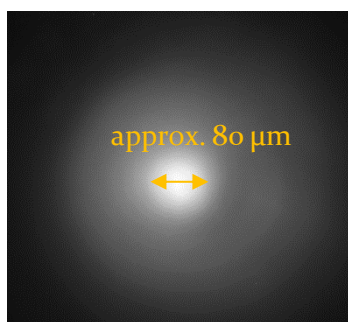
SI Figure. 3.9 Focusing area of the USB oxygen meter equipped with a gradient index lens. The end of the lens was placed on a planar oxygen optode and the emission light was detected with an inverse microscope equipped an imaging system.
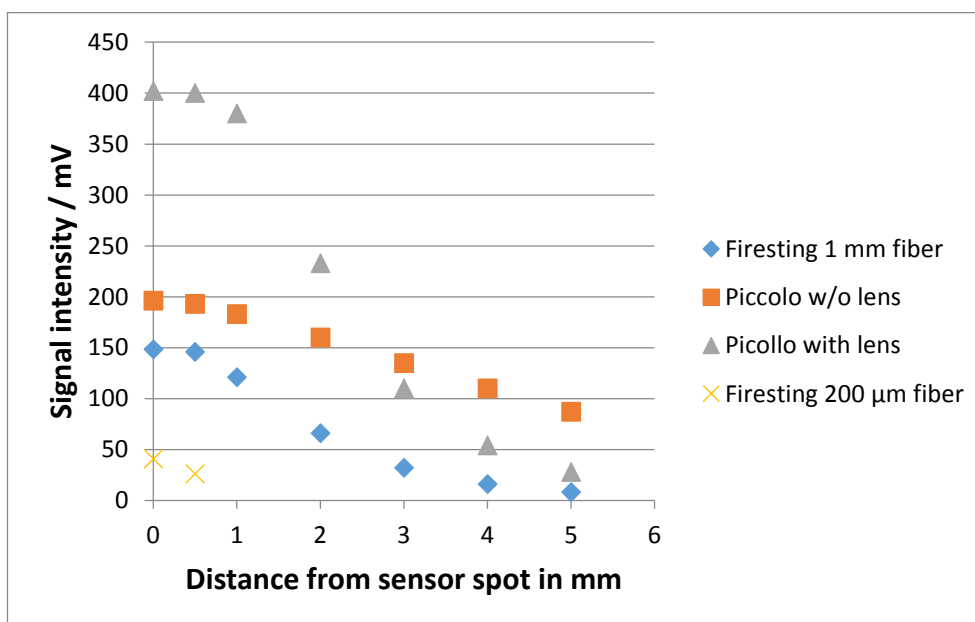
SI Figure 3.10 Signal intensities of different measurement set-ups at a sensor spot (1.4 mm in diameter). The distance of the oxygen meter to the sensor spot in water was adjusted by a xyz-micromanipulator. Measurements were carried out at a LED intensity of 10 % and an amplification of 400x.
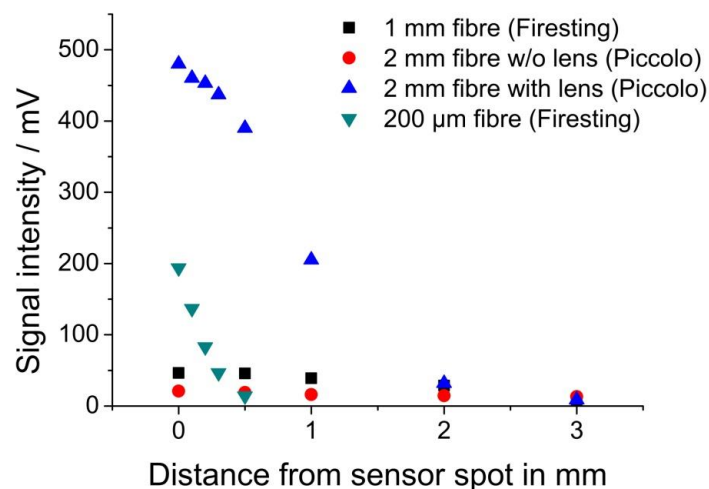
SI Figure 3.11 Signal intensities of a sensor spot (200 µm in diameter) measured with an oxygen meter equipped with 1 mm or 200 µm optical fibres, and an USB oxygen meter equipped with a 2 mm fibre or a 2 mm fibre with a focusing lens. The distance of the oxygen meter to the sensor spot in water was adjusted by a xyz-micromanipulator. Measurements were carried out at a LED intensity of 100% and an amplification of 400x.

SI Table 3.1 Oxygen concentrations for the oxidation of D-alanine or D-phenylalanine by D-amino acid oxidase at four measurement positions.

Measurement position	D-alanine	D-phenylalanine
1	185.4 ± 0.3 hPa	171.7 ± 0.3 hPa
2	138.2 ± 0.5 hPa	66.5 ± 0.6 hPa
3	97.1 ± 1.0 hPa	20.1 ± 0.4 hPa
4	71.6 ± 1.0 hPa	9.1 ± 0.2 hPa

SI Table 3.2 Oxidation of glucose by glucose oxidase to D-glucono-δ-lactone and hydrogen peroxide, which was alternating reconverted into oxygen by adding catalase. Reactions were performed in microreactor 3 and a modified version of microreactor 2. *instead of a catalase solution only buffer without catalase was introduced. **Trace oxygen sensors (PdTPTBPF).

Measurement position	Microreactor 3	Microreactor 2	Microreactor 2 buffer*
1	116.0 ± 0.5 hPa	43.0 ± 0.2 hPa**	44.7 ± 0.5 hPa**
2	5.5 ± 0.2 hPa	0.96 ± 0.06 hPa**	1.01 ± 0.06 hPa**
3 /on	51.8 ± 0.5 hPa	74.2 ± 0.5 hPa	56.0 ± 0.6 hPa
3 off	< 0.6 hPa	< 0.6 hPa	-
4 /on	16.2 ± 2.6 hPa	49.1 ± 0.5 hPa	10.6 ± 0.6 hPa
4 / of	< 0.6 hPa	< 0.6 hPa	-

4 Simultaneous determination of oxygen and pH inside microfluidic devices using core-shell nanosensors

Authors: Josef Ehgartner [a], Martin Strobl [a], Juan M. Bolivar [b], Dominik Rabl [a], Mario Rothbauer [c], Peter Ertl [c], Sergey M. Borisov [a], Torsten Mayr [a]

[a] Institute of Analytical Chemistry and Food Chemistry, Graz University of Technology, NAWI Graz, Stremayrgasse 9/3, 8010 Graz, Austria.
[b] Institute of Biotechnology and Biochemical Engineering, Graz University of Technology, NAWI Graz, Petersgasse 12/1, 8010 Graz, Austria.
[c] Institute of Applied Synthetic Chemistry, Vienna University of Technology, Getreidemarkt 9/163, 1060 Wien, Austria.

Abstract A powerful online analysis set-up for the simultaneous detection of oxygen and pH is presented. It features core-shell nanosensors, which enable contactless and inexpensive read-out using adapted oxygen meters via modified dual lifetime referencing in the frequency domain (phase shift measurements). Lipophilic indicator dyes were incorporated into core-shell structured poly(styrene-block-vinylpyrrolidone) nanoparticles (average diameter = 180 nm) yielding oxygen nanosensors and pH nanosensors by applying different preparation protocols. The oxygen indicator platinum(II) meso-tetra(4-fluorophenyl) tetrabenzoporphyrin (PtTPTBPF) was entrapped into the polystyrene core (oxygen nanosensors) and a pH sensitive BF_2-chelated tetraarylazadipyrromethene dye (aza-BODIPY) was incorporated into the polyvinylpyrrolidone shell (pH nanosensors). The brightness of the pH nanoparticles was increased by more than 3 times using a light harvesting system. The nanosensors have several advantages such as being excitable with red light, emitting in the near-infrared spectral region, showing a high stability in aqueous media even at high particle concentrations, high ionic strength or high protein concentrations, and are spectrally compatible with the used read-out device. The resolution for oxygen of the set-up is 0.5-2.0 hPa (approx. 0.02-0.08 mg/L of dissolved oxygen) at low oxygen concentrations (< 50 hPa) and 4-8 hPa (approx. 0.16-32 mg/L of dissolved oxygen) at ambient air oxygen concentrations (approx. 200 hPa at 980 mbar air pressure) at room temperature. The pH

resolution is 0.03-0.1 pH units within the dynamic range (apparent pK_a 7.23 ± 1.0) of the nanosensors. The sensors were used for online monitoring of pH changes during the enzymatic transformation of Penicillin G to 6-aminopenicillanic acid catalysed by Penicillin G acylase in miniaturized stirred batch reactors or continuous flow microreactors

4.1 Introduction

Miniaturized laboratory systems (lab-on-a-chip technologies) using microfluidic devices are useful tools for various scientific and industrial fields such as cell culturing [1], organ-on-a-chip applications [2], biomedical research [3,4] or organic synthesis [5]. Human individuals around the world benefit from progress in microfluidics even if the appropriateness of lab-on-a-chip technologies has to be reassessed for some applications. Developments such as diagnostic devices for low resource environments [3], more physiologically relevant in vitro models [4], high throughput cell screening methods [6] or chemical synthesis procedures under harsh reaction conditions [5] are now available due to the advancements in microfluidic technologies. Faced with these advances, however, analytical chemists are challenged to find new methods to determine analytes accurately within lab-on-a-chip devices [7]. The use of luminescent sensors can be one useful technique for obtaining online and real-time analytical data of small molecules (ions, glucose etc.) or process parameters (pH, oxygen and temperature) at this miniaturized scale. Luminescent sensors are highly suited for microfluidic applications due to their high sensitivity, ability of contactless read-out, ease of miniaturization, availability of various sensor formats (e.g. integrated sensor films, nanoparticles etc.) and their low cost [8–10]. However, efforts are necessary to develop sensor and read-out systems for lab-on-a-chip applications which are reliable, simple to use, easily accessible and in the best case capable of multi-analyte detection. A recent review covers most of the developments in the field of integrated luminescence sensors within microfluidic devices [8] and two other reviews specialised on optical oxygen sensors give an additional insight into other sensor formats, for example oxygen-sensitive nanoparticles [9,10]. In a newer report, Poehler et al. [11] showed the integration of a fluorescent pH sensor layer into a microfluidic chip for continuous electrophoretic separation of biomolecules via free flow isoelectric focussing. Further, Grist et al. [12] recently designed a microfluidic device with integrated ratiometric oxygen sensors for controlling the oxygen concentrations within the chip for long-term cell culture applications. Recently, we demonstrated the application of optical oxygen sensors in a microfluidically perfused three dimensional human liver model [13] and in microfluidic droplets for cell culture experiments [14]. Moreover, we recently presented two novel techniques for the integration of optical oxygen sensors into glass-based microfluidic

devices and introduced two miniaturized read-out devices based on luminescent lifetime measurements in the frequency domain (phase shifts) for lab-on-a-chip applications [15,16]. Due to our recent developments and gained knowledge of luminescence sensing in microfluidic devices we aimed to develop a measurement system which is able to simultaneously determine the key process parameters pH and dissolved oxygen (DO). Therefore, we decided to use a frequency-domain luminescence lifetime-based method referred to as modified dual lifetime referencing (m-DLR)[17,18] . This method relies on measurement of the overall phase shift of two luminescence indicators with largely different luminescent lifetimes (e.g. pH and oxygen indicator) at two different modulation frequencies. We refer the reader to a recent review of time-resolved luminescence determination methods for further information about different techniques [19]. The m-DLR method is a self-referencing technique which only determines relative contributions between the two luminescence indicators; therefore it is less prone to errors compared to simple intensity based methods. A recent mini-review summarises the current state of the art of pH and DO sensors that are applied to bioprocesses from microfluidic systems to benchtop scale [20]. To our knowledge no m-DLR system for simultaneously sensing of pH and oxygen in microfluidic devices was presented so far in literature and only few macroscopic investigations for simultaneously sensing of pH and DO based on m-DLR techniques are described in literature [17,21,22]. In addition, all former studies are based on sensor films. Hence, we investigated a m-DLR set-up for the simultaneous determination of oxygen and pH in microfluidic devices based on core-shell nanosensors and miniaturized oxygen meters [16]. The presented system offers the advantage over former reports that it uses red light excitation, emits in the near infrared, which causes less background fluorescence or scattering from chip materials or biological matter, possesses higher photostability and uses nanosensors, which can be used in microfluidic devices without an integration step in comparison to sensor films. The poly(styrene-block-vinylpyrrolidone) core-shell nanosensors are ideally suited for different applications due to their low toxicity to cells and high stability in aqueous media even if high particle concentrations (20 mg/mL), high ionic strength or high protein concentrations are used. Moreover, the two different polymeric domains of the particles have complementary properties; therefore allowing their use as oxygen and pH nanosensors. The in-house prepared oxygen and pH indicator dyes show high brightness (BS = ε * quantum yield), are excitable with red light and emit in the near infrared, a spectral region where fewer compounds emit. Moreover, the dyes are very lipophilic which enables physical entrapment inside the nanoparticles and are compatible with the used read-out device. Further, a light harvesting system was applied in order to enhance the brightness of the pH nanosensors which additionally allows ratiometric imaging. We applied this set-up for real-time monitoring of pH changes during the enzymatic

transformation of Penicillin G to 6-aminopenicillanic acid catalysed by Penicillin G acylase in microreactors.

4.2 Experimental

4.2.1 Materials

Platinum(II) *meso*-tetra(4-fluorophenyl) tetrabenzoporphyrin (PtTPTBPF), 2,3-bis(3,3,9,9-tetramethyl-2-hydroxyjulolidine)but-2-enedinitrile (Schiff base) and BF_2-chelated tetraarylazadipyrromethene dye (aza-BODIPY) were synthesized in-house according to the literature procedures (for chemical structures see Fig. 4.1) [23–26]. For preparation of the Zn-Schiff base see supplementary information (SI).

Poly(stryrene-block-1-vinylpyrrolidone) (PSPVP, 38 % dispersion in water, consist of 64% w/w of styrene and 36% w/w of vinylpyrrolidone and are <500 nm in size), sodium dihydrogen phosphate (≥99.0%, anhydrous), glucose oxidase from *Aspergillus niger* and zinc acetate dihydrate were purchased from Sigma Aldrich.

Poly(vinylidene chloride-co-acrylonitrile) (PViCl-PAN, 20% w/w polyacrylonitrile, 125 000 g/mol) was bought from Scientific Polymer products, Inc. (scientificpolymer.com). Penicillin G acylase (PGA) from *E. coli* and Penicillin G (PenG) were a kind gift from Prof. Guisan (ICP-CSIC, Spain).

Tetrahydrofuran (≥99.5% p.a.), acetic acid (100%, p.a.) sodium hydroxide, sodium sulphite, D-glucose and buffer salts (CAPS and CHES) were obtained from Carl Roth (www.carl-roth.de). Sodium chloride and hydrochloric acid (1 M) were bought from VWR (Vienna, Austria). N-Methyl-2-pyrrolidone (99.5%, peptide grade) was purchased from ABCR (www.abcr.de). Ethanol (99.9%) was bought from AustrAlco (www.australco.at). Nitrogen, oxygen and synthetic air (all of 99.999% purity) were obtained from Linde (Graz, Austria). Ultrapure water (Milli-Q) was used throughout the study.
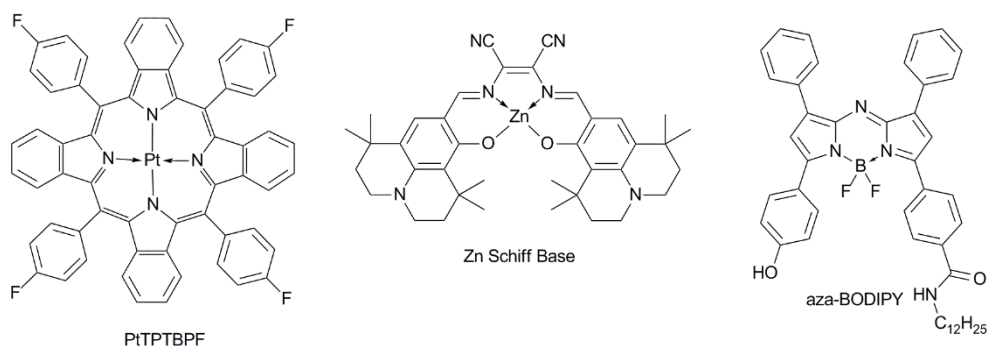
Figure 4.1 Chemical structures of the oxygen indicator (PtTPTBPF), the antenna dye (Zn-Schiff base) and the pH indicator (aza-BODIPY).

4.2.2 Preparation of PSPVP nanoparticles for oxygen sensing

PSPVP nanoparticle dispersion (526 mg dispersion containing 200 mg of particles) was diluted with water (50 mL) and THF (30 mL). The mixture was stirred and THF (20 mL) containing PtTPTBPF (2 mg) was added dropwise. All THF and partly water were removed under reduced pressure to a final volume of approximately 20-30 mL. The particle concentration of the oxygen nanosensor stock dispersion was approx. 7-10 mg/mL.

4.2.3 Preparation of PSPVP nanoparticles for pH sensing

PSPVP nanoparticle dispersion (526 mg containing 200 mg of particles) was diluted with water (50 mL) and ethanol (40 mL). Aza-BODIPY dye (250 µL of a 1 mg/mL stock solution in THF, Fig. 4.1) and Zn-Schiff base (500 µL of a 1 mg/mL stock solution in THF) were added to a solution of ethanol (20 ml) and this mixture was then added dropwise over 1 min to the nanoparticle dispersion while stirring. Ethanol and water were removed under reduced pressure to a final volume of approx. 13-20 mL. The particle concentration of the pH nanosensor stock dispersion was approx. 10-15 mg/mL. The same particles were also prepared without Zn-Schiff base. Also particles with different aza-BODIPY to Zn-Schiff base ratios were prepared accordingly (see SI Tab. 4.1).

4.2.4 Measurements

MALDI-TOF mass spectra were recorded on a Micromass TofSpec 2E (further details see SI). ^{1}H and ^{13}C spectra were recorded on a Bruker Avance III 300 MHz Spectrometer at 300 (^{1}H) and 75 (^{13}C) MHz. Absorption spectra were measured at a Cary 50 UV–VIS spectrophotometer (Varian). Emission spectra were acquired on a Hitachi Model F-7000 fluorescence spectrometer (Japan) equipped with a red-sensitive photomultiplier R 9876 from Hamamatsu (Japan). The size of the beads was determined with a particle size analyzer Zetasizer Nano ZS (www.malvern.de) or with a transmission electron microscope (FEI Tecnai F20, further details see SI). Light conditioning experiments were performed with an LED array containing 12 LEDs [OSRAM Oslon SSL 80 red (625 nm) on a round printed circuit board (www.LED-TECH.de)] at an irradiance of approx. 950-1150 W m^{-2}. The pH of buffer solutions (acetate, phosphate, CAPS and CHES each 40 mM) was adjusted with a pH meter (SevenCompact, Mettler-Toledo, Switzerland) equipped with a glass electrode (InLab Nano or Inlab Micro, Mettler Toledo, Switzerland). The glass electrode was calibrated with standard buffers of pH 4.01, pH 7.01 and pH 10.01 (Hanna instruments, www.hannainst.com). The buffers were adjusted at constant ionic strength (IS = 0.30 M, 0.20 M and 0.15 M) using sodium chloride as a background electrolyte. Two mass flow controller instruments (Read Y smart series) by

Vögtlin instruments (www.voegtlin.com) were used to obtain gas mixtures of defined oxygen partial pressures (pO_2). Compressed air, and nitrogen were used as calibration gases.

The activity of soluble and immobilized Penicillin G acylase (PGA) was determined spectrophotometrically by using 6-nitro-3-phenylacetamide benzoic acid (NiPAB) as substrate and additionally by direct quantification of Penicillin G (PenG) hydrolysis (further details see SI).

4.2.5 Characterization of nanosensors for the simultaneous determination of pH and oxygen

A dispersion containing a mixture of oxygen nanosensors (ca. 1.2 mg/mL) and pH nanosensors (ca. 5 mg/mL) was prepared. The dispersion was conditioned with light for 10 min prior to the characterization. The conditioned stock dispersion (0.5 mL) was diluted with water (0.5 mL) and buffer solution (1 mL, 40 mM of either acetate, phosphate, CAPS or CHES, IS of either 0.30 M, 0.20 M or 0.15 M) was added in order to obtain various pH calibration standards at different ionic strength. The final pH of the calibration standards was determined with a pH electrode. Measurements were performed in glass vials at different temperatures or inside microreactors (channel width: 200 µm, channel depth: 400 µm, see SI Fig. 4.12-4.13) at room temperature (approx. 23°C). The oxygen concentration within the calibration standards was adjusted by flushing them with defined gas mixtures of compressed air and nitrogen. Additionally, deoxygenated buffer dispersions were prepared by adding glucose oxidase and glucose or sodium sulphite to the dispersions. A temperature sensor connected to the temperature port of a FireStingO2 (Pyro-Science, Germany) was used to monitor the temperature during measurements. A modified optical oxygen meter (Piccolo2, Pyro-Science, Germany) including a stainless steel tube with an optical fiber (2 mm in diameter) was used for recording the phase shifts (luminescent lifetime measurements in the frequency domain) of the nanosensors. The phase shifts were recorded at two modulation frequencies (m_1 = 2000 Hz, m_2 = 8000 Hz, measurement duration 16 ms per frequency to enable dual parameter detection). A measurement software was provided from Pyro-Science. The optical fiber of the optical meter was adapted with a GRadient INdex (GRIN) lens (www.grintech.de) to enhance the signal intensities for measurements within microreactors by focusing the excitation light into the microchannel. The microreactors were connected *via* an in-house developed chip holder to syringe pumps (Cavro® Centris pumps from Tecan, www.tecan.com), which were operated by a Lab VIEW program (www.ni.com/labview). Long term measurements of light conditioned nanosensors (light conditioning for 10 min) were also performed to study the influence of the excitation light of the measurement device on the

nanosensors; hence more than 9000 measurement points (equals more than 150 minutes of continuous measurement at a sample interval of 1 measurement point per second) of two nanosensor samples (pH = 3.98 and 9.82) were recorded.

4.2.6 Real-time monitoring of pH changes during the enzymatic transformation of Penicillin G to 6-aminopenicillanic acid catalysed by *Penicillin G* acylase

Enzymatic transformations were performed in glass vials (1 mL) or inside a microreactor. Calibration standards (40 mM of either acetate, phosphate, CAPS or CHES, IS either 0.30 M) as mentioned above were prepared. The calibration of the nanosensors was performed at different pH values, at ambient air oxygen concentrations and at room temperature. A nanosensor stock dispersion (250 µL, see above) was diluted with a phosphate buffer (200 µL, 50 mM, pH 7.5) containing 50 mM of Penicillin G (PenG) for enzymatic transformations inside glass vials. This mixture was further diluted with a phosphate buffer (500 µL, 20 mM, IS = 0.30 M, pH 8.2) and the pH was adjusted with strong base or acid to 8.3. The final dispersion was stirred and different amounts of *Penicillin G* acylase (PGA) were added. The final volume was 1 mL and the enzyme activities were 3.40, 2.88, 1.98, 1.20 and 0.36 U/mL (expressed as hydrolytic activity of PGA at the conditions referred in SI). The modified optical oxygen meter recorded the phase shifts of the nanosensors at two modulation frequencies (m_1 = 2000 Hz, m_2 = 8000 Hz) every 4 seconds. pH time courses were additionally simulated according to the known kinetic of PGA hydrolysis. The hydrolysis is catalysed by the free enzyme where one mole of phenyl acetic acid is produced per mole of hydrolyzed PenG [27]. The dependency between enzymatic activity and pH exhibit a sigmoidal behavior and an apparent dissociation constant was experimentally determined (pK = 7.4) at the used conditions [28]. The pH change due to the release of protons is described by the Henderson-Hasselbalch equation [28].

  Two nanosensor dispersions were prepared for enzymatic transformations inside a microreactor (channel width: 200, channel depth: 400 µm, volume: 22.7 µL). The first dispersion contained nanosensors (0.75 mL, mixture of oxygen nanosensors and pH nanosensors, see previous paragraph), phosphate buffer with PenG (0.60 mL, see above) and phosphate buffer (1.5 mL, 20 mM, IS = 0.30 M, pH 8.2). The second dispersion contained nanosensors (0.75 mL), water (0.664 mL), phosphate buffer (1.5 ml, 40 mM, IS = 0.30 M, pH 8.2) and *PGA* (81 µL). The enzyme activity was approx. 18 U/mL. Strong acid or base were added to the dispersion until the pH was adjusted to 8.0. The final volume of the dispersions was 3 mL. These two dispersions were introduced over the two main inlets into the microreactor at different flow rates (2.4, 1.2, 0.6, 0.3 and 0.1 µL/s). Measurements were performed with a modified optical oxygen meter equipped with a focusing lens.

4.3 Results and Discussion

4.3.1 Measurement device for dual parameter detection in microfluidic applications

Miniaturized dual-parameter detection tools are scarce for microfluidic applications. Hence, we investigated the use of a commercially available hardware (Piccolo2 with gradient index lens [16]) that was extended with a modified dual lifetime referencing (m-DLR) method [18] for this purpose. Two luminescent indicators with similar absorption and emission spectra but with largely different luminescent lifetimes are necessary for m-DLR measurements. Generally, an indicator that possess a relatively long lifetime in the range µs (phosphorescence of e.g. an oxygen or temperature indicator) and an indicator that possesses a much shorter lifetime in the range of ns (fluorescence of e.g. a pH or CO_2 indicator) are used. Both dyes are excited by a sinusoidally modulated light source and the superimposed overall luminescence emission and phase shift are recorded (Fig. 4.2). The recording is performed at two modulation frequencies (e.g. 2000 and 8000 Hz in the case of PtTPTBPF) in order to obtain the luminescent intensity for each indicator and the luminescent lifetime of the longer living component. The mathematical derivation and further explanations can be found in the supplementary information (SI). The lifetime of the fluorophore which is in the ns range cannot be determined by this set-up. The fastest sampling rate (= time which is needed to measure and record at two different modulation frequencies) is 340 ms. The nanosensors are excited with a red light emitting diode (λ_{max} = 620 nm) and the emission is detected by photodiode, which in combination with a long-pass filter collects the light in the near infrared spectral region (λ > 700 nm). A gradient index lens focuses the excitation light to a point of approximately 80 µm in diameter to enhance signal intensities for microfluidic measurements. The measurement device in combination with our nanosensors (see Fig. 4.2) was used for microreactors with channel dimensions of 200 µm in width and 400 µm in depth.
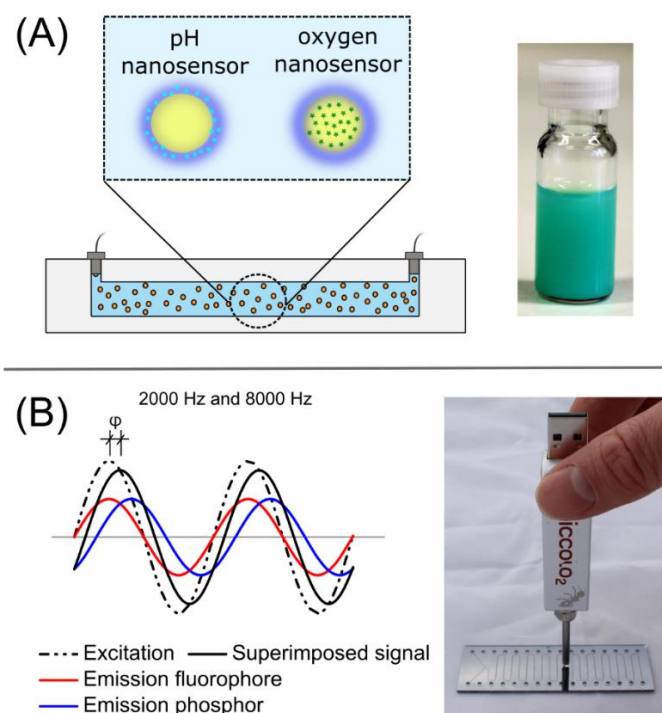
Figure 4.2 Schema of the nanosensors and a nanosensor stock solution (A). m-DLR schema and the measurement device (B). The phase shifts (φ) and the amplitudes of the superimposed signals are used to obtain the luminescent intensity for each indicator and the luminescent lifetime of the phosphor.

4.3.2 Nanosensors for the simultaneous determination of pH and oxygen

Dual sensing of pH and oxygen is challenging from a material point of view because a material for oxygen sensing should be permeable for oxygen but preferably impermeable to ions and protons which are necessary for pH sensing. We chose poly(styrene-block-vinylpyrrolidone) nanoparticles (average diameter = 180 nm) due to their core-shell structure (polystyrene core and hydrophilic polyvinylpyrrolidone shell) and their ability to integrate lipophilic indicator dyes into both domains. Furthermore, these particles can be easily prepared with high reproducibility and feature high stability in aqueous media [29,30]. The nanoparticles are not prone to aggregation even at high particle concentrations (20 mg/mL), high ionic strength or high protein concentrations such as Dulbecco's modified Eagle medium. The size of the particles was investigated by TEM images (see SI Fig. 4.2) and dynamic light scattering experiments (z-av. 180 ± 5 nm in diameter, PDI 0.07 ± 0.02, n = 9). As shown previously [29], lipophilic dyes can either be stained into the shell or the core of the particles by using two different procedures. Tetrahydrofuran/water mixtures can swell the polystyrene core which then enables incorporation of indicator dyes (e.g. oxygen indicator) into the core. Ethanol is used as a solvent in order to mainly entrap the indicator into the shell which is important for pH indicators since only the shell is permeable for protons.

Here, platinum(II) *meso*-tetra(4-fluorophenyl) tetrabenzoporphyrin (PtTPTBPF) was used as an oxygen indicator and a BF_2-chelated tetraarylazadipyrromethene dye (aza-BODIPY) was used as a pH indicator. Both dyes show excellent photostability, absorption in the red region of the electromagnetic spectrum, emission in the near infrared and tuneable dynamic ranges [26,31]. The spectral properties of the dyes are shown in SI Fig. 4.3.

In principle both dyes can be excited with the red LED (λ_{max} approx. 620 nm) of the read-out instrument, but due to the fact that aza-BODIPY dyes show absorption maxima (acidic form) around 675 nm, a light harvesting system [32] with zinc(II) 2,3-bis(3,3,9,9-tetramethyl-2-hydroxyjulolidine)but-2-enedinitrile (Zn-Schiff base, λ_{exc} = 610 nm, λ_{em} = 650 nm) as an antenna dye was used to enhance the brightness. Indeed, the brightness was increased by a factor of 3 compared to nanosensors without the Zn-Schiff base antenna (see SI Fig. 4.4). No leaching was observed because all dyes are lipophilic. PtTPTBPF is stained into the polystyrene core, whereas aza-BODIPY and Zn-Schiff base are physically entrapped into the hydrophilic polyvinylpyrrolidone shell of the particle. Ideally, the three dyes are incorporated together into a single particle. However, preliminary experiments revealed that incorporation of both indicator dyes and the antenna dye into a single PSPVP particle yielded in unreproducible results which may derive from dye migration within the core and shell and interactions of the oxygen indicator with the two other dyes. Therefore oxygen and pH nanoparticles are prepared separately and mixed together at a constant particle ratio to perform m-DLR measurements. In addition, oxygen and pH nanosensors can also be used separately from each other. The oxygen particles for example can be used with phosphorescence lifetime based measurement set-ups. The pH nanosensors can be used with intensity based ratiometric imaging set-ups because the antenna dye emits in the red and the pH indicator emits in the near infrared spectral region.

4.3.3 Characterization of the nanosensors

The dual pH/oxygen nanosensors were developed with regard to stability, reproducibility, accuracy, resolution, response time, cross sensitivity (temperature and ionic strength) and biocompatibility. We optimized the ratio of Zn-Schiff base to aza-BODIPY in order to obtain an efficient light harvesting system (see SI Tab. 4.1-4.3). Further, the ratio of oxygen nanosensors (1.2 mg/mL) to pH nanosensors (5.0 mg/mL) was adjusted to fine-tune the sensitivity of the m-DLR system. The pH/oxygen nanosensor stock solution was conditioned with light prior to the first use in order to obtain a more reliable sensor response. The response of unconditioned nanosensors changed during first exposure with light because of photochemical reactions with the polymeric material. After light conditioning, the nanosensors showed minimal change

in the measurement signal (RSD < 0.5 %, SI Fig. 4.5-4.6) even if more than 9000 measurement points (equals more than 150 minutes of continuous measurement at a sample interval of 1 measurement point per second) were recorded by the measurement device. In addition, cytotoxicity screenings of pH and oxygen nanosensors were performed to rule out any detrimental effect of the nanosensors on cell viability (for experimental details see SI). The metabolic activity of fibroblast cells was not affected even at the highest particle concentrations (1 mg/mL) with respect to the untreated control (see SI Fig. 4.14). Further, a cell viability assay based on Calcein AM and ethidium bromide showed that the intracellular esterase is active and that the plasma membrane of the cells is intact even after incubation overnight (see SI Fig. 4.15).

4.3.3.1 Oxygen measurements

Measurements of the pH/oxygen nanosensors are performed at 2000 and 8000 Hz and the superimposed signal intensities and phase shifts are recorded as described above. The determination of oxygen is straightforward because the luminescence lifetime of the oxygen indicator is directly calculated from dual frequency measurements and corresponded to the oxygen partial pressure (pO_2) of the solution. A pH/oxygen nanosensor dispersion was purged with different oxygen/nitrogen gas mixtures and a Stern-Volmer calibration curve was obtained (f= 0.800±0.015 and K_{SV} = 17.1±0.2 * 10^{-3} hPa^{-1} at 26 °C). A simplified two site model was used to fit the calibration data (Equation 4.1) [33]. The ratio I_0/I in the model was replaced by τ_0/τ where τ is the lifetime of the oxygen indicator dye at a certain pO_2-value. The lifetime τ_0 represents the lifetime under deoxygenated conditions, where the oxygen indicator is in its unquenched state. A simple two point calibration procedure at air saturated and deoxygenated conditions is typically sufficient to achieve good accuracies.

$$\frac{I_0}{I} = \frac{\tau_0}{\tau} = \left(\frac{f}{1 + K_{SV} \cdot pO_2} + (1 - f) \right)^{-1} \quad (4.1)$$

The oxygen resolution of the measurement set-up is 0.5-2.0 hPa at low oxygen concentrations (< 50 hPa) and 4-8 hPa at ambient air oxygen concentrations (approx. 200 hPa at 980 mbar air pressure at room temperature). The nanosensors immediately respond to a change in oxygen concentrations and it is assumed that the response time is < 1s.
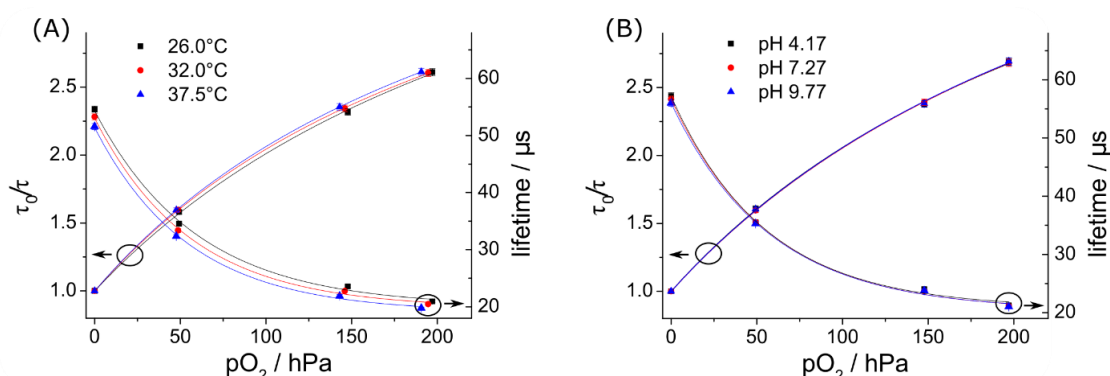
Figure 4.3 Stern-Volmer calibration curves (left Y-axis) and luminescent lifetimes (right Y-axis) for different temperatures at pH 7.27 (A) and for different pH values at 21°C (B). $R^2 > 0.99$ for all shown calibration curves.

The oxygen nanosensors are not influenced by variation of pH but show minor cross-sensitivity to temperature (decrease of τ_o and increase of K_{SV}) as shown in Fig. 4.3.

4.3.3.2 pH measurements

Theoretically, the superimposed phase angle at 2000 Hz or 8000 Hz, the signal intensity of the pH indicator or the ratio of the signal intensities of the pH indicator and of the oxygen indicator can be used for pH determination. The superimposed phase angle at 8000 Hz, however, offers the advantage that the signal is more stable and less prone to error compared to intensity based methods. Furthermore, the superimposed signal at 8000 Hz exhibits a higher pH resolution than the signal at 2000 Hz because of a larger phase angle difference between acidic and basic conditions. Hence, the superimposed signal at 8000 Hz was used for pH measurements. The cotangent of the phase angle at 8000 Hz was plotted against the pH as shown in Fig. 4.4 for different oxygen concentrations. The cotangent ϕ shows linear dependency on the oxygen partial pressure (Fig. 4.4B) if the temperature was kept constant. A Boltzmann sigmoid function was used to fit the pH calibration data (Equation 4.2), where A2 is the bottom value, A1 is the top value, pK_a' (apparent pK_a) is the point of inflection and dx is the slope at the point of inflection.

$$cotan(\varphi) = A2 + \frac{A1 - A2}{1 + e^{(pH - pK_a')/dx}} \quad (4.2)$$

We repeated the pH calibration at different oxygen concentrations with different nanosensor batches multiple times (n = 7) and observed for each sensor batch a similar behaviour. A variation in oxygen concentration changed the values of A1 and A2, whereas, the other 2 calibration parameters (pK_a' and dx) stayed constant. The relative standard deviation (RSD) was < 1% for pK_a' and < 3% for dx. Therefore, a simplified

calibration procedure for the oxygen/pH nanosensors typically consists of a pH calibration at air saturation and the determination of A1 and A2 at two different oxygen concentrations at minimum (e.g. air saturation and anoxic conditions). The pK_a' was 7.23 ± 0.1 and dx was 0.57 ± 0.01 for our system if the temperature was kept constant at 23 °C. It is essential for the simplified calibration model that the temperature is kept constant during the measurement in order to obtain reliable results. Another option to compensate the parameters A1 and A2 for different oxygen concentrations is to plot cotangent ϕ at the two plateau levels (e.g. pH < 4.5 => A1 or pH > 9.5 => A2) against the phase angle of the oxygen indicator (see SI Fig. 4.7). Therefore both parameters are recorded at different oxygen concentrations. This can be done by using an oxygen depletion reaction for example glucose oxidase and glucose or sodium sulphite. The obtained curve can be fitted by an exponential decay function (exponential model) and shows the oxygen dependency of A1 and A2.

In addition, the influence of different ionic strengths and temperatures on the pH nanosensors was investigated. A change in ionic strength from 75 mM to 150 mM resulted in a pH offset of approx. 0.2 pH units (near the pK_a'). The influence of the temperature between 23 °C and 37 °C is even more pronounced and therefore the temperature has to be constant to enable accurate measurements. The influence of the temperature and of the ionic strength on the pH calibration is illustrated in SI Fig. 4.8-4.9.
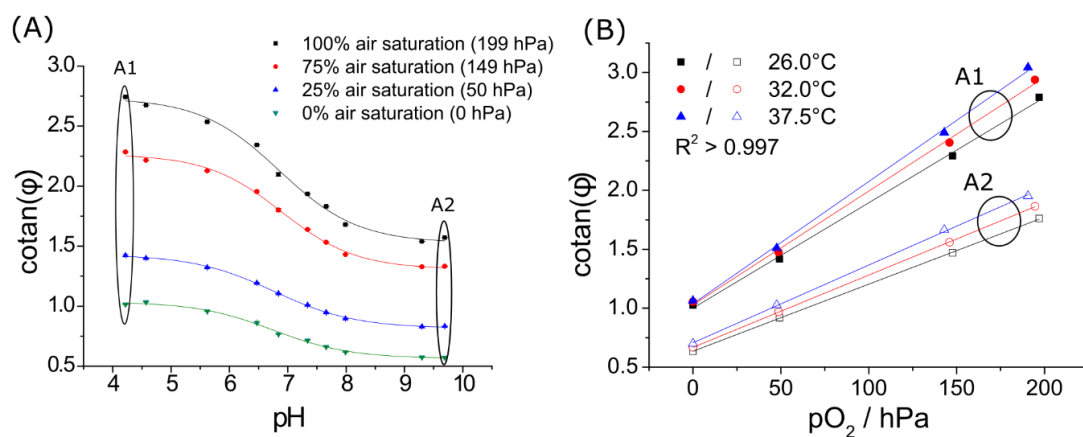
Figure 4.4 pH calibration curves (A) at different oxygen concentrations at 26°C (cotangent of superimposed signal at 8000 Hz, R² > 0.99) and oxygen dependency of the calibration parameters A1 and A2 at different temperatures (B).

The resolution of the pH nanosensors is 0.03-0.1 pH units if the pH is within the dynamic range (apparent pK_a 7.23 ± 1.0) of the nanoparticles. The pH resolution is mostly influenced by the accuracy of the oxygen determination if the linear calibration model

is used. The nanosensors showed the same calibration characteristics even 3 months after preparation (see SI Fig. 4.10).

We evaluated the accuracy of oxygen and pH determination by using different particle solutions at known pH and oxygen concentrations. A1 and A2 were calculated by using the linear model (Fig. 4.4B) and the exponential model. Both models showed similar results (see SI Tab. 4.5). The measured pH values and oxygen concentrations were compared with the set O_2 and pH values and show only minimal deviations (see Tab. 4.1). Further, the oxidation of glucose to D-glucono-δ-lactone and hydrogen peroxide by glucose oxidase was investigated to study the influence of a continuous change in oxygen on the pH measurement. Oxygen is depleted during the reaction which resulted in a pH independent increase of the measurement signals (phase angles). The pH of the solution was monitored by the nanosensors and additionally by a pH electrode. Both techniques showed similar pH values (see SI Fig. 4.11). The pH differences of both methods were lower than 0.1 pH units. The small pH increase of the nanosensors during the beginning of the enzymatic reaction possibly arise from slightly different oxygen concentrations during the 2000 Hz and 8000 Hz measurements.

Furthermore, the system was applied in two different microreactors (see SI Fig. 4.12-4.13). The set-up (100% LED intensity, 1.2 mg/mL pH nanosensors and 0.3 mg/mL oxygen nanosensors) provided sufficient signals (25-60 mV) with signal to noise ratios of 100-500 demonstrating the application in microfluidic devices. However an in-chip calibration procedure is recommended for the achievement of accurate pH and oxygen results.

Table 4.1 Evaluation of the measurement accuracy by comparison of known and measured values after calibration.* calculation of A1 and A2 with the linear model.

sample	pO_2set / hPa	$pO_{2,meas.}$ / hPa	ΔpO_2 / hPa	pH_{Set}	$pH_{meas.}$*	ΔpH
1	39.9	41.3	0.4	6.46	6.52	0.06
2	74.8	76.6	1.8	6.83	6.91	0.08
3	99.7	100.8	1.1	7.35	7.37	0.02
4	124.7	125.2	0.5	7.67	7.70	0.03
5	159.6	159.3	-0.3	7.97	8.02	0.05

4.3.4 Real-time measurements of pH course during the enzymatic transformation of Penicillin G to 6-aminopenicillanic acid catalysed by *Penicillin G acylase*

The enzymatic transformation of Penicillin G (PenG) to 6-aminopenicillanic acid and phenyl acetic acid, which is catalysed by *Penicillin G* acylase (PGA) was used as model

reaction to test our measurement system. Initially, the pH time course was monitored by a pH electrode in the absence or presence of the nanosensors in order to test the potential perturbation on the enzymatic reaction. The reaction was performed in a stirred glass vial and no influence was detected (SI Fig. 4.16). Therefore, the nanosensors (particle concentrations were 1.25 mg/mL for pH and 0.3 mg/mL for oxygen) can be used in the presences of soluble enzyme catalysts. Further, the set-up was used to measure the pH time course at different concentrations of enzyme catalyst. The nanosensors could determine the initial pH irrespectively of the catalyst concentration and the modulation of the pH time course promoted by different hydrolysis velocities of PenG (Fig. 4.5). The dynamic response of the nanosensors is fast enough for real-time monitoring of the characteristic acidification rates at different catalyst concentrations and the measured data fully agree with the expected values corresponding to simulations of PenG hydrolysis shown in Fig. 4.5. The simulations only differed for the two highest enzyme concentrations at the end of the displayed reactions probably because of small deviations in the initial PenG and buffer concentrations. However, the pH endpoints were verified also by measurements with a pH electrode.

The biocatalytic transformation was also performed in a microreactor (Fig. 4.6 and SI Fig. 4.17) at different residence times. The residence time inside the microreactor (from the inlet to the measurement position) changed from 8.3 s, 16.6 s, 33.2 s, 66.4 s, to 199.3 s according to the flow rate (2.4, 1.2, 0.6, 0.3 and 0.1 μL/s). For each residence time the pH at the measurement positions changed. These pH changes were recorded in triplicates (n = 3) and were 7.96 ± 0.03 (8.3 s), 7.89 ± 0.03 (16.6 s), 7.78 ± 0.04 (33.2 s), 7.67 ± 0.03 (66.4 s) and 7.59 ± 0.03 (199.3 s). The oxygen partial pressure stayed constant during the whole measurements (lifetime of the oxygen indicator was constant). The signal intensities (23-28 mV) of the nanosensors were sufficient with signal to noise ratios of 110-600. The peak drops in Fig. 4.6 between the different residence times originate because the pumps stopped and refilled their syringes at these times, while the enzymatic reaction continued.
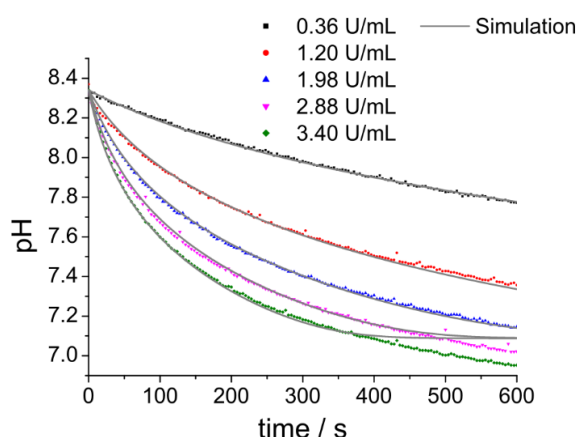
Figure 4.5 pH decrease measured by the nanosensors at different enzyme activities during the transformation of Penicillin G to 6-aminopenicillanic acid and phenyl acetic acid. Measurement data (n = 2) was compared with simulations (grey lines). 20 mM phosphate buffer, 10 mM Penicillin G, 150 mM ionic strength. Reaction was started by adding Penicillin G acylase.
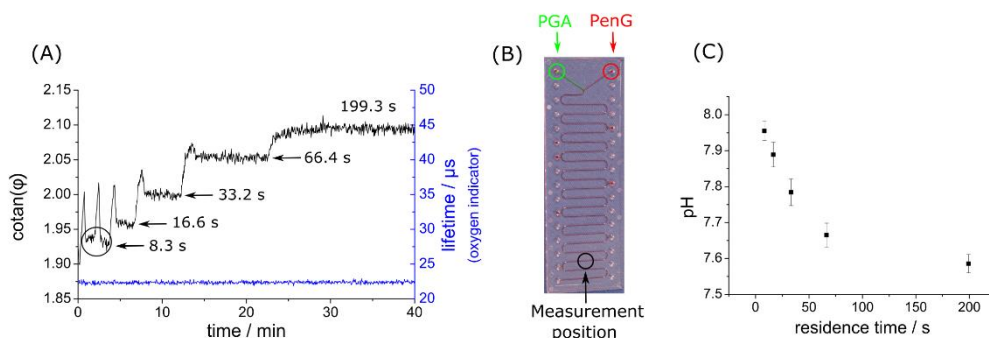
Figure 4.6 Online monitoring during the enzymatic transformation of Penicillin G (PenG) to 6-aminopenicillanic acid and phenyl acetic acid by Penicillin G acylase (PGA) at different residence times (A) in the used microreactor (B). Data was used for the calculation of residence time dependent pH-values (n = 3) (C).

4.3.5 Alternative use of the nanosensors

Independent pH measurements can be also performed with oxygen insensitive PViCl-PAN nanoparticles [34] which were used instead of the described oxygen nanosensors (for preparation protocol see SI). The PViCl-PAN particles were stained with PtTPTBPF and were mixed with pH nanosensors to obtain a dual lifetime referencing (DLR) system. The DLR-system has a higher pH resolution (theoretically approx. 0.01 pH values or below) and shows no cross sensitivity to oxygen because of the very low oxygen permeability of PViCl-PAN. Unfortunately, the particles suffer from several disadvantages. Preliminary experiments showed that PViCl-PAN nanosensors aggregate and precipitate at higher ionic strengths (≥ 150 mM). Aggregation and sedimentation was hindered by continuously stirring the dispersion. The PViCl-PAN nanosensors are also less photostable in comparison to the oxygen nanosensors and should be only used

for short term measurements. Calibration curves of the DLR-system in glass vials and in a microreactor are shown in SI Fig. 4.18.

The pH nanosensors can be also applied in combination with a ratiometric imaging set-up for example a 2-CCD colour near infrared camera. This application is possible because the antenna dye of the light harvesting system emits in the red channel and the pH indicator emits in the near infrared channel of the camera [35]. A calibration curve of the pH nanosensors in a 96-well plate obtained by a 2-CCD colour near infrared camera is shown in the SI Fig. 4.19.

4.4 Conclusion

In summary, we report a powerful measurement set-up consisting of NIR-emitting optical nanosensors and a read-out system based on commercially available oxygen meters that allow simultaneous sensing of pH and oxygen using a modified dual lifetime referencing algorithm. The set-up is applicable in microfluidics and will be used in microfluidic droplet reactors, cell-based assays and lab-on-a-chip applications in the future. The nanosensors show high stability in aqueous media even at high particle concentrations, high ionic strength or high protein concentrations. Additionally they do not show toxicity to cells and are photostable. The nanosensors were used for real-time monitoring of the pH time courses during enzymatic transformations. The measured pH time courses fully agreed with the expected values corresponding to simulations. Oxygen concentrations can be determined at a resolution of 0.5-8.0 hPa (approx. 0.02-0.32 mg/L of dissolved oxygen) depending on the oxygen levels. The pH value can be determined at a resolution of 0.03-0.1 pH units within the dynamic range (apparent pK_a 7.23 ± 1.0) of the nanosensors. The $pK_a{}'$ (7.2±0.1) is in the physiological range which is an interesting region for various applications, e.g. cell based microfluidic assays or organs-on-chips. The system is of particular interest for microfluidic droplet applications because the nanosensors can be easily dispersed into media for monitoring and controlling the conditions within a droplet. In the future, we plan to develop a set of nanosensors with different dynamic ranges based on the aza-BODIPY pH indicator toolbox which was recently published [26].

4.5 References

(1) El-Ali, J.; Sorger, P. K.; Jensen, K. F. *Nature*, **2006**, *442* (7101), 403–411.

(2) Bhatia, S. N.; Ingber, D. E. *Nature biotechnology*, **2014**, *32* (8), 760–772.

(3) Chin, C. D.; Linder, V.; Sia, S. K. *Lab on a chip*, **2007**, *7* (1), 41–57.

(4) Sackmann, E. K.; Fulton, A. L.; Beebe, D. J. *Nature*, **2014**, *507* (7491), 181–189.

(5) Gutmann, B.; Cantillo, D.; Kappe, C. O. *Angewandte Chemie (International ed. in English)*, **2015**, *54* (23), 6688–6728.

(6) Guo, M. T.; Rotem, A.; Heyman, J. A.; Weitz, D. A. *Lab on a chip*, **2012**, *12* (12), 2146–2155.

(7) Bolivar, J. M.; Wiesbauer, J.; Nidetzky, B. *Trends in Biotechnology*, **2011**, *29* (7), 333–342.

(8) Simon A Pfeiffer and Stefan Nagl. *Methods and Applications in Fluorescence*, **2015**, *3* (3), 34003.

(9) Shiwen Sun and Birgit Ungerböck and Torsten Mayr. *Methods and Applications in Fluorescence*, **2015**, *3* (3), 34002.

(10) Grist, S. M.; Chrostowski, L.; Cheung, K. C. *Sensors (Basel)*, **2010**, *10* (10), 9286–9316.

(11) Poehler, E.; Herzog, C.; Lotter, C.; Pfeiffer, S. A.; Aigner, D.; Mayr, T.; Nagl, S. *The Analyst*, **2015**, *140* (22), 7496–7502.

(12) Grist, S. M.; Schmok, J. C.; Liu, M. C.; Chrostowski, L.; Cheung, K. C. *Sensors*, **2015**, *15* (8), 20030–20052.

(13) Rennert, K.; Steinborn, S.; Gröger, M.; Ungerböck, B.; Jank, A.-M.; Ehgartner, J.; Nietzsche, S.; Dinger, J.; Kiehntopf, M.; Funke, H.; Peters, F. T.; Lupp, A.; Gärtner, C.; Mayr, T.; Bauer, M.; Huber, O.; Mosig, A. S. *Biomaterials*, **2015**, *71*, 119–131.

(14) Mahler, L.; Tovar, M.; Weber, T.; Brandes, S.; Rudolph, M. M.; Ehgartner, J.; Mayr, T.; Figge, M. T.; Roth, M.; Zang, E. *RSC Adv*, **2015**, *5* (123), 101871–101878.

(15) Lasave, L. C.; Borisov, S. M.; Ehgartner, J.; Mayr, T. *RSC Adv*, **2015**, *5* (87), 70808–70816.

(16) Ehgartner, J.; Sulzer, P.; Burger, T.; Kasjanow, A.; Bouwes, D.; Krühne, U.; Klimant, I.; Mayr, T. *Sensors and Actuators B: Chemical*, **2016**, *228*, 748–757.

(17) Vasylevska, G. S.; Borisov, S. M.; Krause, C.; Wolfbeis, O. S. *Chem. Mater.*, **2006**, *18* (19), 4609–4616.

(18) Borisov, S. M.; Neurauter, G.; Schroeder, C.; Klimant, I.; Wolfbeis, O. S. *Appl. Spectrosc.*, **2006**, *60* (10), 1167–1173.

(19) Collier, B. B.; McShane, M. J. *Journal of Luminescence*, **2013**, *144*, 180–190.

(20) Demuth, C.; Varonier, J.; Jossen, V.; Eibl, R.; Eibl, D. *Applied microbiology and biotechnology*, **2016**, *100* (9), 3853–3863.

(21) Borisov, S. M.; Seifner, R.; Klimant, I. *Analytical and bioanalytical chemistry*, **2011**, *400* (8), 2463–2474.

(22) Kocincova, A. S.; Nagl, S.; Arain, S.; Krause, C.; Borisov, S. M.; Arnold, M.; Wolfbeis, O. S. *Biotechnology and bioengineering*, **2008**, *100* (3), 430–438.

(23) Borisov, S. M.; Zenkl, G.; Klimant, I. *ACS Appl. Mater. Interfaces*, **2010**, *2* (2), 366–374.

(24) Borisov, S. M.; Saf, R.; Fischer, R.; Klimant, I. *Inorg. Chem.*, **2013**, *52* (3), 1206–1216.

(25) Jokic, T.; Borisov, S. M.; Saf, R.; Nielsen, D. A.; Kühl, M.; Klimant, I. *Anal. Chem.*, **2012**, *84* (15), 6723–6730.

(26) Strobl, M.; Rappitsch, T.; Borisov, S. M.; Mayr, T.; Klimant, I. *Analyst*, **2015**, *140* (21), 7150–7153.

(27) Valencia, P.; Wilson, L.; Aguirre, C.; Illanes, A. *Enzyme and Microbial Technology*, **2010**, *47* (6), 268–276.

(28) Zahel, T.; Boniello, C.; Nidetzky, B. *Process Biochemistry*, **2013**, *48* (4), 593–604.

(29) Borisov, S. M.; Mayr, T.; Klimant, I. *Anal. Chem.*, **2008**, *80* (3), 573–582.

(30) Borisov, S. M.; Herrod, D. L.; Klimant, I. *Sensors and Actuators B: Chemical*, **2009**, *139* (1), 52–58.

(31) Borisov, S. M.; Nuss, G.; Klimant, I. *Anal. Chem.*, **2008**, *80* (24), 9435–9442.

(32) Mayr, T.; Borisov, S. M.; Abel, T.; Enko, B.; Waich, K.; Mistlberger, G.; Klimant, I. *Anal. Chem.*, **2009**, *81* (15), 6541–6545.

(33) Demas, J. N.; DeGraff, B. A.; Xu, W. *Anal. Chem.*, **1995**, *67* (8), 1377–1380.

(34) Borisov, S. M.; Mayr, T.; Mistlberger, G.; Waich, K.; Koren, K.; Chojnacki, P.; Klimant, I. *Talanta*, **2009**, *79* (5), 1322–1330.

(35) Ehgartner, J.; Wiltsche, H.; Borisov, S. M.; Mayr, T. *Analyst*, **2014**, *139* (19), 4924–4933.

4.6 Supplementary Information

4.6.1 Synthesis of zinc(II) 2,3-bis(3,3,9,9-tetramethyl-2-hydroxyjulolidine)but-2-enedinitrile (Zn- Schiff base)

2,3-bis(3,3,9,9-tetramethyl-2-hydroxyjulolidine)but-2-enedinitrile (BTMHJBN, 100 mg, 0.16 mmol) was dissolved in N-methyl-2-pyrrolidone (15 mL) and zinc acetate dihydrate (100 mg, 0.46 mmol) was added to the solution. The reaction mixture was stirred for 2 hours at 60 °C. The solution was poured into a mixture of ice (50 g) and water (100 mL). The product precipitated immediately, was filtered, washed with water (500 mL) and dried at 60 °C in a vacuum oven. Yield: 95 mg (88 %) of a dark violet powder. MS (MALDI-TOF): m/z [M]$^+$ 680.2817 calc., 680.2824 found. ^{1}H NMR (300 MHz, CDCl$_3$), ppm: 8.05 (s, 2H; HC=N), 6.76 (s, 2H; Ph), 3.33 (t, 4H; CH$_2$N), 3.21 (t, 4H; CH$_2$N), 1.71 (m, 8H; CH$_2$), 1.55 (s, 12H; CH$_3$), 1.26 (s, 12H; CH$_3$).^{13}C-APT NMR (75 MHz, CDCl$_3$), ppm: 28.1 (CH$_3$), 30.1(CH$_3$), 31.7, 32.6 , 36.1, 40.2,47.4, 47.7, 112.6, 113.0, 116.8, 117.9, 123.6, 131.0 (CH), 149.6, 156.6 (CH).

4.6.2 Preparation of dual oxygen and pH sensitive PSPVP nanoparticles

PSPVP nanoparticle dispersion (526 mg) was diluted with water (50 mL) and THF (30 mL). The mixture was stirred and THF (20 mL) containing PtTPTBPF (0.2 mg) was added dropwise. THF and water were removed under reduced pressure to a final volume of approx. 45-48 mL. The obtained greenish dispersion was stirred and ethanol (40 mL) was added. Aza-BODIPY (250 µL of a 1 mg/mL stock solution in THF) and a Zn-Schiff base (500 µL of a 1 mg/mL stock solution in THF) were added to 20 mL of ethanol and this mixture was added dropwise to the stirred nanoparticle dispersion. Ethanol and water were removed under reduced pressure to a final volume of approx. 10-20 mL. The particle concentration of the dual oxygen and pH sensitive nanosensor stock dispersion was approx. 10-20 mg/mL.

4.6.3 Preparation of poly(vinylidene chloride-co-acrylonitrile) (PViCl-PAN) reference particles

PViCl-PAN (200 mg) and PtTPTBPF (2 mg) were dissolved in acetone (100 mL). Nanoparticles were precipitated by slowly adding water (300 mL) to the stirred solution. Acetone and water were removed under reduced pressure to a final volume of approx. 40-50 mL; this corresponds to a particle concentration of 4-5 mg/mL.

4.6.4 Measurements

MALDI-TOF mass spectra were recorded on a Micromass TofSpec 2E. The instrument is equipped with a nitrogen laser (337 nm wavelength, operated at a frequency of 5 Hz), and a time lag focusing unit. Spectra were taken in reflectron mode at an accelerating voltage of +20 kV. Dithranol or trans-2-[3-(4-tert-butylphenyl)-2-methyl-2-propenylidene]malononitrile (DCTB) were used as matrix. Analysis of data was done with MassLynx 3.4 (Micromass, Manchester, U.K.).

Transmission electron microscopy (TEM) images, energy filtered images (EFTEM) and electron energy-loss spectroscopy (EELS) data were obtained using a FEI Tecnai F20 instrument fitted with a Schottky Field Emitter, a Gatan imaging filter, and an UltraScan CCD camera. The EELS spectra were acquired in the TEM collection mode of the microscope using a convergence semi-angle of 6.06 mrad, a semi-angle of 11.9 mrad, 200 kV accelerating voltage, and an acquisition time of 100 s.

The activity of soluble and immobilized Penicillin G acylase (PGA) was determined spectrophotometrically by using 6-nitro-3-phenylacetamide benzoic acid (NiPAB) as substrate and additionally by direct quantification of Penicillin G (PenG) hydrolysis. Therefore, the increase in absorbance at 405 nm was measured due to hydrolysis of 0.15 mM NiPAB in a 50 mM sodium phosphate buffer at pH 10 and 25°C. The hydrolytic activity of soluble PGA towards PenG was performed by titration of phenyl acetic acid released upon hydrolysis of 10 mM PenG at pH 9 and 25°C using 25 mM NaOH as titrant solution [1,2]. One activity unit (IUPenG) is the amount of PGA that hydrolyses 1 μmol of PenG per minute.

4.6.5 Biocompatibility of pH and oxygen nanosensors

L929 mouse fibroblast cells were propagated on untreated 75 cm² cell culture flasks (VWR, Austria) using Dulbecco's modified Eagle medium (DMEM) containing a high glucose culture medium with stable glutamine (11965-092, Gibco, Thermo Fisher Scientific) supplemented with 10 % of fetal calve serum (FCS; 10270-106, Gibco, Thermo Fisher Scientific), and 1X penicillin/streptomycin solution (10378016, Gibco, Thermo Fisher Scientific). Cells were maintained in a humidified atmosphere at 37°C and at a 5 % CO_2 atmosphere.

Cytotoxicity cell viability of pH and oxygen nanoparticles was assessed in a 96-well plate format using an Alamar Blue (Life Technologies, Austria) viability assay. Cells were seeded at a density of $1*10^5$ cells cm^{-2} and cultured for 24 hours. Afterwards, cells were exposed with nanoparticle-containing medium (200 μL, particle concentrations were 1.0, 0.5, 0.25, 0.125, 0.063 mg/mL, n = 3) or pure medium (blank) and cultured for a period of 60 min or 12 hours. Afterwards, the nanoparticle-containing medium was removed and

the cells were rinsed with culture medium. Alamar Blue 10X stock solution was diluted 1+9 with culture medium and was added (100 µL) to each microwell and incubated for 4 h at 37 °C. The absorption was recorded at 570 nm using an Enspire 2300 plate reader (PerkinElmer, Austria).

For assessment of the cell viability a LIVE/DEAD® Viability/Cytotoxicity Assay Kit (Life Technologies, Austria) was used. The staining solution was prepared according the manufacturer's instructions. Microwells used in the cytotoxicity experiment were rinsed with culture medium and cell cultures were incubated with 100 µL of a Calcein AM/ethidium bromide containing medium for 30 min at 37°C. Fluorescence was assessed on a Wilovert 30 fluorescence microscope (Wetzlar Hund) equipped with TRITC and GFP filter cubes and XC10 firewire camera (Olympus).

4.6.5 Mathematical derivation of the modified dual lifetime referencing (m-DLR) method

Luminophores behave like first order linear time-invariant systems under the assumptions that moderate excitation light intensities are used [3]. Therefore, the emission signal $S(t)$ of a luminophore, which is described by a mono-exponential decay, is Fourier transformed to the expression seen in equation (1).

$$S(t) = S_0 * e^{-t/\tau} \xrightarrow{\mathcal{F}} S(i\omega) = \frac{S_0^*}{1 + i\omega\tau} \quad (1) \; with \; \omega = 2 * \pi * f$$

As described in the main article, two luminescent indicators with largely different luminescent lifetimes, for example a phosphor and a fluorophore, are necessary in order to perform the m-DLR method [4], which means that the superimposed signal of both luminophores has to be measured at 2 modulation frequencies ($f_1 \, and \, f_2$). Equation (2-3) show the Fourier transformed signals for the oxygen indicator $P(i\omega)$ (phosphor, eq. 2) and for the pH indicator $F(i\omega)$ (fluorophore, eq. 3) . The lifetime of the oxygen indicator (τ) corresponds to the oxygen partial pressure (pO_2) whereas the lifetime of the pH indicator is three orders of magnitudes lower (in the range of ns) and hence the measurement signal $F(i\omega)$ only corresponds to the fluorescence intensity of the pH indicator, which is pH dependent.

$$P(i\omega) = \frac{P_0^*}{1 + i\omega\tau(pO_2)} \quad (2)$$

$$F(i\omega) = \frac{F_0^*(pH)}{1 + i\omega\tau} \xRightarrow{\omega\tau \ll 1} F(i\omega) = F_0^*(pH) \quad (3)$$

The superimposed signal $S(i\omega)$ is described by a composed vector of the fluorophore $F(i\omega)$ and of the phosphor $P(i\omega)$ in the complex space as shown in the figure below $(S(i\omega) = F(i\omega) + P(i\omega))$.
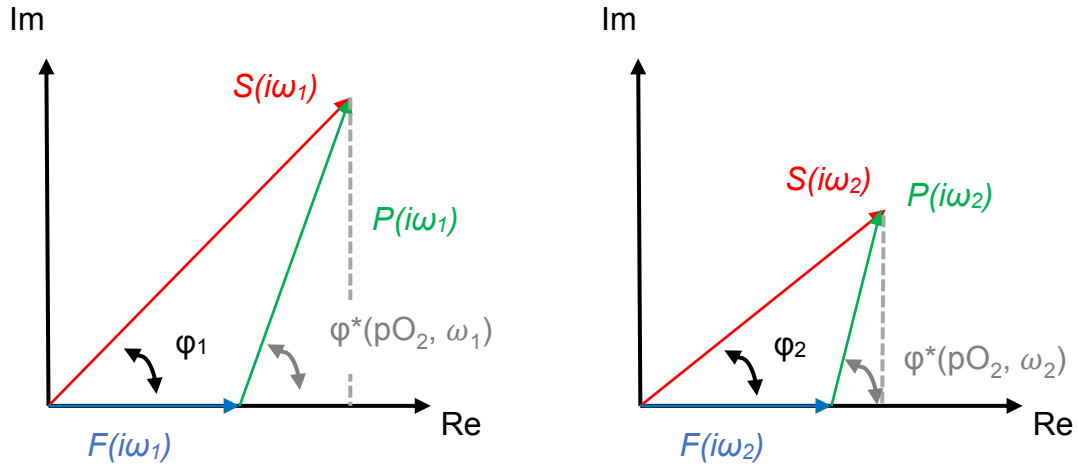
SI Figure 4.1 Vector representation of the superimposed signal S(iω) in the complex space at the two modulation frequencies ω₁ and ω₂.

The measured signal intensities (amplitude) at the two frequencies (ω1 and ω2) correspond to the length $|\vec{S}|$ of the vectors S(iω1) and S(iω2). Further, the measured phase difference at each frequency corresponds to the phase angle (φ₁ and φ₂) shown above. In the following equations (4-5) the relationship between the vectors are shown.

$$Im\left\{S(i\omega)\right\} = Im\left\{P(i\omega)\right\} = Im\left\{\frac{S_0^*}{1+i\omega\tau}\cdot\frac{1-i\omega\tau}{1-i\omega\tau}\right\}$$

$$Im\left\{S(i\omega)\right\} = Im\left\{P(i\omega)\right\} = -\tau\omega\cdot\frac{S_0^*}{1+\omega^2\tau^2} \quad (4)$$

$$Re\{P(i\omega)\} = Re\left\{\frac{S_0^*}{1+i\omega\tau}\cdot\frac{1-i\omega\tau}{1-i\omega\tau}\right\}$$

$$Re\left\{P(i\omega)\right\} = \frac{S_0^*}{1+\omega^2\tau^2} = \frac{Im\left\{S(i\omega)\right\}}{-\tau\omega} \quad (5)$$

$$Re\left\{S(i\omega)\right\} = |\vec{S}|*\cos\varphi \quad (6)$$

Under the assumption shown in equation (7) the phase angle of the oxygen indicator φ*(pO₂,ω) and the signal intensities of the oxygen and pH indicator are calculated as shown below.

$$F(i\omega_1) = F(i\omega_2) = F_0^*(pH) \quad (7)$$

It is important for the following assumptions that pH and oxygen stay almost constant during the two measurements at the two adjusted frequencies. Further, it is necessary that the read-out hardware shows frequency independent signal intensities. Therefore, the signal intensities for different frequencies have to be corrected. If these assumptions are considered the following derivation is valid:

$$Re\left\{S(i\omega_1)\right\} - Re\left\{S(i\omega_2)\right\} = F(i\omega_1) + Re\left\{P(i\omega_1)\right\} - (F(i\omega_2) + Re\left\{P(i\omega_2)\right\}) =$$

$$Re\left\{S(i\omega_1)\right\} - Re\left\{S(i\omega_2)\right\} = Re\left\{P(i\omega_1)\right\} - Re\left\{P(i\omega_2)\right\} =$$

$$= \left|\vec{S}_1\right| * \cos\varphi_1 - \left|\vec{S}_2\right| * \cos\varphi_2 = \frac{Im\left\{S(i\omega_1)\right\}}{-\tau\omega_1} - \frac{Im\left\{S(i\omega_2)\right\}}{-\tau\omega_2}$$

$$\left|\vec{S}_1\right| * \cos\varphi_1 - \left|\vec{S}_2\right| * \cos\varphi_2 = \frac{\left|\vec{S}_1\right| * \sin\varphi_1}{-\tau\omega_1} - \frac{\left|\vec{S}_2\right| * \sin\varphi_2}{-\tau\omega_2}$$

$$= \frac{1}{-\tau} * \left(\frac{\left|\vec{S}_1\right| * \sin\varphi_1}{\omega_1} - \frac{\left|\vec{S}_2\right| * \sin\varphi_2}{\omega_2}\right)$$

$$-\tau = \frac{\left|\vec{S}_1\right| * \sin\varphi_1 * \omega_2 - \left|\vec{S}_2\right| * \sin\varphi_2 * \omega_1}{\omega_1 * \omega_2 * (\left|\vec{S}_1\right| * \cos\varphi_1 - \left|\vec{S}_2\right| * \cos\varphi_2)} \quad (8)$$

$$Re\left\{P(i\omega_1)\right\} = \frac{Im\left\{S(i\omega_1)\right\}}{-\tau\omega_1}$$

$$Re\left\{P(i\omega_1)\right\} = \frac{\left|\vec{S}_1\right| * \sin\varphi_1 * \omega_2 * (\left|\vec{S}_1\right| * \cos\varphi_1 - \left|\vec{S}_2\right| * \cos\varphi_2)}{(\left|\vec{S}_1\right| * \sin\varphi_1 * \omega_2 - \left|\vec{S}_2\right| * \sin\varphi_2 * \omega_1)} \quad (9)$$

The phase angle $\varphi^*(pO_2,\omega)$ of the oxygen indicator, the luminescent lifetime (τ) of the oxygen indicator and the signal intensities of the oxygen as well as pH indicator are calculated with these equations as seen below.

$$\varphi^*(pO_2, \omega_1) = \tan^{-1}\left(\frac{\left|\vec{S}_1\right| * \sin\varphi_1}{Re\left\{P(i\omega_1)\right\}}\right) \quad (10)$$

$$\tau(pO_2) = \frac{\tan\varphi^*(pO_2, \omega_1)}{\omega_1} \quad (11)$$

$$Intensity(pO_2) = \sqrt{\left(\left|\vec{S}_1\right| * \sin\varphi_1\right)^2 + (Re\left\{P(i\omega_1)\right\})^2} \quad (12)$$

$$Intensity(pH) = \left|\vec{S}_1\right| * \cos\varphi_1 - Re\left\{P(i\omega_1)\right\} \quad (13)$$

4.6.6 Nanosensor characterisation using TEM and DLS

The size of the nanosensors was obtained by dynamic light scattering (z-av. 180 ± 5 nm in diameter, PDI 0.07 ± 0.02, n = 9) and TEM imaging. Dynamic light scattering experiments showed that the majority of the particles (approx. 93 %) had a size between 122 nm and 295 nm in diameter. The size of the nanosensors in the TEM images is in the range of 50-100 nm, which is smaller than the values obtained by dynamic light scattering experiments (z-av. 180 nm). However, this discrepancy could be due to the shrinkage or collapse of the hydrogel shell of the particles in the anhydrous environment of the evacuated electron microscope sample chamber. The diffuse layer around the particles in Fig. 2 (right TEM image, see edges) could possibly be a hydrogel layer which covers the polystyrene cores. This observation in combination with the fact that the particles consist of 64% w/w of styrene and 36% w/w of vinylpyrrolidone could explain why the particles are much smaller in the TEM images.
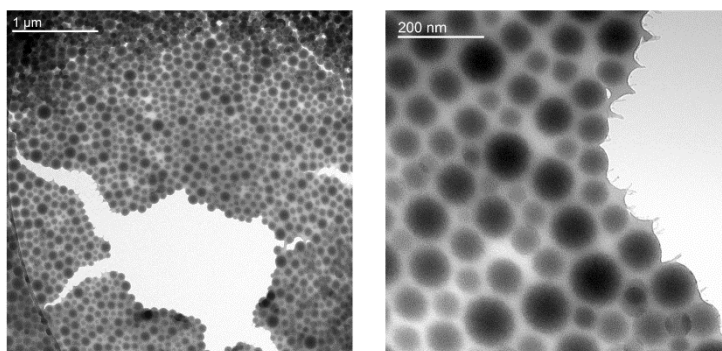
SI Figure 4.2 TEM images of the pH nanosensors.

4.6.7 Spectral properties of the dyes
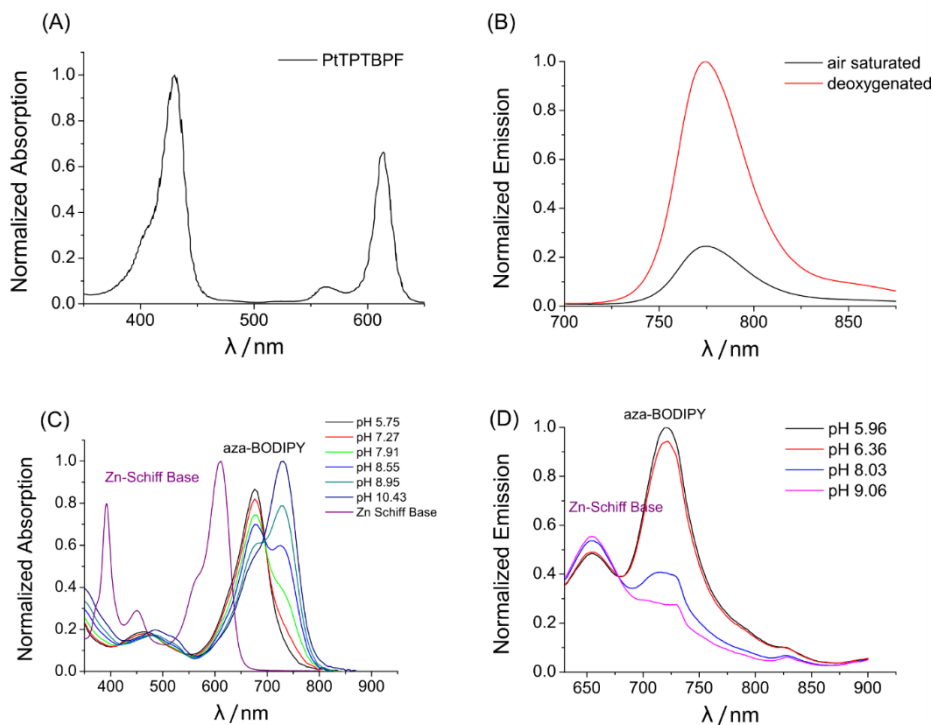
SI Figure 4.3 Absorption spectrum of PtTPTBPF in toluene (A). Emission spectra (λ_{exc} = 620 nm) of PSPVP nanosensors stained with PtTPTBPF at air saturated or deoxygenated conditions in water (B). Absorption spectrum of Zn-Schiff base in THF and absorption spectra of aza-BODIPY in ethanol/buffer mixtures at different pH values (C). Emission spectra (λ_{exc} = 620 nm) of PSPVP nanosensors stained with Zn-Schiff base and aza-BODIPY at different pH values in water (D).

4.6.8 Signal enhancement of the nanosensors by light harvesting

The use of a light harvesting system increases the signal intensity more than 3 times compared to particles without the antenna dye. The signal increase derives not only from energy transfer alone but also from fluorescence of the Zn-Schiff base because not all of the energy is transferred from Zn-Schiff base to aza-BODIPY (see SI Fig. 4.4). The Zn-Schiff base fluorescence is also detected by the read-out device and thus influences the pH sensitivity of the system.
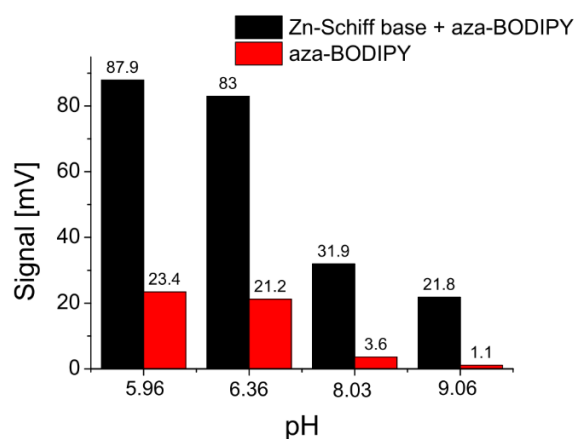
SI Figure 4.4 Comparison between pH nanosensors with and without antenna dye (Zn-Schiff base). The nanosensors were stained with 0.125 % w/w of aza-BODIPY and in addition with 0.25 % Zn-Schiff base for the light harvesting system. The particles were suspended in buffers with a particle concentration of 0.1 % w/w.

4.6.9 Optimization of the light harvesting system

In order to obtain an efficient light harvesting system, the ratio of Zn-Schiff base to aza-BODIPY is optimized by considering following effects: If low amount of Zn-Schiff base is added, less energy is transferred to the aza-BODIPY which results in low signal intensity. Whereas too high amounts of the antenna dye decrease the pH sensitivity of the aza-BODIPY dye due to increased background signals. Moreover, very high concentration of Zn-Schiff base (and also aza-BODIPY) in the particle system may cause inner filter effects [5,6] and self-quenching processes [6] which again result in decreased signal intensities. Different ratios of aza-BODIPY to Zn-Schiff base are shown below.

SI Table 4.1 Amount of stained dye per 100 mg of PSPVP particles.

	Ratio 1	Ratio 2	Ratio 3	Ratio 4
aza-BODIPY C12 / µg	125	62.5	42	42
Zn-Schiff base / µg	250	250	250	83

SI Table 4.2 Signal intensities (mV) of different ratios of Zn-Schiff base and aza-BODIPY dye in PSPVP particles with a concentration of approx. 0.5 mg/mL) Measurement settings: 60 % LED intensity at 2000 Hz, signal intensities for 2000 and 8000 Hz are equal. Measurement time for each point was set to 16 ms.

pH	Ratio 1 [mV]	Ratio 2 [mV]	Ratio 3 [mV]	Ratio 4 [mV]
3.94	45.3	86.4	90.9	71.4
7.10	25.0	56.9	64.9	48.4
9.83	7.7	22.0	30.2	21.6

SI Table 4.3 Signal intensity ratios calculated from the data of SI Tab. 4.2.

pH	Ratio 1	Ratio 2	Ratio 3	Ratio 4
3.94	5.88	3.93	3.01	3.31
7.10	3.25	2.59	2.15	2.24
9.83	1.00	1.00	1.00	1.00

Ratio 1 has the highest dynamic range, therefore ratio 1 was chosen for the light harvesting system because the obtained light intensities were sufficient for our purpose but the ratio of the light harvesting system can be further optimized if necessary.

4.6.10 Photostability experiments of the nanosensors

Oxygen/pH nanosensors which were conditioned for 10 min prior to the first use showed minimal drift under measurement conditions even if more than 9000 measurement points were recorded.
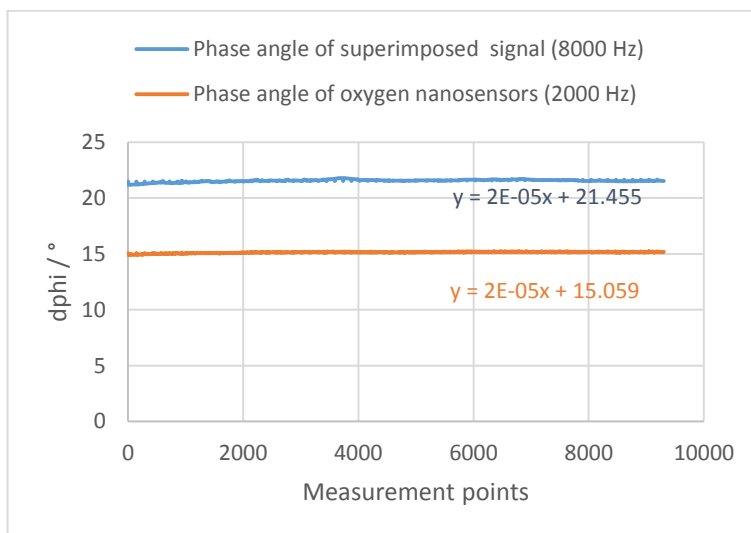
SI Figure 4.5 Long term measurements of oxygen/pH nanosensors at pH 4.0, 100% LED intensity and 16 ms measurement duration per frequency.
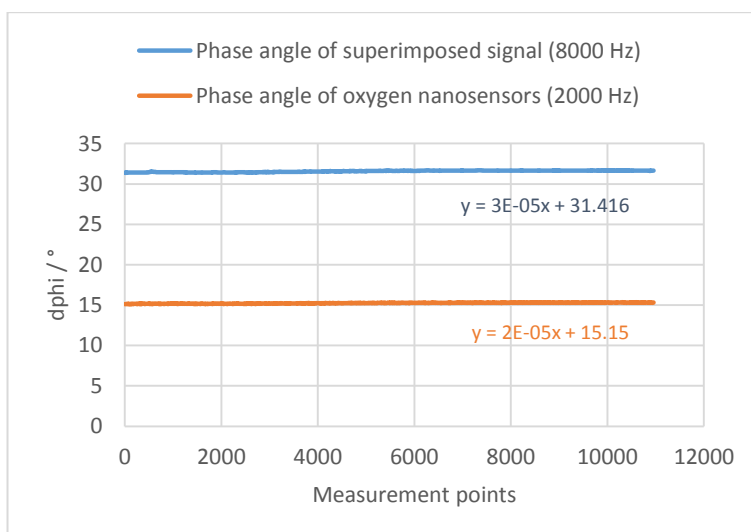
SI Figure 4.6 Long term measurements of oxygen/pH nanosensors at pH 9.8, 100% LED intensity and 16 ms measurement duration per frequency.

SI Table 4.4 Summary of the long term measurements.

pH	dphi oxygen nanosensors [2000 Hz]	dphi [8000 Hz]
4.0	15.14 ± 0.06	21.55 ± 0.11
9.8	15.25 ± 0.06	31.57 ± 0.10

4.6.11 Correlation between A1 / A2 and the phase angle of the oxygen indicator

The calibration parameters A1 (top value of Boltzmann sigmoid function) and A2 (bottom value of Boltzmann sigmoid function) were plotted against the phase angle of the oxygen indicator and follows an exponential decay. The calibration curve in Fig. 4.7A was obtained by recording A1 and A2 at four different oxygen concentrations (199 hPa, 149 hPa, 50 hPa, 0 hPa) and at three different temperatures (26°C, 32°C and 37.5°C). The calibration curve in Fig. 4.7B was obtained by recording A1 and A2 during oxygen depletion reactions at the two plateau levels (e.g. pH < 4.5 => A1 reaction with glucose and glucose oxidase; or pH > 9.5 => A2 reaction with sodium sulphite).
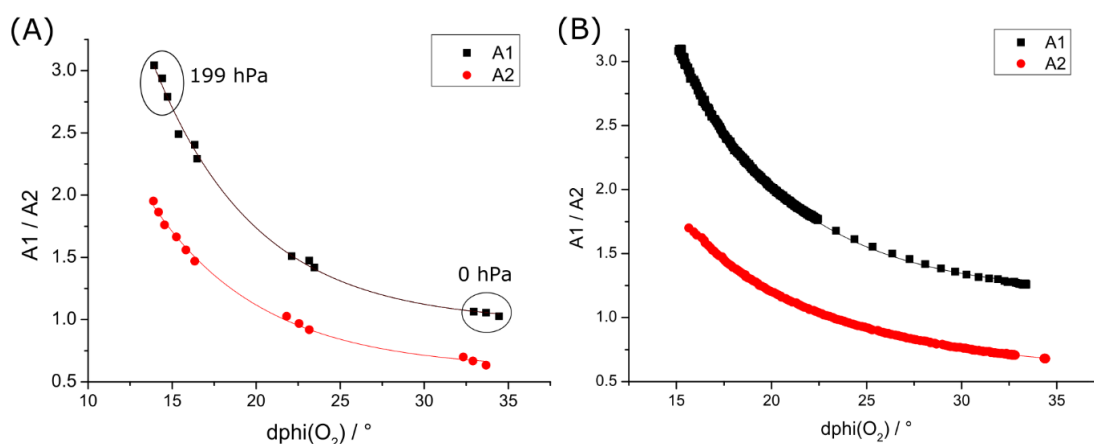
SI Figure 4.7 Oxygen dependency of the calibration parameters A1 and A2 at four different oxygen concentrations (199 hPa, 149 hPa, 50 hPa, 0 hPa) and at three different temperatures (26°C, 32°C and 37.5°C) (A) and by oxygen depletion reactions at the two plateau levels (e.g. pH < 4.5 => A1 or pH > 9.5 => A2) (B).

4.6.12 Comparison between the linear calibration model and the exponential model

Samples with different pH values and oxygen concentrations (as seen in the main article) were prepared and measured. The obtained data was used to calculate the values for oxygen and pH. The linear and the exponential calibration models for A1 and A2 were used and the obtained values agree as can be seen below. The linear model offers the advantage that a simple calibration procedure at two pH values (e.g. pH < 4.5 => A1 or pH > 9.5 => A2 reaction) and at two oxygen concentrations (e.g. air saturation and anoxic conditions) allows the determination of A1 and A2 if the temperature is kept constant. A disadvantage of the linear model is the fact that the pH determination relies on the accurate determination of the oxygen partial pressure in contrast to the exponential model where only the phase angle of the oxygen indicator is needed to determine A1 and A2. However, the exponential model needs more calibration points in order to obtain a reliable calibration function. In general, usage of the linear model is only recommended if temperature control and temperature maintenance is ensured during the calibration and use of the nanosensors.

SI Table 4.5 Comparison between the real and calculated pH values by using the linear or the exponential calibration model.

sample	pHSet	pHmeas., linear	ΔpH	pHmeas.,expo.	ΔpH
1	6.46	6.52	0.06	6.37	-0.09
2	6.83	6.91	0.08	6.88	0.05
3	7.35	7.37	0.02	7.39	0.04
4	7.67	7.70	0.03	7.75	0.08
5	7.97	8.02	0.05	8.03	0.06

4.6.13 Cross sensitivity of the oxygen/pH nanosensor to temperature and ionic strength

The pH/oxygen nanosensors were calibrated at different temperatures and ionic strengths to determine the cross sensitivity, which is shown in the figures below. The calibration of the nanosensors has to reflect the actual conditions during the measurements in order to provide accurate oxygen and pH values.
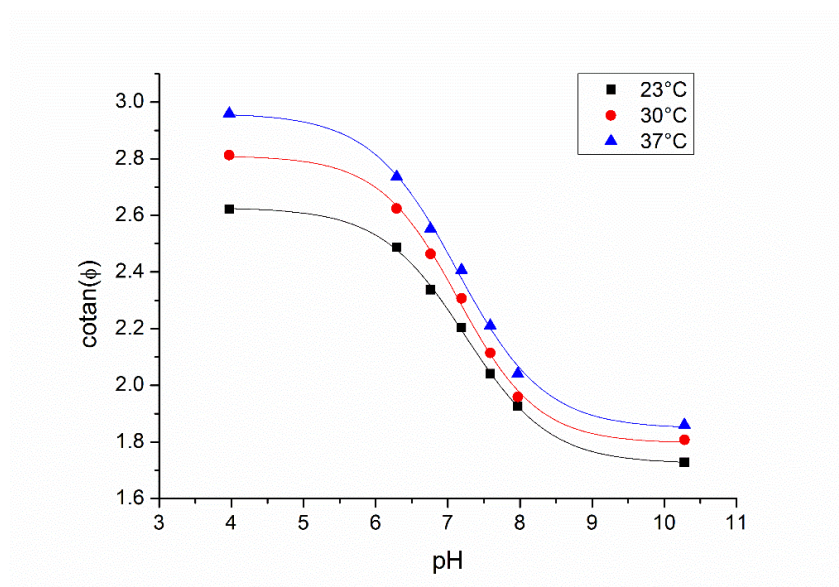
SI Figure 4.8 Influence of temperature on the superimposed signal at 8000 Hz at an ionic strength of 150 mM.
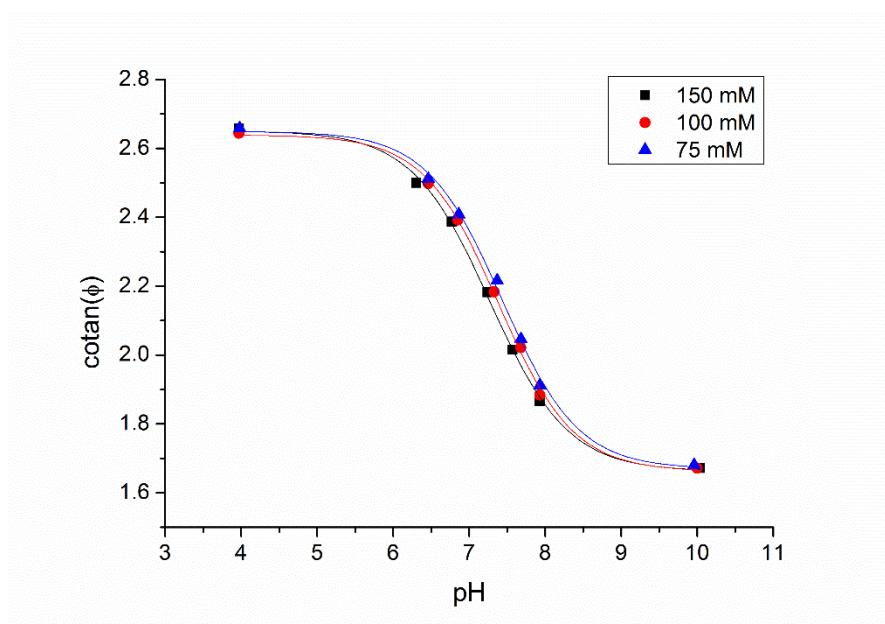
SI Figure 4.9 Dependency of ionic strength on the superimposed signal at 8000 Hz at 23°C.

4.6.14 Long-term stability test of the nanosensors after storage

The calibration curves of the nanosensor did not change even after 3 months of storage. The changes below result from small changes in temperature and minor pipetting errors during preparation of the pH and oxygen nanosensor stock solutions.
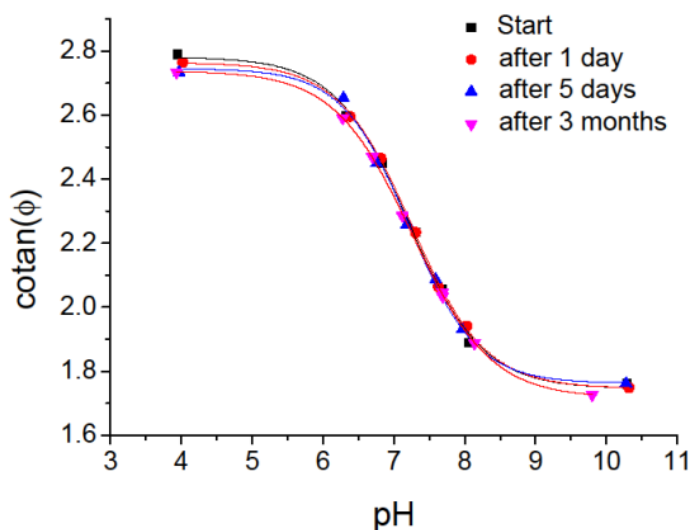
SI Figure 4.10 Measurements (8000 Hz) of the pH/oxygen nanosensors after different times of storage.

4.6.15 Influence of the oxygen concentration on the pH measurement
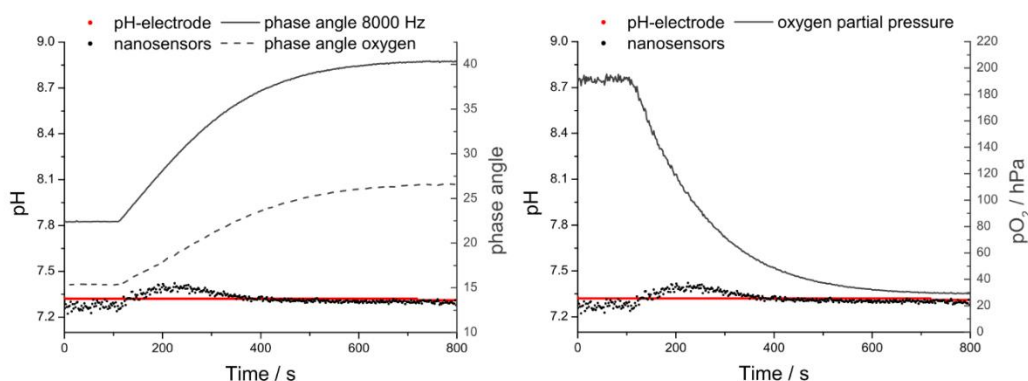
SI Figure 4.11 pH monitoring during the oxidation of glucose to D-glucono-δ-lactone and hydrogen peroxide by glucose oxidase (n=2). The pH value was determined by a pH electrode and the nanosensors every 2 seconds. The pH of the nanosensors was obtained by using the exponential model.

4.6.16 Measurement of the nanosensors within microreactors

Calibration curves of the nanosensor in different microreactors are shown below.
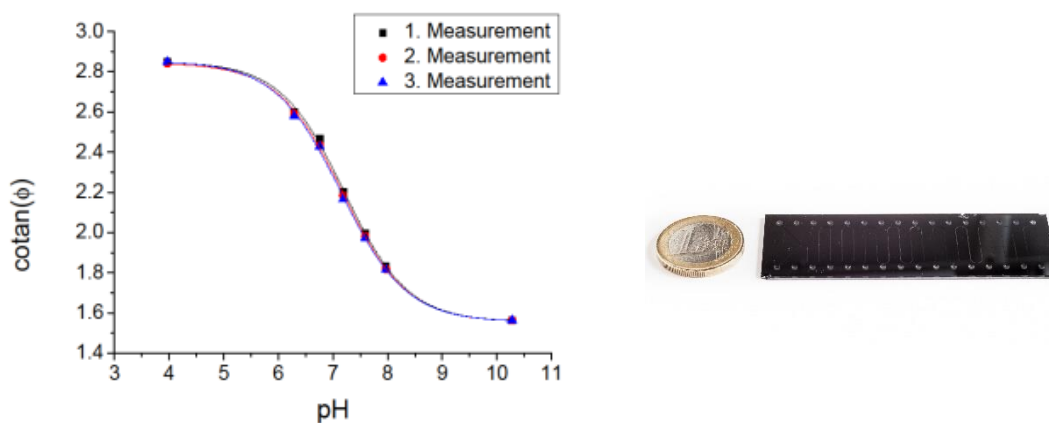
SI Figure 4.12 Measurements (8000 Hz) of the nanosensors within a silicon/glass microreactor from iX-factory with a channel width of 200 μm and a channel depth of 400 μm.
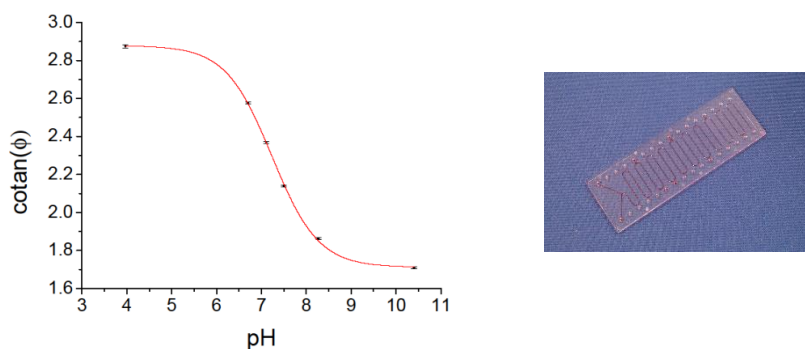
SI Figure 4.13 Measurement (8000 Hz) of the nanosensors within a polymeric microreactor from microfluidic ChipShop with a channel width of 200 μm and a channel depth of 400 μm.

4.6.17 Biocompatibility of pH and oxygen nanosensors

The cell metabolic activity determined by the Alamar Blue viability assay was not affected by the nanosensors which is shown in the figure below.
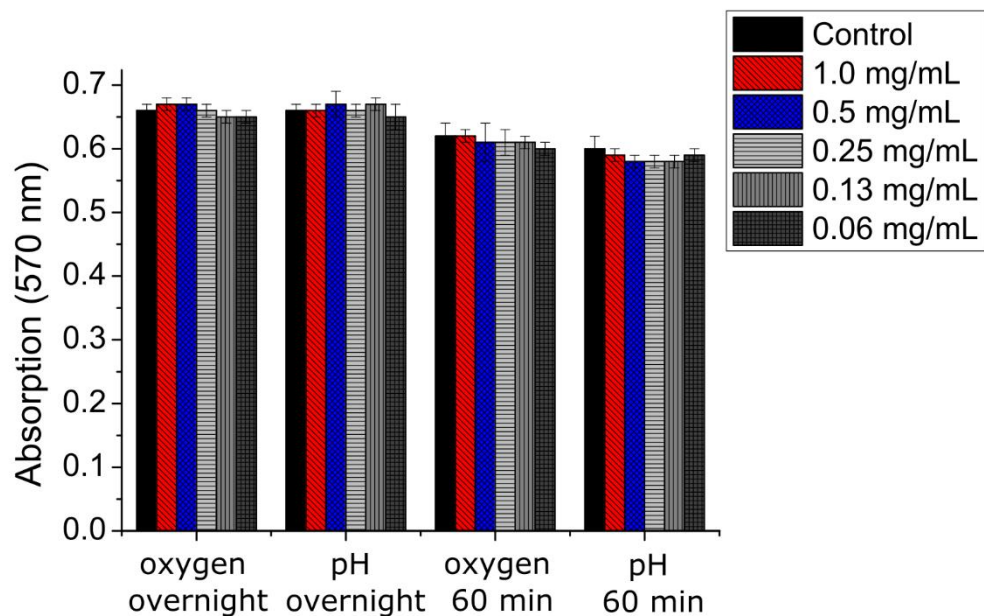
SI Figure 4.14 Metabolic activity of fibroblast cells after 60 min and overnight incubation with oxygen and pH nanoparticles at different particle concentrations (n = 3).

The cell viability assay (LIVE/DEAD® Viability/Cytotoxicity Assay) showed that the intracellular esterase is active (green cells) and that the plasma membrane of the cells is intact (absence of stained nuclei; see Fig. 4.15). These experiments indicate that the nanosensors are biocompatible but for specific applications with different cell types further investigations will be necessary.
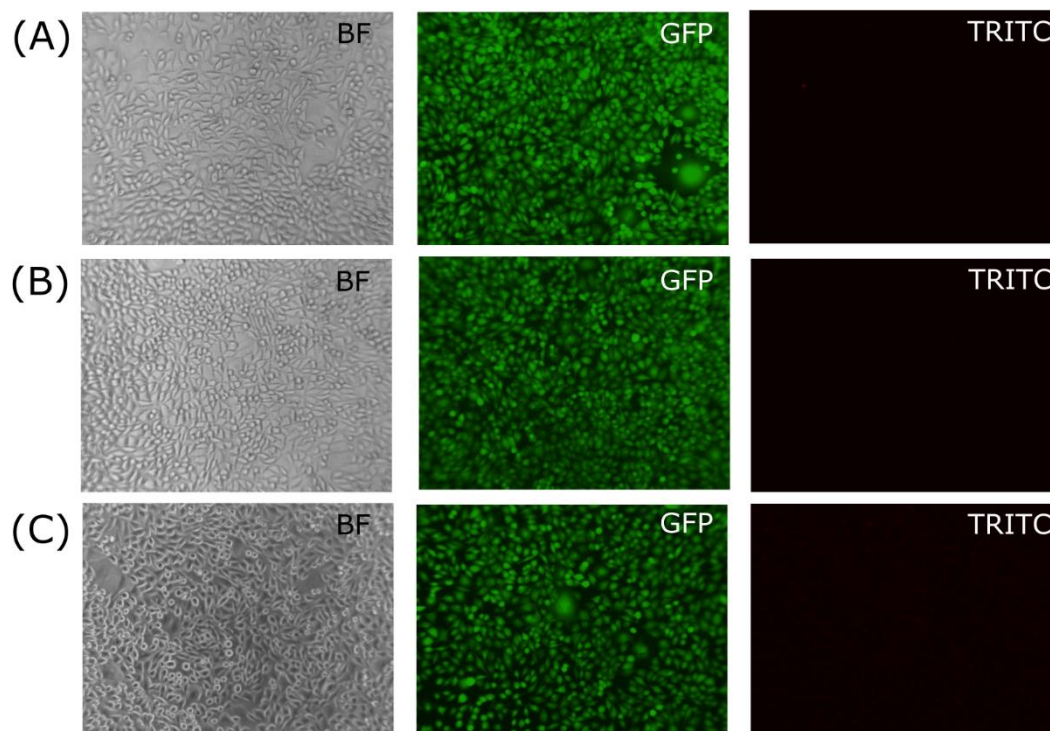
SI Figure 4.15 Cell viability of fibroblast cells incubated overnight with medium (A), oxygen nanosensors (B) and pH nanosensors (C) at a nanosensor concentration of 1 mg/mL. Live cells are fluorescing green in the GFP channel (Calcein AM) whereas dead cells have red fluorescing nuclei in the TRITC channel (ethidium bromide).

4.6.18 Real-time monitoring of pH changes during the enzymatic transformation of Penicillin G to 6-aminopenicillanic acid catalysed by *Penicillin G* acylase
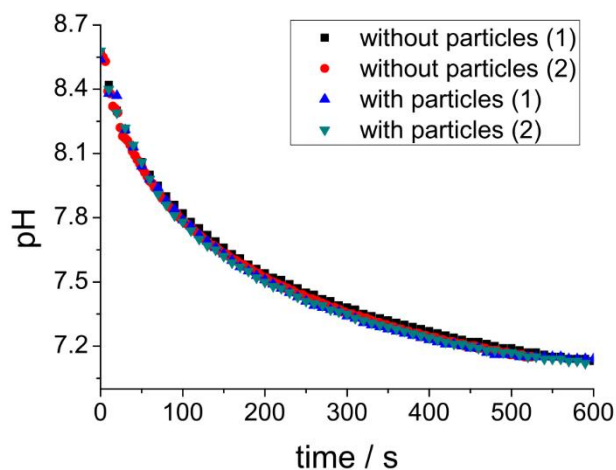
SI Figure 4.16 Comparison of the pH change of the enzymatic transformation measured by a pH electrode in the absence or presence of the nanosensors (1.2 mg/mL pH particles and 0.3 mg/mL oxygen particles). 20 mM phosphate buffer, 10 mM Penicillin G, 150 mM ionic strength. Reaction was started by adding *Penicillin G* acylase (enzyme activity 3.8 U/mL).
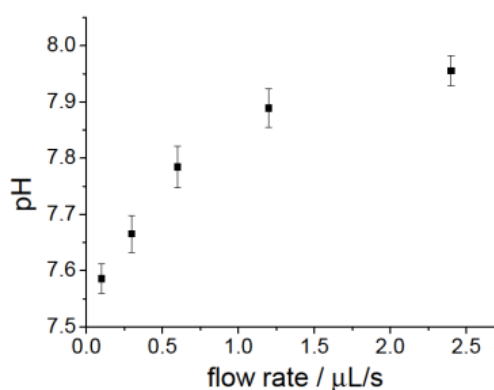
SI Figure 4.17 Comparison of the pH of the enzymatic reaction within a microreactor at different flow rates (2.4, 1.2, 0.6, 0.3 and 0.1 µL/s; n= 3). 20 mM phosphate buffer, 5 mM Penicillin G, 150 mM ionic strength. Reaction was started by adding *Penicillin G* acylase.

4.6.19 Alternative use of the nanosensors
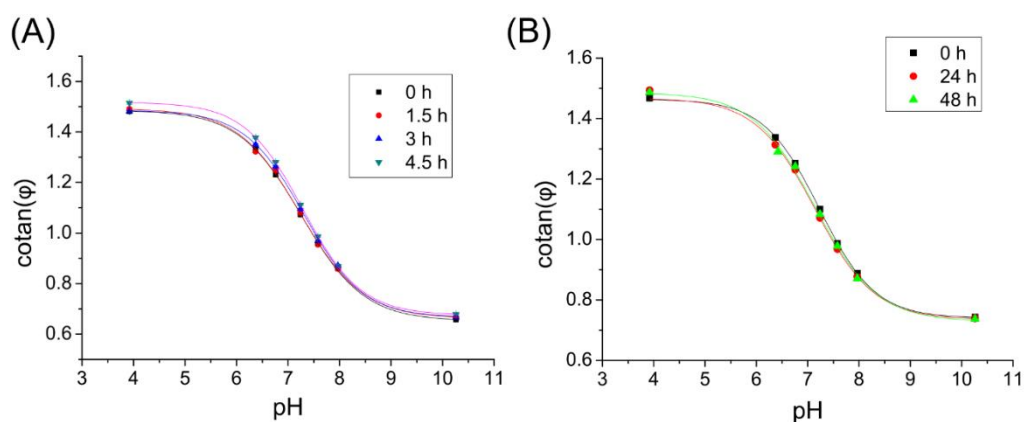
SI Figure 4.18 Calibration of nanosensors based on oxygen impermeable PViCl-PAN nanoparticles (0.18 mg/mL) stained with PtTPTBPF and mixed with the pH nanosensors (1.2 mg/mL). Measurements were either performed in a microreactor ((A), microreactor see SI Fig. 4.7) or in a glass vial (B). 20 mM phosphate buffer, 150 mM ionic strength at 23°C.

Modell	Boltzmann	
Gleichung	y = A2 + (A1-A2)/(1 + exp((x-x0)/dx))	
Chi-Quadr Reduziert	4.8131E-4	
Kor. R-Quad	0.99434	
		Wert	Standardfeh
	A1	1.221	0.02297
R0/R	A2	0.453	0.02312
	x0	6.985	0.07147
	dx	0.578	0.0702
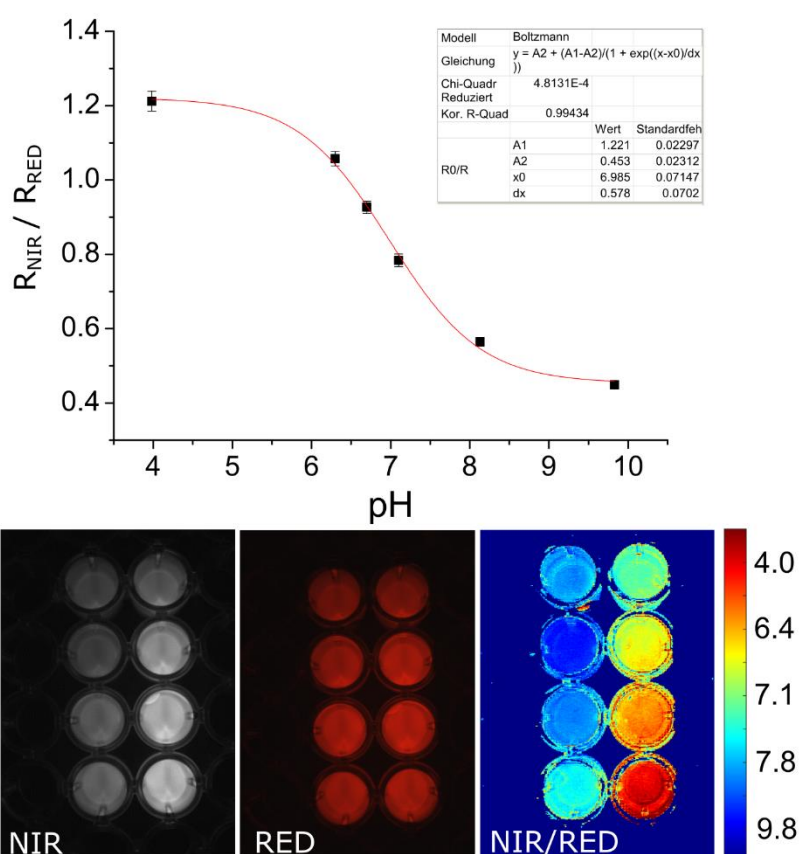
SI Figure 4.19 Imaging of the pH nanosensors in a 96-well plate with a 2-CCD colour near infrared camera at different pH values. 20 mM phosphate buffer, 150 mM ionic strength at 23°C.

4.6.20 References

(1) Valencia, P.; Wilson, L.; Aguirre, C.; Illanes, A. *Enzyme and Microbial Technology*, **2010**, *47* (6), 268–276.

(2) JM, G.; Alvaro, G.; CM, R.; Fernandez-Lafuente, R. *Biotechnology and Applied Biochemistry*, **1994**, *20* (3), 357–369.

(3) Larndorfer, C.; Borisov, S. M.; Lehner, P.; Klimant, I. *Analyst*, **2014**, *139* (24), 6569–6579.

(4) Borisov, S. M.; Neurauter, G.; Schroeder, C.; Klimant, I.; Wolfbeis, O. S. *Appl. Spectrosc.*, **2006**, *60* (10), 1167–1173.

(5) Puchalski, M. M.; Morra, M. J.; Wandruszka, R. von. *Fresenius J Anal Chem*, **1991**, *340* (6), 341–344.

(6) Lakowicz, J. R., *Principles of Fluorescence Spectroscopy*; Springer Science+Business Media, LLC, Boston, MA, 2006.

5 Low cost referenced luminescent imaging of oxygen and pH with a 2-CCD colour near infrared camera

Authors: Josef Ehgartner [a], Helmar Wiltsche [a], Sergey M. Borisov [a], and Torsten Mayr [a]

[a] Institute of Analytical Chemistry and Food Chemistry, Graz University of Technology, Stremayrgasse 9/3, 8010 Graz, Austria.

Abstract A low cost imaging set-up for optical chemical sensors based on NIR-emitting dyes is presented. It is based on a commercially available 2-CCD colour near infrared camera, LEDs and tailor-made optical sensing materials for oxygen and pH. The set-up extends common ratiometric RGB imaging based on the red, green and blue channels of colour cameras by an additional NIR channel. The hardware and software of the camera was adapted to perform ratiometric imaging. A series of new planar sensing foils were introduced to image oxygen, pH and both parameters simultaneously. The used NIR-emitting indicators are based on benzoporphyrins and aza-BODIPYs for oxygen and pH, respectively. Moreover, a wide dynamic range oxygen sensor is presented. It allows accurate imaging of oxygen from trace levels up to ambient air concentrations. The imaging set-up in combination with the normal range ratiometric oxygen sensor showed a resolution of 4-5 hPa at low oxygen concentrations (< 50 hPa) and 10-15 hPa at ambient air oxygen concentrations; the trace range oxygen sensor (< 20 hPa) revealed a resolution of about 0.5-1.8 hPa. The working range of the pH-sensor was in the physiological region from pH 6.0 up to pH 8.0 and showed an apparent pKa-value of 7.3 with a resolution of about 0.1 pH units. The performance of the dual parameter oxygen/pH sensor was comparable to the single analyte pH and normal range oxygen sensors.

5.1 Introduction

Since the ancestor of modern cameras, an ancient device called camera obscura, photography and imaging have had a significant impact on human lives. The progress in camera technology, especially the development of digital cameras expanded our options and made the information of an image easily accessible. In the last decades, it was demonstrated that the combination of camera technology and optical chemical sensors

leads to powerful systems to image and quantify analytes by luminescence measurements [1–6]. The concentration of analytes is usually accessed by intensity-based imaging, referenced intensity-based imaging (= ratiometric imaging) or via imaging of luminescence lifetime [7]. Intensity based imaging is the simplest form. There, the analyte concentration causes a change in luminescence intensity of an optical sensor and this change is recorded by the imaging set-up. Unfortunately, this change also depends on other parameters, for example heterogeneity of the light source, sensitivity of the photodetector or homogeneity of the sensor layer, which can lead to measurement inaccuracies. Some of these errors are referenced out by ratiometric imaging [8–12] due to an additional measurement of an analyte-independent (= reference) luminescence intensity signal. Yet, leaching and bleaching of the sensor material are not referenced out, but these properties can be minimized by well-engineered sensor materials. A variation of ratiometric imaging is red-green-blue (RGB) imaging, which uses standard digital photographic cameras as readout and has been used for various types of sensors [13–17]. These cameras are normally sensitive in the visible range of the spectrum and an image usually consists of the blue, green and red channel of the camera. These channels can be split up and used for ratiometric imaging. Luminescent lifetime imaging set-ups [18–22] offer an even more robust imaging system, but are much more expensive than ratiometric imaging platforms [23].

Ratiometric imaging systems combined with optical chemical sensors were used to measure oxygen partial pressure (pO_2) in tumour tissue [24,25], in cancer cells [26], in neurospheres [27], in microfluidic channels [28,29] and marine sediments [16,30], to monitor the pH value during cutaneous wound healing processes [31] or to determine the intracellular pH value [32]. Other analytes such as glucose [12], H_2O_2 [33,34], CO_2 [14,35], heavy metal ions [36–38] or temperature [39,40] were also determined by these techniques. Many of these imaging set-ups are optimized for the visible range and near infrared (NIR) emitting dyes are often not suitable due to low quantum efficiency of the photodetector in the near infrared or because of NIR cut-off filters in front of the photodetector. Nevertheless, the use of NIR sensors can be beneficial for example in tissue monitoring [25,26] due to a higher penetration depth of the excitation and emission light or because of less background luminescence from proteins and other cell constituents. NIR emitting sensors are excited with red light, which has less energy than UV, blue or green light and is therefore less harmful to cells. The NIR part of the electromagnetic spectrum can also provide a window for measuring additional parameters. The purpose of our current work was the development of a low cost ratiometric imaging system for NIR sensors [41–48]. Hence, we adapted the hardware and software of a commercially available 2-CCD NIR-colour (RGB) camera to obtain a simple, more powerful and cheap set-up for referenced luminescence imaging in the visible and NIR. In addition, we developed ratiometric NIR-sensor foils

for imaging of oxygen partial pressure, the pH value and simultaneous detection of pO_2 and pH. In contrast to common ratiometric RGB imaging systems our ratiometric imaging set-up has the advantage that the detection of two analytes and a reference or three analytes is easily accessible due to the additional NIR-CCD chip. Further, the 2- CCD set-up allows ratiometric imaging simultaneously in the visible and in the NIR. The two separate CCD chips do not spectrally overlap like the blue, green and red channels of RGB systems and therefore, the reference and the analyte signal can be recorded independently from each other for single analyte measurements. The spectral overlap in common RGB set-ups usually reduces the sensitivity and the dynamic range of an optical chemical sensor.
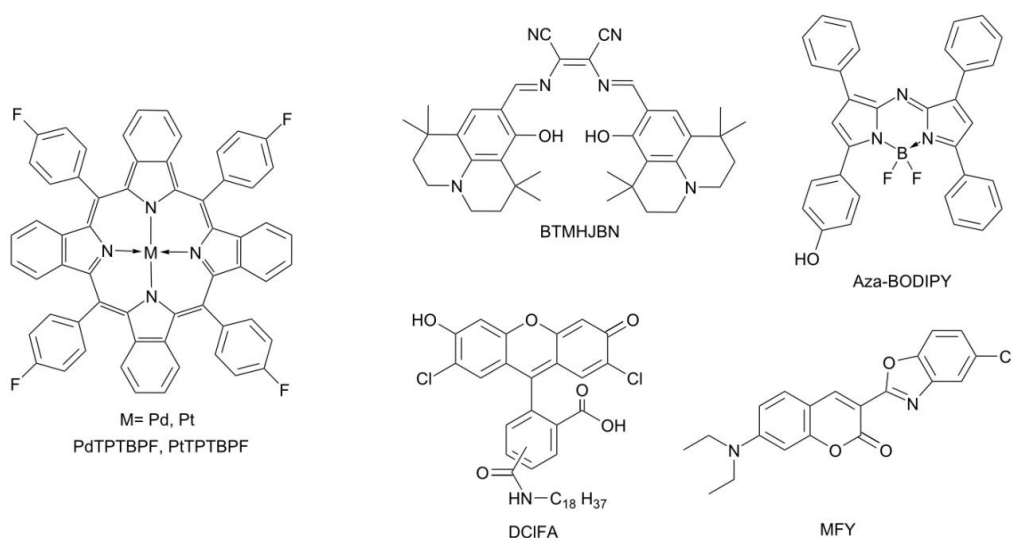
Figure 5.1 Chemical structures of the indicator and reference dyes.

5.2 Experimental

5.2.1 Materials

Palladium(II) and platinum(II) *meso*-tetra(4-fluorophenyl) tetrabenzoporphyrin (PdTPTBPF and PtTPTBPF, respectively, Fig. 5.1), 2,3-bis(3,3,9,9-tetramethyl-2-hydroxyjulolidine)but-2-enedinitrile (BTMHJBN), the BF_2 chelate of [5-(4-hydroxyphenyl)-3-phenyl-1H-pyrrol-2-yl]-[5-phenyl-3-phenyl-pyrrol-2-ylidene]amine (aza-BODIPY) and 2′,7′-dichloro-5(6)-N-octadecyl-carboxamidofluorescein (DClFA) were synthesized in house according to the literature procedures [46-49]. Platinum(II)-5,10,15,20-tetrakis-(2,3,4,5,6-pentafluorphenyl)-porphyrin (PtTFPP) was obtained from Frontier Scientific (www.frontiersci.com); Macrolex Fluorescence yellow® (MFY, (3-(5-chloro-2-benzoxazolyl)-7-(diethylamino)-2H-1-benzo-pyran-2-one) was purchased from Simon and Werner GmbH (www.simon-und-werner.de); fluorescent pigment Brick red

was bought from Kremer Pigmente GmbH & Co KG (www.kremer-pigmente.com); polyurethane hydrogel (Hydromed D4) was obtained from AdvanSource biomaterials (www.advbiomaterials.com); polystyrene (PS; M = 250 000) was purchased from Fisher Scientific (www.fishersci.com). Chloroform, toluene, ethanol, sodium chloride, acetic acid and the buffer salts 2-(Cyclohexylamino)ethanesulfonic acid (CHES) and 2-(N-morpholino)ethanesulfonic acid (MES) were purchased from Roth (www.carl-roth.de); tetrahydrofuran and the buffer salt 3-morpholinopropane-1-sulfonic acid (MOPS); polystyrene beads (2% divinylbenzene, 8 μm) were obtained from Sigma Aldrich (www.sigmaaldrich.com). Polyethylene terephthalate films (thickness 0.125 mm) were bought from Goodfellow (www.goodfellow.com); Teflon® AF 1600 was obtained from DU Pont (www.dupont.com); poly(phenylsilsesquioxane) was purchased from ABCR (www.abcr.de). Gases for calibration were obtained from Linde (www.linde-gas.at).

5.2.2 Preparation of the oxygen sensitive polystyrene particles

A solution of 5 mg of PtTPTBPF in 1 ml of chloroform was added dropwise to the dispersion of 1 g of polystyrene particles in 5 ml of chloroform. The dispersion was stirred at 55°C for 30 min. It was cooled to room temperature and 1.5 ml ethanol were added dropwise into the stirred dispersion. The particles were dried at 50 °C and homogenized in a mortar. The dye absorbed on the surface of the beads was removed by washing 4 times with 40 ml of ethanol.

5.2.3 Preparation and calibration of sensor films for the determination of oxygen

A sensor dye, a reference dye and polystyrene were dissolved in chloroform to obtain a sensor "cocktail". This "cocktail" (150 μl) was knife coated onto dust-free polyethylene terephthalate films by using a bar film applicator (25 μm, www.byk.com). The solvent was evaporated in a drying oven at 60 °C to result in an about 2.0 μm thick sensor film. The used dyes and the initial masses of all components are shown in Tab 5.1.

Table 5.1 Input masses of the sensor "cocktails".

Sensor dye /mg	Ref. dye /mg	Polystyrene /mg	Chloroform /g
PtTPTBPF / 1.3	MFY / 3.1	160	2.1
PdTPTBPF / 1.0	MFY / 1.1	100	1.4
PtTPTBPF / 1.0	BTMHJBN /1.1	200	2.9
PtTFPP / 0.9	MFY / 0.3	270	2.7

A second layer of an oxygen trace sensor was spin-coated onto the PtTFPP/MFY layer to obtain a wide dynamic range oxygen sensor. For the second layer PdTPTBPF (10 mg) and poly(phenylsilsesquioxane) (1 g) were dissolved in chloroform (3 ml). The solvent was evaporated under a nitrogen gas stream overnight and the mixture was sintered at 170 °C

for four hours in an oven. The sinter was suspended in water/ethanol (4+1 v/v) and was ground in a ball mill (6 hours; 400 rpm). The powder was dried overnight in an oven and a portion (82 mg) was suspended in perfluorodecalin (1.2 g) containing 5 % of the fluoropolymer Teflon® AF 1600. This mixture (350 µl) was spin-coated for 30 s at 3000 rpm onto the PtTFPP/MFY film by the spin coater WS-650-23NPP Modular Spin Processor (www.laurell.com). The solvent was evaporated in a drying oven at 60°C. For a schematic pattern of the sensor foils see supplementary information.

Three foils of each sensor film were calibrated. The sensors PtTPTBPF/MFY, PdTPTBPF/MFY and PtTFPP/MFY/ PdTPTBPF were gas-phase calibrated in a home-made calibration chamber. PtTPTBPF/BTMHJBN was calibrated in a glass vessel sealed with a lid and filled with water. Two mass flow controller instruments (Read Y smart series) by Vögtlin instruments (www.voegtlin.com) were used to obtain gas mixtures of defined pO_2. Compressed air and nitrogen or 2 % (v/v) oxygen in nitrogen and nitrogen were used as calibration gases. The calibration gas was passed through a glass gas washing bottle (filled with wet silica gel) which was dipped into a temperature-controlled (25 °C) water bath to keep the temperature constant. The exact oxygen concentration and the temperature in the calibration vessel were determined with an optical oxygen meter (FireStingO2) from Pyroscience connected to a fiber-optic oxygen sensor and a temperature sensor (www.pyro-science.com). The sensors with Macrolex Fluorescence yellow as reference dye were excited with a 458 nm high power 10 W LED array (www.led-tech.de). The filter set consisted of the excitation filter BG12 (350-470 nm) and the long-pass emission filter OG515 (515 nm) from Schott (www.schott.com). The Lee filter Oklahoma yellow (www.edmundoptics.com) was fixed in front of the OG515 filter to reduce its fluorescence and the background signal. The sensor with BTMHJBN as reference dye was excited with a 617 nm high power 30 W LED array (www.led-tech.de). The filter set consisted of the band-pass excitation filter Bk 620/25 (www.interferenzoptik.de) and the long-pass emission filter edge basic 633 LP (www.semrock.com). The Lee filter Medium red was fixed in front of the long-pass emission filter to reduce its fluorescence and the background signal.

5.2.4 Preparation and calibration of pH planar optodes

BTMHJBN (0.5 mg) as reference dye and polystyrene (500 mg) were dissolved in toluene (2.7 g). This mixture (350 µl) was spin-coated for 30 s at 3000 rpm onto a dust-free polyethylene terephthalate film by a spin coater. The solvent was evaporated in a drying oven at 70 °C. The dried reference layer was covered with a pH-sensor layer by spin coating. Hence, a pH indicator (1.0 mg) — aza-BODIPY — was dissolved in 100 µl of THF and was diluted with an ethanol + water 9+1 (w/w, 2.2 g) containing 10 % w/w hydrogel D4. 350 µl of this sensor "cocktail" were spin-coated onto the reference layer as described

above. The solvents were evaporated in a drying oven at 70 °C (schematic drawing of the sensor foil see supplementary information).

Three foils of the pH sensor were calibrated; therefore, buffer solutions (MES, MOPS, CHES) at different pH values were used. The buffers were adjusted to constant ionic strength (IS = 0.15 M) using sodium chloride as a background electrolyte. The pH of the buffer solutions was controlled by a digital pH meter (SevenEasy, Mettler-Toledo, www.mt.com) equipped with a glass electrode (InLab Routine Pro, Mettler-Toledo). The glass electrode was calibrated with standard buffers of pH 4.1, pH 7.1 and pH 10.1 (Hanna instruments, www.hannainst.com). A Petri dish was used as calibration vessel. A 617 nm high power 30 W LED array was used as excitation source. The filter set consisted of the band-pass excitation filter Bk 620/25 and the long-pass emission filter edge basic 633 LP (www.semrock.com). The Lee filter Medium red was fixed in front of the long-pass emission filter to reduce its fluorescence and the background signal.

5.2.5 Preparation of sensor films for the simultaneous determination of oxygen and the pH value

The pH indicator DClFA (0.8 mg), polystyrene particles containing 1 % w/w PtTPTBPF as oxygen indicator (130 mg), fluorescent pigment Brick red (7.8 mg) as reference particles and ethanol + water 9+1 (w/w, 1.5 g) containing 15 % w/w hydrogel D4 were mixed to obtain a sensor "cocktail". 150 μl of this "cocktail" were knife coated onto dust-free polyethylene terephthalate films by using a bar film applicator (25 μm). The solvent was evaporated in a drying oven at 60 °C to result in a ca. 3.8 μm thick sensor film (schematic drawing of the sensor foil see supplementary information).

Three foils of the oxygen/pH sensor were fixed in a glass vessel and sealed with a lid. The pH value was adjusted by different buffer solutions (acetic acid/sodium acetate, MES, MOPS, CHES) and the oxygen concentration was regulated by bubbling mixtures of compressed air and nitrogen at different ratios through the solution. The pH values of the buffer solutions were controlled as described above. The oxygen mixtures were obtained by two mass flow controller instruments. The oxygen concentration and the temperature within the buffer solution were online monitored with an optical oxygen meter. A 458 nm high-power 10-W LED array was used as excitation source. The filter set consisted of the excitation filter BG12 and the long-pass emission filter OG515. The Lee filter Oklahoma yellow was fixed in front of the OG515 filter to reduce its fluorescence and the background signal.

5.2.6 Spectral measurements

Emission spectra were acquired on a Hitachi F-7000 fluorescence spectrometer (www.hitachi-hta.com) equipped with a red-sensitive photomultiplier tube (PMT) R 928

from Hamamatsu (www.hamamatsu.com). The emission spectra were corrected for the sensitivity of the PMT.

5.2.7 Imaging setup and data evaluation

The imaging set-up consisted of a commercial RGB-NIR camera Jai AD-130GE (www.jai.com) equipped with a 6-mm-focal-length chromatic aberration corrected lens (CVO GMHR3D26018C, www.stemmer-imaging.de), an LED array, optical filters and a sensor foil (Fig. 5.2). The software platform common vision blox (CVB 2011) from Stemmer Imaging was used to adapt the measuring software. More details and the source code of the program can be found in the supplementary information. An external trigger source was built using the Arduino open source microcontroller platform (www.arduino.cc) to extent the exposure time of the camera up to two seconds (more details see supplementary information). The current fed to the LED array was also microcontroller adjusted by means of a field effect transistor (FET) operated in linear mode. Contrary to pulse width modulation, this linear current regulation avoided additional flicker noise in the case of very short CCD exposure time.
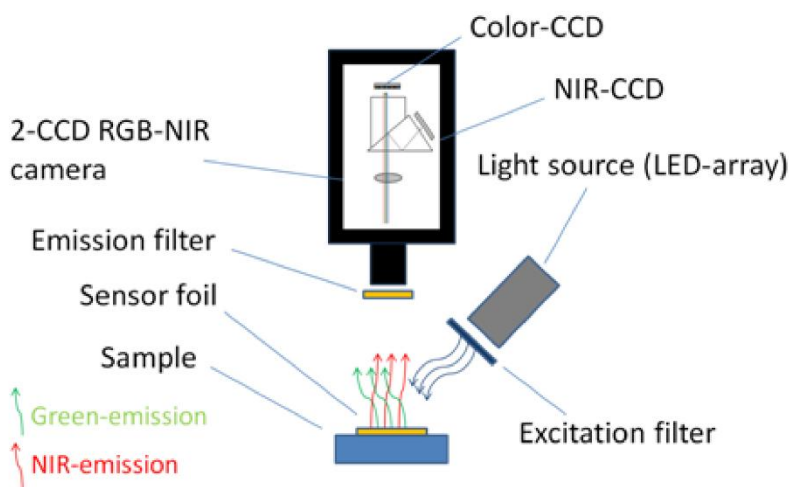
Figure 5.2 Schematic drawing of the imaging set-up.

During data acquisition, two images were recorded by the camera under continuous excitation of the sensor foil. Low ambient light conditions were necessary during acquisition to minimize the background signal. One image contained the near infrared information and the other image contained the colour information (channel). The images had a size of 1296 (h) x 966 (v) pixels at 12 bit resolution which is equivalent to 4096 greyscale values. The colour channel was separated into a blue, green and red channel each also comprising of 12 bit signal information. A ratiometric image R was obtained by dividing the channel containing the analyte dependent signal, for example

the near infrared channel, by the channel containing the reference (analyte independent) signal, for example the green channel. This process was done pixel by pixel by a self-written MATLAB script; therefore, each pixel contained referenced information about the analyte. MATLAB R2009a (www.mathworks.com) was used for image processing. Also NIR and colour blank-images were recorded. These images were acquired under identical acquisition parameters (e.g. shutter time, brightness of the LED array etc.) but without a sensor foil to obtain the background signal of the measurement conditions. These background signals were subtracted from the recorded images. Calibration curves were obtained by calculating the mean value and the standard deviation of a certain region of pixels (region of interest) of a referenced image at different analyte concentrations. Fitting of the calibration data was performed using OriginLab 8.5 (www.originlab.com).

5.3 Results and Discussion

5.3.1 Imaging setup for ratiometric imaging

The main component of the detection system is the camera Jai AD-130GE, which contains two 1/3" CCD chips. One chip is sensitive in the visible region of the spectrum and contains the blue, green and red channel (Bayer colour filter array) and the other chip is sensitive in the NIR region and contains the NIR channel. The spectral response of the camera is shown in Fig. 5.3. Special lenses should be used with this camera to minimize the chromatic aberration. A ratiometric optical sensor usually consists of an analyte indicator dye and an analyte independent reference dye; hence, this camera is ideally suited for ratiometric imaging due to its ability of recording the analyte signal and the reference signal in separate channels or chips of the camera. The two chip set-up provides distinct advantages over common one chip RGB systems In comparison to the detection with monochrome cameras the 2-CCD system does not need additional equipment and moving parts, for example a filter wheel or a slider. Moreover, the NIR-chip offers an additional window for the determination of further analytes. Three-analyte detection can be performed by simultaneous detection of a reference and two analyte indicators on the RGB-chip and of an additional analyte indicator on the NIR-chip. Compared to RGB systems the 2-CCD camera is better suited for the detection of NIR-emitting optical chemical sensors. These novel sensors are beneficial in applications such as tissue monitoring or imaging of cells and biofilms in order to reduce the inherent background luminescence from biological material and from the surrounding medium itself; e.g. common cell culture media show strong autofluorescence in the visible part of the electromagnetic spectrum. Another advantage is the increased penetration depth

into the tissue of the red excitation light of NIR emitting dyes, which is important in medical applications such as imaging of organs.
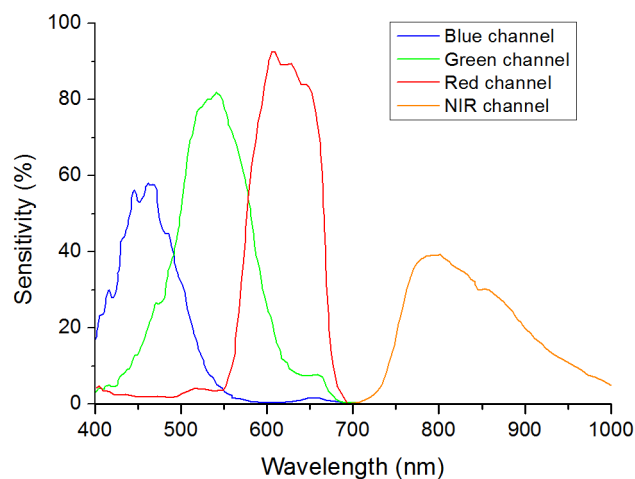
Figure 5.3 Spectral response of the camera and the 4-channels adapted from Jai (www.jai.com).

Further, the exposure time of the 2-CCD camera can be set individually for each chip and thus can be used to optimize the signals based on the brightness of the dyes if the reference and the analyte signal are recorded on separate chips. In one chip systems, for example RGB imaging, the adjustment will always be a compromise since the brightness of individual indicators may vary significantly and can only be achieved by changing the concentrations of the dyes within the sensor film. Another advantage of two chip cameras is that they offer more flexibility for the used sensor dyes. Dyes for a ratiometric imaging system must match the spectral properties of the camera. When using one chip imaging systems, the emission of a dye often overlaps with two, rather than one, channel of interest and therefore the analyte signal or the reference signal or both are influenced by each other. This property can make quantification difficult or even impossible. In one chip systems, this spectral overlap often leads to decreased sensitivity and to a narrower dynamic range of an optical chemical sensor. The used two chip camera offers more opportunities as reference signal and analyte signal of a sensor can be detected on independent chips without overlaps. In principle, spectral interference can be minimized or eliminated by using dedicated band-pass filters for each luminescent component. However, in order to enable fast measurements fast moving mechanical parts (filter-wheels) are essential. This results in high equipment costs (approx. 5 times higher than the dual chip camera). Our ratiometric imaging set-up consists of rather simple and cost-efficient instrumentation (approx. 3000 €) and offers in contrast to intensity-based imaging the advantage of compensating some disturbing effects for

example heterogeneous thickness of the sensor films or the inhomogeneity of the light source. Fig. 5.4 illustrates these effects; the NIR intensity of a sensor foil over a certain region of pixels shows a drift and the signal dynamic at two different analyte concentrations changes within the intensity image (left), while the referenced value R (NIR intensity/green intensity) and the signal dynamic of this region remains constant (right) for the ratiometric image. Calibration of the sensor foil based on the intensity image is thus prone to error compared to the referenced image. Evidently, slight changes in position of the camera and excitation source will negatively affect the intensity-based measurement. For accurate ratiometric measurements a constant ratio of the dyes within the sensor film is required; thus, the sensor foils must be homogeneous. In addition, scratches in the sensor foil can lead to errors due to interferences by refraction (a wavelength-dependent effect). Another source of error could be introduced by the measured sample itself if the sample randomly changes the ratio of the detected intensities by heterogeneous absorption or intrinsic luminescence [7].
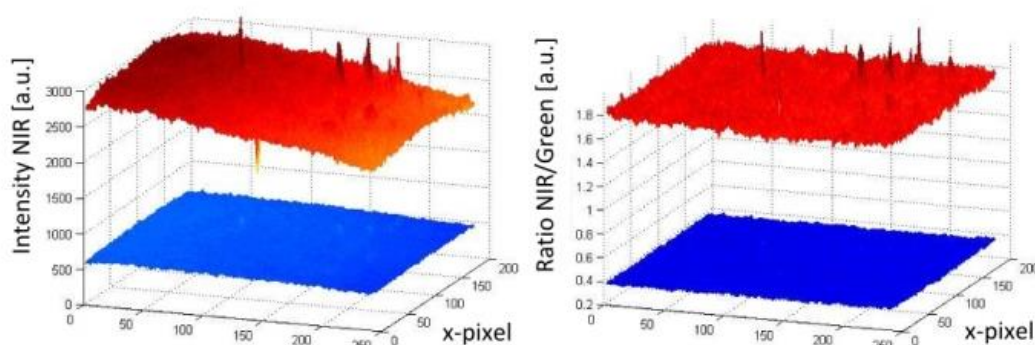
Figure 5.4 Comparison of a pixel area recorded by intensity based imaging (left) and ratiometric imaging (right).

5.3.2 Sensor films for imaging of pO$_2$

Common optical oxygen sensors have limited dynamic ranges and show either a good resolution at low oxygen concentrations or at high oxygen concentrations. In some application, e.g. imaging of biofilms, it might be useful to have a sensor with a wider dynamic range. Therefore, a wide dynamic range sensor was developed to image oxygen at trace levels and at ambient air conditions or even above. The advantage of this sensor over common oxygen sensors is the improved resolution for oxygen over the whole calibration range. The wide dynamic range sensor is composed of two sensing layers. The lower layer consisted of platinum(II)-5,10,15,20-tetrakis-(2,3,4,5,6-pentafluorphenyl)-porphyrin (PtTFPP) as oxygen indicator dye and the commercially available coumarin Macrolex Fluorescence Yellow® (MFY), both dyes were incorporated into a polystyrene film. PtTFPP emitted in the red channel of the camera and MFY

emitted in the green camera channel. The upper layer consisted of poly-(phenylsilsesquioxane) particles with physically entrapped palladium(II) meso-tetra(4-fluorophenyl) tetrabenzoporphyrin (PdTPTBPF) incorporated into a fluoropolymer film. PdTPTBPF offers the advantages that it emits in the NIR, is excitable with blue or red light and is very photostable [50].The combination of poly(phenylsilsesquioxane) and PdTPTBPF acts as an oxygen trace sensor within the wide dynamic range sensor because poly(phenylsilsesquioxane) is highly permeable for oxygen and PdTPTBPF is highly sensitive to oxygen due to its long luminescence decay time ($\tau_0 \sim 350$ µs at 25 °C). The emission of MFY in the green channel of the camera was used as reference signal for both oxygen indicators. Single layer systems were developed to offer even more accessible and more reproducible ratiometric optical oxygen sensors and to show the performance of the camera. Single layer systems usually show better homogeneity than dual layer systems and are easier to prepare. The single layer systems used either PdTPTBPF or platinum(II) *meso*-tetra(4-fluorophenyl) tetrabenzo-porphyrin (PtTPTBPF) as oxygen indicator dye. The oxygen sensitive dye was incorporated with MFY into a polystyrene film. PdTPTBPF was used to determine oxygen at trace levels and PtTPTBPF (which has significantly shorter luminescence decay times) to detect oxygen up to air saturation and above (normal range oxygen sensor). PtTPTBPF and PdTPTBPF offer the advantages that they are excitable with blue or red light, emit in the NIR and are very photostable [50]. These ratiometric single layer systems were excitable with blue light, which in some applications can cause a higher background fluorescence and therefore another system was introduced which uses 2,3-bis(3,3,9,9-tetramethyl-2-hydroxyjulolidine)but-2-enedinitrile (BTMHJBN) as a red-excitable reference dye [47]. Its fluorescence was detected in the red channel of the camera. The oxygen indicator and the reference dye were also incorporated into a single polystyrene layer.

The spectra and Stern-Volmer calibration curves for each sensor system were recorded in triplicates and are shown in Fig 5.5. Each calibration point represents the mean value of the three independent measurements and each error bar corresponds to the standard deviation. An adapted version of the two-site model, the simplified two-site model, was used to fit the calibration data (equation 5.1) [51].

$$\frac{I_0}{I} = \frac{R_0}{R} = \left(\frac{f_1}{1 + K_{SV} * pO_2} + f_2 \right)^{-1} \quad (5.1)$$

The ratio I_0/I in the model was replaced by R_0/R where R is the ratio of the measured intensity of the oxygen indicator dye divided by the intensity of the reference dye at a certain pO_2 value. R_0 represents this ratio under deoxygenated conditions, where the oxygen indicator is in its unquenched state. The parameter K_{SV} describes the quenching

efficiency and thus the sensitivity of the sensor, while the parameters f_1 and f_2 characterize different fractions of dye molecules. The dye molecules in fraction f_1 are quenched at a certain K_{SV}, whereas the molecules in fraction f_2 ($f_2 = 1 - f_1$) are unquenchable ($K_{SV} = 0$).
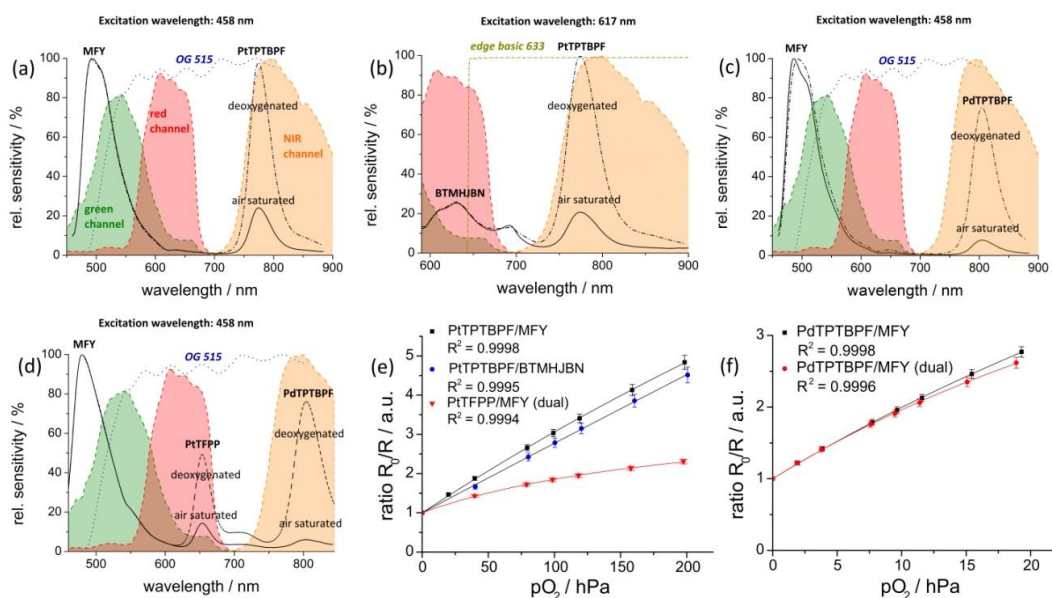
Figure 5.5 Spectral properties (a-d) of the oxygen imaging set up at deoxygenated and air saturated conditions; shown are the spectral sensitivity of the camera channels, the emission spectra of the dye systems PtTPTBPF/MFY (a), PtTPTBPF/BTMHJBN (b), PdTPTBPF/MFY (c) and PtTFPP/MFY/PdTPTBPF (d)] and the spectra of the emission filters (OG 515 and edge basic 633). Stern-Volmer calibration curves (e-f) for the oxygen optodes at 25°C. Lines indicate a fit according to equation 5.1.

The sensitivity (slope of the calibration curve) of the sensor system PtTPTBPF/BTMHJBN (K_{SV} = 18.0 x 10^{-3} x hPa^{-1}; f_1 = 0.996) was slightly decreased in comparison to PtTPTBPF/MFY (K_{SV} = 23.0 x 10^{-3} x hPa^{-1}; f_1 = 0.967), which resulted from a weak background emission of BTMHJBN in the NIR channel of the camera. The calibration parameters of the single layer trace oxygen sensor (PdTPTBPF/MFY) were K_{SV} = 120 x 10^{-3} x hPa^{-1} and f_1 = 0.913. The calibration parameters of the dual layer system were K_{SV} = 16.9 x 10^{-3} x hPa^{-1} and f_1 = 0.734 for the lower layer (PtTFPP/MFY) and K_{SV} = 129 x 10^{-3} x hPa^{-1} and f_1 = 0.869 for the upper layer (PdTPTBPF entrapped into the poly(phenylsilsesquioxane) particles). The data showed good precision as the relative standard deviation for each calibration point was within 2-5 %. The sensors employing the NIR channel show a significantly higher sensitivity compared to an RGB sensor systems because of recording the analyte signal and the reference signal on separate chips on the camera. Obviously, the calibration curve of the PtTFPP/MFY system of the dual sensor, which is virtually a RGB system, and the calibration curve of the

PtTPTBPF/MFY dye system illustrate this and is in accordance with reported ratiometric sensor systems with comparable sensor composition [28]. The exposure time of the NIR chip (approx. 20-30 ms) was similar for all oxygen optodes in contrast to the exposure time of the RGB chip. There, the exposure time of the red-light excitable oxygen optode (approx. 300-500 ms) had to be set five to ten times longer in comparison to the blue-light excitable system (approx. 30-50 ms) due to a lower intensity of the reference signal within the used part of the camera channel (Fig. 5.5). If higher signals in the red channel are needed, this can be realized either by using a shorter excitation wavelength for example an amber LED array (approx. 590 nm) in combination with a different filer set-up or by changing the ratio of the dyes within the red excitable optode.

Pseudo colour images of the near infrared intensity, of the green intensity and of the ratiometric image (each pixel represents the R-value) for PtTPTBPF/MFY at 0 hPa, 100 hPa and 200 hPa oxygen are shown in Fig 5.6. The ratiometric images are very homogeneous in contrast to the pure intensity-based images which are very heterogeneous and thus calibration at different region of interest would lead to different intensity values. Tiny heterogeneous areas in the ratiometric images result from small scratches of the sensor foil and wavelength-dependent diffraction of NIR and green emission light at these sides. The resolution of the imaging set-up for the normal range oxygen sensor (PtTPTBPF/MFY and PtTPTBPF/BTMHJBN) was about 4-5 hPa at low oxygen concentration (< 50 hPa) and about 10-15 hPa at ambient air oxygen concentrations; the trace range oxygen sensor (< 20 hPa; PdTPTBPF/MFY) showed a resolution of about 0.5-1.8 hPa. The wide dynamic range sensor combined the beneficial behaviour of both sensor types and showed a resolution of 0.5-1.8 hPa at low oxygen concentrations (< 20 hPa) and about 10-15 hPa at ambient air oxygen concentrations.
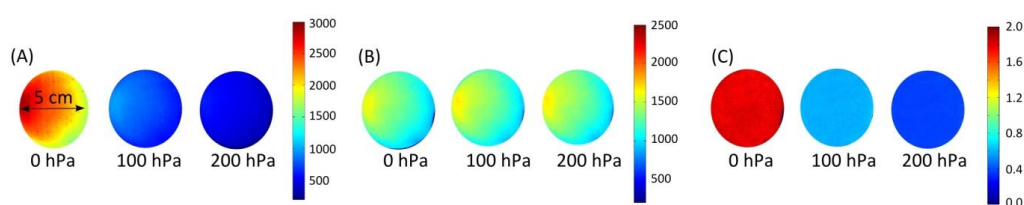
Figure 5.6 Pseudo colour images of the NIR intensity channel (A), of the green intensity channel (B) and of the ratiometric images (C) at different oxygen partial pressures for the oxygen optode PtTPTBPF/MFY.

5.3.3 Sensor films for imaging of pH

The pH value is an important analytical parameter in many environmental systems and applications; therefore we demonstrated the applicability of our imaging set-up on a red excitable ratiometric pH sensor. As mentioned above longer excitation and emission wavelength are beneficial because they reduce the inherent background luminescence from biological samples. Hence, the BF$_2$ chelate of *[5-(4-hydroxyphenyl)-3-phenyl-1H-*

pyrrol-2-yl]-[5-phenyl-3-phenyl-pyrrol-2-ylidene]amine (aza-BODIPY) was used as a pH indicator dye because it emits in the NIR region, is very photostable and has high molar absorption coefficients and a good quantum yield [48]. *2,3-bis(3,3,9,9-tetramethyl-2-hydroxyjulolidine)but-2-enedinitrile* (BTMHJBN) was used as a red-light excitable reference dye, which emits in the red channel of the imaging set-up (Fig. 5.7). A two layer system was necessary for the sensor because the reference dye had to be incorporated into a pH insensitive matrix due to its pH sensitive hydroxyl groups; therefore polystyrene was used as a permeation selective protective matrix. The aza-BODIPY dye was immobilized in a polyurethane hydrogel D4 film upon the polystyrene layer. In two layer systems the ratio of the layer thicknesses must be similar across the imaged region; otherwise the variations of the layer thicknesses have to be determined for each pixel, which is theoretically possible but inefficient and prone to error. Spin coating was applied to obtain nearly equal distributed sensor layers.

  Calibration curves of the sensor system were recorded in triplicates and are shown in Fig. 5.7 (mean value and standard deviation). The data was fitted by the Boltzmann function shown in equation 5.2, where R is the ratio of the measured intensities of the pH indicator dye and the reference dye at a certain pH value, A_1 and A_2 represent empirical parameters describing the initial value ($A_1 = 1.244$) and the final value ($A_2 = 0.389$), x_0 describes the point of highest sensitivity (apparent pK_a value) of the sensor ($x_0 = 7.294$), and dx the pH constant of the fitting curve (dx = 0.449).

$$R = \frac{A_1 - A_2}{1 + exp^{\left(\frac{x - x_0}{dx}\right)}} + A_2 \quad (5.2)$$

The measurement points showed good precision as the relative standard deviation for each calibration point was within 3-4 %. The ratiometric pH sensor had a working range from about pH 6.0 up to pH 8.0 and a pK_a value of 7.3, which is ideal for physiological studies. The working range of the pH sensor can be simply adjusted by using other aza-BODIPY dyes with different substitution patterns as described in the literature [48]. It should be mentioned that optical pH-sensors have a limited working range typically within 2 to 3 pH-units, which is adequate for most applications since the pH changes are typically not very high. The referenced pseudo colour images are shown in Fig 5.7 and indicate a very homogeneous spatial distribution within the sensing area. The resolution of the imaging set-up and the sensor film around the apparent pK_a value was about 0.1 pH units. Further investigations will focus on the development of single layer sensor films. The reference dye might be incorporated in proton-impermeable nano- or microparticles which are dispersed in the hydrogen layer.
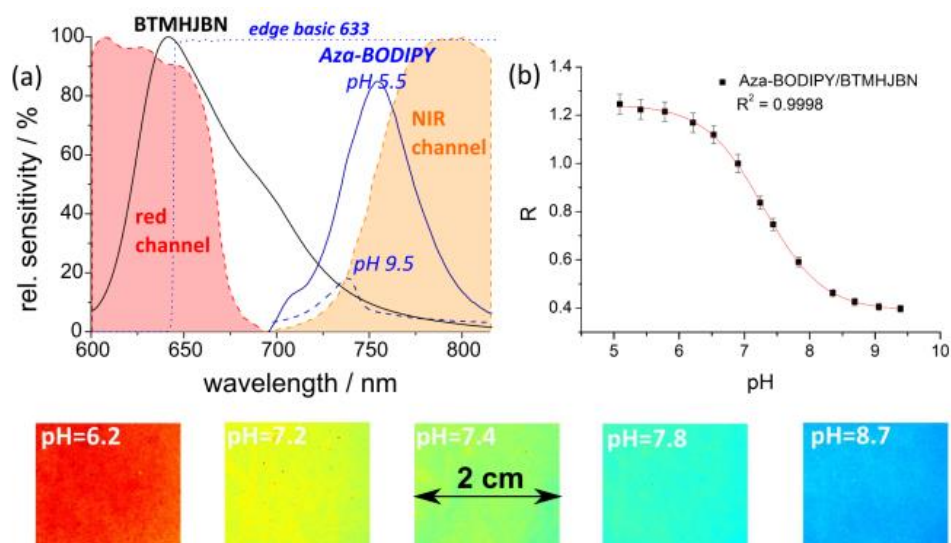
Figure 5.7 Spectral properties of the pH imaging set-up at pH 5.5 and 9.5 (a); shown are the spectral sensitivity of the camera channels, the emission spectra of the used dyes (BTMHJBN and Aza-BODIPY) and the spectrum of the emission filter (edge basic 633); calibration curve (b) for the pH optode at 25 °C. Lines indicate a fit according to equation 5.2. Below: Pseudo colour images of the referenced images of the pH sensor film at different pH values.

5.3.4 Sensor films for simultaneous imaging of pH and pO₂

The simultaneous detection of different analytes for example oxygen, temperature, pH, CO_2 or glucose is of great importance in order to monitor, control and understand processes of all kinds [52–57]. Multi-parameter detection can also be performed with the described imaging set-up and is demonstrated by an optode for simultaneous detection of the pH value and the oxygen concentration. For the pH/oxygen sensor 2′,7′-dichloro-5(6)-N-octadecyl-carboxamido-fluorescein (DClFA) was used as pH indicator dye; its fluorescence was detected in the green channel of the camera. The fluorescent pigment Brick red, which emits in the red channel, was used as reference dye; PtTPTBPF was entrapped into polystyrene particles to determine the oxygen partial pressure in the NIR channel (Fig. 5.8). The entrapment was performed to minimize interactions with the other dyes (e.g. FRET). All these constituents were embedded into a hydrogel D4 matrix; the dyes are lipophilic enough not to be washed out [54].
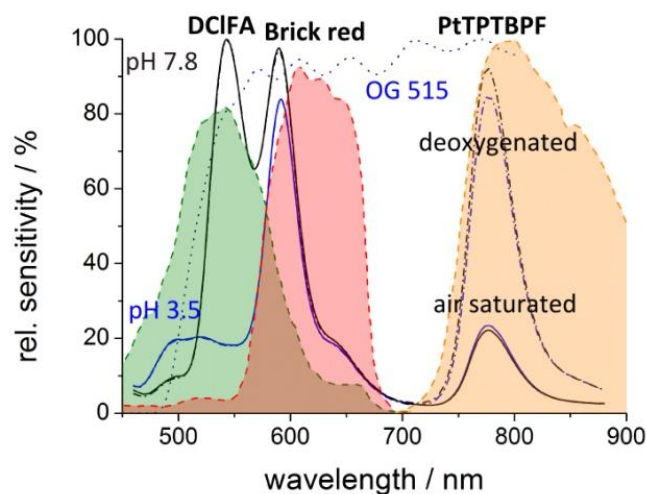
Figure 5.8 Spectral properties of the dual parameter oxygen/pH sensor set-up at different pH-values (3.5 and 7.8) and at different oxygen concentrations (air saturated and deoxygenated); shown are the spectral sensitivity of the camera channels, the emission spectra of the used dye system (DClFA, BrickRed and PtTPTBPF) and the spectrum of emission filters (OG 515).

In comparison to single analyte sensing films, the calibration and quantification schemes of multi-parameter sensors can be more difficult as spectral overlaps of a dye with two camera channels can occur. In our system, a portion of the fluorescence of DClFA is detected in the red channel and disturbs the reference signal. This overlap does not disturb the pH measurement, but influences the oxygen detection. For the pH measurement, the ratio of the green channel (pH dependent signal) to the red channel (reference signal) changes due to this overlap, but this change is proportional to the pH value. The determined oxygen concentration in contrast would be falsified by a change of the pH value because a pH change influences the reference signal and therefore the oxygen signal even when the oxygen level stays constant. To overcome this problem, the intensity value of the red channel has to be reduced as a function of the green signal as shown in equation 5.3.

$$Red\ signal_{corrected} = Red\ signal - Green\ Signal * f \quad (5.3)$$

A portion (*f*) of the green signal which reflects the spectral overlap has to be subtracted from the red signal. This portion can be empirically determined by the use of a sensor film without a reference dye; there, the ratio of the red to the green channel reflects the spectral overlap. Calibration of the sensor at different pH values and at a certain oxygen concentration would also lead to this factor; for our multi-parameter sensor this factor was 0.245. Fig. 5.9 illustrates the reliability of the used correction equation. In this context, the degradation of the sensor layers by photobleaching or leaching is a critical point because these effects can change the measured signals and make a comparison of

the signals with the calibration curve difficult. Hence, the indicator dyes DClFA and PtTPTBPF were chosen because of their high photostability [57]. In addition, photobleaching can be minimized by reducing the light intensity and the turn-on time of the excitation source.
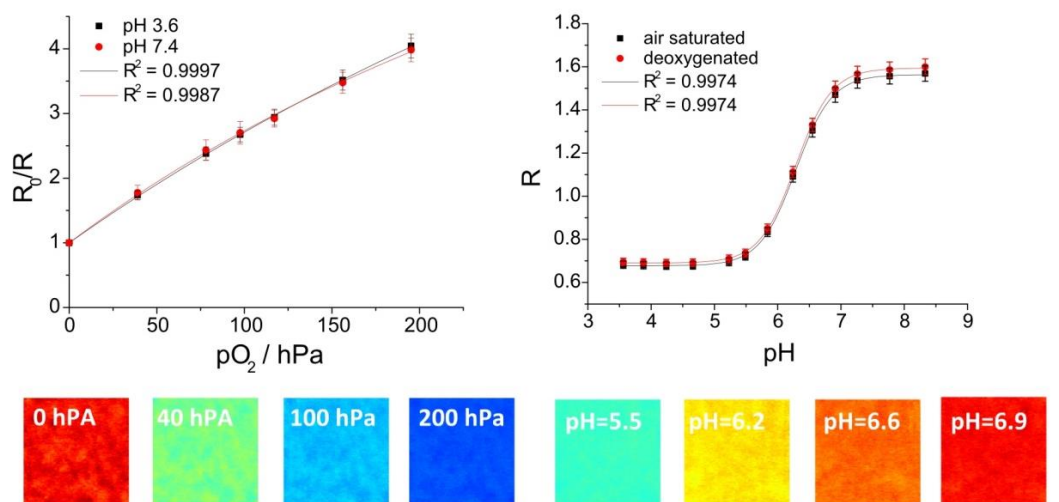
Figure 5.9 Above: Calibration curves of the dual-parameter oxygen/pH sensor at 21 °C. Lines indicate a fit according to equations 5.1 and 5.2. Below: Pseudo colour images of the dual-parameter oxygen/pH sensor at certain oxygen concentrations and pH values.

Stern-Volmer calibration curves and pH calibration curves were recorded in triplicates (Fig.5.9) and processed as mentioned above. The fitting parameters for the Stern-Volmer curves were $K_{SV} = 21.3 * 10^{-3}$ hPa and $f_1 = 0.930$; the relative standard deviation for each calibration point was within 4-6%. The resolution of the oxygen sensor was 25-30 hPa at high oxygen concentrations and 6-10 hPa at low oxygen concentrations. The fitting parameters for the pH sensor were $A_1 = 0.677$ (air saturated) and 0.690 (deoxygenated), $A_2 = 1.563$ (air saturated) and 1.594 (deoxygenated), $x_0 = 6.285$ and $dx = 0.285$. The sensor had a working range of pH 5.5 to 7.0 and an apparent pK_a value of 6.3 and the resolution in the vicinity of the pK_a was about 0.1 pH units. The referenced pseudo colour images of the oxygen and pH sensor films are illustrated in Fig. 5.9. The oxygen images showed in comparison to single layer systems more heterogeneous areas due to a slightly unequal distribution of the oxygen particles; thus, the resolution for oxygen of the dual-parameter sensor was lower than with the single layer oxygen sensor films. The homogeneity of the pH images was comparable to the two layer system. The dual-parameter oxygen/pH sensor can be a useful tool for example in biology to image oxygen and pH distributions or changes in biofilms.

5.4 Conclusion

We presented a new imaging set-up for simultaneous detection of optical chemical sensors emitting in the visible and in the NIR region of the electromagnetic spectrum. The dual chip camera offers the opportunity of two separate chips and therefore minimizes the optical cross-talk and allows real time measurements at four wavelengths (without moving parts) at low costs. The set-up is compatible with high performance NIR sensing materials allowing more reliable measurements in scattering media and biological samples because of an increased optical transparency and less autofluorescence in the NIR regime. The simultaneous determination of at least two parameters is also possible as shown with this measurement system. We demonstrated that ratiometric imaging of oxygen, pH and both parameters simultaneous can be accomplished with high accuracy by our developed optical optodes. Moreover, we developed a wide dynamic range oxygen sensor which allows accurate oxygen measurements over the whole calibration range. The imaging system can be adapted to a large variety of different optical sensors and will be applicable to many analytes and applications varying from marine science to microfluidics or biotechnology or food packaging. Ongoing investigations will focus on multi-parameter detection.

5.5 References

(1) Kenworthy, A. K. *Methods*, **2001**, *24* (3), 289–296.

(2) Ke, S.; Wen, X.; Gurfinkel, M.; Charnsangavej, C.; Wallace, S.; Sevick-Muraca, E. M.; Li, C. *Cancer Research*, **2003**, *63* (22), 7870–7875.

(3) Vinogradov, S. A.; Lo, L. W.; Jenkins, W. T.; Evans, S. M.; Koch, C.; Wilson, D. F. *Biophysical Journal*, **1996**, *70* (4), 1609–1617.

(4) Yang, M.; Baranov, E.; Moossa, A. R.; Penman, S.; Hoffman, R. M. *Proceedings of the National Academy of Sciences*, **2000**, *97* (22), 12278–12282.

(5) Glud, R. N.; Ramsing, N. B.; Gundersen, J. K.; Klimant, I. *Mar. Ecol. Prog. Ser.*, **1996**, *140*, 217–226.

(6) Glud, R. N.; Kühl, M.; Kohls, O.; Ramsing, N. B. *Journal of Phycology*, **1999**, *35* (2), 270–279.

(7) Gregor Liebsch, Dissertation, *Time-resolved luminescence lifetime imaging with optical chemical sensors: set up, controlling, concepts and applications,* University of Regensburg, Regensburg, 2000.

(8) Cao, Y.; Lee Koo, Y.-E.; Kopelman, R. *Analyst*, **2004**, *129* (8), 745–750.

(9) Wu, C.; Bull, B.; Christensen, K.; McNeill, J. *Angew. Chem. Int. Ed. Engl.*, **2009**, *48* (15), 2741–2745.

(10) Domaille, D. W.; Zeng, L.; Chang, C. J. *J. Am. Chem. Soc.*, **2010**, *132* (4), 1194–1195.

(11) Im, S. H.; Khalil, G. E.; Callis, J.; Ahn, B. H.; Gouterman, M.; Xia, Y. *Talanta*, **2005**, *67* (3), 492–497.

(12) Xu, H.; Aylott, J. W.; Kopelman, R. *Analyst*, **2002**, *127* (11), 1471–1477.

(13) Aigner, D.; Ungerböck, B.; Mayr, T.; Saf, R.; Klimant, I.; Borisov, S. M. *J. Mater. Chem. C*, **2013**, *1* (36), 5685–5693.

(14) Ali, R.; Lang, T.; Saleh, S. M.; Meier, R. J.; Wolfbeis, O. S. *Anal. Chem.*, **2011**, *83* (8), 2846–2851.

(15) Fischer, L. H.; Karakus, C.; Meier, R. J.; Risch, N.; Wolfbeis, O. S.; Holder, E.; Schäferling, M. *Chemistry*, **2012**, *18* (49), 15706–15713.

(16) Larsen, M.; Borisov, S. M.; Grunwald, B.; Klimant, I.; Glud, R. N. *Limnol. Oceanogr. Methods*, **2011**, *9* (9), 348–360.

(17) Wang, X.-d.; Gorris, H. H.; Stolwijk, J. A.; Meier, R. J.; Groegel, D. B. M.; Wegener, J.; Wolfbeis, O. S. *Chem. Sci.*, **2011**, *2* (5), 901.

(18) Lakowicz, J. R.; Szmacinski, H.; Nowaczyk, K.; Berndt, K. W.; Johnson, M. *Analytical Biochemistry*, **1992**, *202* (2), 316–330.

(19) Gadella, T. W.; Jovin, T. M.; Clegg, R. M. *Biophysical Chemistry*, **1993**, *48* (2), 221–239.

(20) Hartmann, P.; Ziegler, W.; Holst, G.; Lübbers, D. W. *Sensors and Actuators B: Chemical*, **1997**, *38* (1-3), 110–115.

(21) Hartmann, P.; Ziegler, W. *Anal. Chem.*, **1996**, *68* (24), 4512–4514.

(22) Stahl, H.; Glud, A.; Schröder, C. R.; Klimant, I.; Tengberg, A.; Glud, R. N. *Limnol. Oceangr. Methods*, **2006**, *4*, 336–345.

(23) Meier, R. J.; Fischer, L. H.; Wolfbeis, O. S.; Schäferling, M. *Sensors and Actuators B: Chemical*, **2013**, *177*, 500–506.

(24) Babilas, P.; Schacht, V.; Liebsch, G.; Wolfbeis, O. S.; Landthaler, M.; Szeimies, R.-M.; Abels, C. *Br J Cancer*, **2003**, *88* (9), 1462–1469.

(25) Napp, J.; Behnke, T.; Fischer, L.; Würth, C.; Wottawa, M.; Katschinski, D. M.; Alves, F.; Resch-Genger, U.; Schäferling, M. *Anal. Chem.*, **2011**, *83* (23), 9039–9046.

(26) Lee, Y.-E. K.; Ulbrich, E. E.; Kim, G.; Hah, H.; Strollo, C.; Fan, W.; Gurjar, R.; Koo, S.; Kopelman, R. *Anal. Chem.*, **2010**, *82* (20), 8446–8455.

(27) Dmitriev, R. I.; Zhdanov, A. V.; Nolan, Y. M.; Papkovsky, D. B. *Biomaterials*, **2013**, *34* (37), 9307–9317.

(28) Ungerbock, B.; Charwat, V.; Ertl, P.; Mayr, T. *Lab Chip*, **2013**, *13* (8), 1593–1601.

(29) Gitlin, L.; Hoera, C.; Meier, R. J.; Nagl, S.; Belder, D. *Lab Chip*, **2013**, *13* (20), 4134–4141.

(30) Klimant, I.; Kühl, M.; Glud, R. N.; Holst, G. *3rd European Conference on Optical Chemical Sensors and Biosensors*, **1997**, *38* (1–3), 29–37.

(31) Schreml, S.; Meier, R. J.; Wolfbeis, O. S.; Landthaler, M.; Szeimies, R.-M.; Babilas, P. *Proceedings of the National Academy of Sciences*, **2011**, *108* (6), 2432–2437.

(32) Peng, H.-s.; Stolwijk, J. A.; Sun, L.-N.; Wegener, J.; Wolfbeis, O. S. *Angewandte Chemie*, **2010**, *122* (25), 4342–4345.

(33) Niethammer, P.; Grabher, C.; Look, A. T.; Mitchison, T. J. *Nature*, **2009**, *459* (7249), 996–999.

(34) Wu, M.; Lin, Z.; Schäferling, M.; Dürkop, A.; Wolfbeis, O. S. *Analytical Biochemistry*, **2005**, *340* (1), 66–73.

(35) Liebsch, G.; Klimant, I.; Frank, B.; Holst, G.; Wolfbeis, O. S. *appl spectrosc*, **2000**, *54* (4), 548–559.

(36) Mayr, T.; Igel, C.; Liebsch, G.; Klimant, I.; Wolfbeis, O. S. *Anal. Chem.*, **2003**, *75* (17), 4389–4396.

(37) Mayr, T.; Klimant, I.; Wolfbeis, O. S.; Werner, T. *Analytica Chimica Acta*, **2002**, *462* (1), 1–10.

(38) Iniya, M.; Jeyanthi, D.; Krishnaveni, K.; Mahesh, A.; Chellappa, D. *Spectrochimica Acta Part A: Molecular and Biomolecular Spectroscopy*, **2014**, *120* (0), 40–46.

(39) Peng, H.; Stich, M. I. J.; Yu, J.; Sun, L.-N.; Fischer, L. H.; Wolfbeis, O. S. *Adv. Mater.*, **2010**, *22* (6), 716–719.

(40) Filevich, O.; Etchenique, R. *Anal. Chem.*, **2006**, *78* (21), 7499–7503.

(41) Lebedev, A. Y.; Cheprakov, A. V.; Sakadzić, S.; Boas, D. A.; Wilson, D. F.; Vinogradov, S. A. *ACS Appl Mater Interfaces*, **2009**, *1* (6), 1292–1304.

(42) Rietveld, I. B.; Kim, E.; Vinogradov, S. A. *Recent Developments in Dendrimer Chemistry*, **2003**, *59* (22), 3821–3831.

(43) Baumes, J. M.; Gassensmith, J. J.; Giblin, J.; Lee, J.-J.; White, A. G.; Culligan, W. J.; Leevy, W. M.; Kuno, M.; Smith, B. D. *Nat Chem*, **2010**, *2* (12), 1025–1030.

(44) Sreejith, S.; Divya, K. P.; Ajayaghosh, A. *Angew. Chem. Int. Ed. Engl.*, **2008**, *47* (41), 7883–7887.

(45) McDonnell, S. O.; O'Shea, D. F. *Org. Lett.*, **2006**, *8* (16), 3493–3496.

(46) Borisov, S. M.; Zenkl, G.; Klimant, I. *ACS Appl. Mater. Interfaces*, **2010**, *2* (2), 366–374.

(47) Borisov, S. M.; Saf, R.; Fischer, R.; Klimant, I. *Inorg. Chem.*, **2013**, *52* (3), 1206–1216.

(48) Jokic, T.; Borisov, S. M.; Saf, R.; Nielsen, D. A.; Kühl, M.; Klimant, I. *Anal. Chem.*, **2012**, *84* (15), 6723–6730.

(49) Matray Tracy, Hernandez Vincent, Singh Sharat, United States Patent 6673550, *Electrophoretic tag reagents comprising fluorescent compounds*, 2002.

(50) Borisov, S. M.; Nuss, G.; Klimant, I. *Anal. Chem.*, **2008**, *80* (24), 9435–9442.

(51) Demas, J. N.; DeGraff, B. A.; Xu, W. *Anal. Chem.*, **1995**, *67* (8), 1377–1380.

(52) Ferguson, J. A.; Healey, B. G.; Bronk, K. S.; Barnard, S. M.; Walt, D. R. *Analytica Chimica Acta*, **1997**, *340* (1–3), 123–131.

(53) Wencel, D.; Higgins, C.; Klukowska, A.; MacCraith, B. D.; McDonagh, C. *Mater. Sci.-Pol.*, **2007**, *25* (3), 767–779.

(54) Stich, M. I. J.; Fischer, L. H.; Wolfbeis, O. S. *Chemical Society reviews*, **2010**, *39* (8), 3102–3114.

(55) Zelelow, B.; Khalil, G. E.; Phelan, G.; Carlson, B.; Gouterman, M.; Callis, J. B.; Dalton, L. R. *Sensors and Actuators B: Chemical*, **2003**, *96* (1-2), 304–314.

(56) Li, L.; Walt, D. R. *Anal. Chem.*, **1995**, *67* (20), 3746–3752.

(57) Weidgans, B. M.; Krause, C.; Klimant, I.; Wolfbeis, O. S. *Analyst*, **2004**, *129* (7), 645.

5.6 Supplementary Information

pO$_2$-sensors

PtTPTBPF/MFY in polystyrene

PET-foil

PdTPTBPF/MFY in polystyrene

PET-foil

PtTPTBPF/BTMHJBN in polystyrene

PET-foil

Poly(phenylsilsesquioxane) particles with PdTPTBPF in Teflon(R) AF 1600

PtTFPP/MFY in polystyrene

PET-foil

pH-sensor

aza-BODIPY in D4

BTMHJBN in polystyrene

PET-foil

pO$_2$/pH sensor

Polystyrene particles with PtTPTBPF, DCIFA and particles of pigment Brick red in hydrogel D4

PET-foil
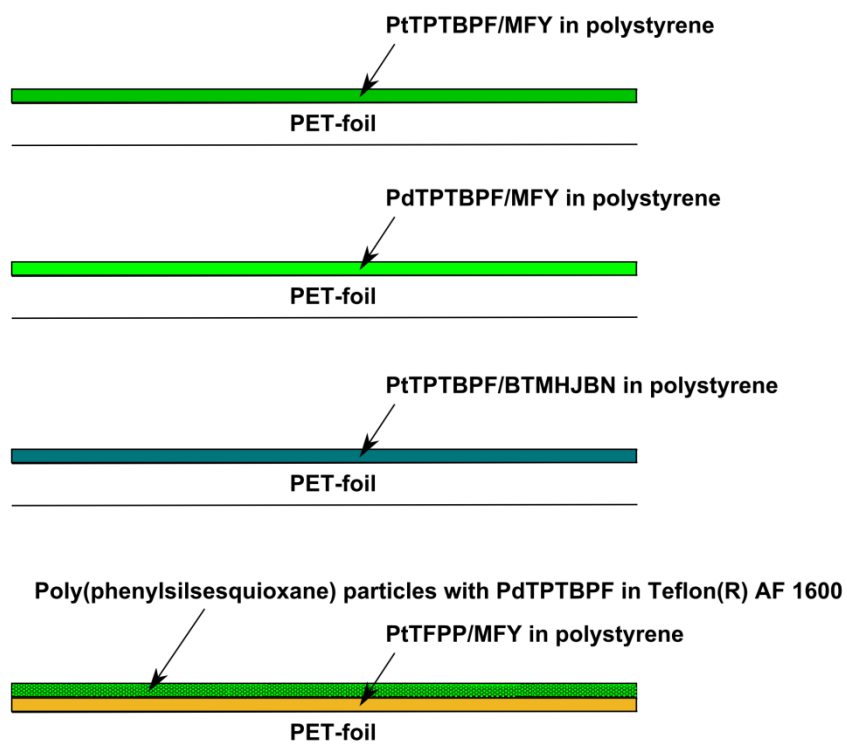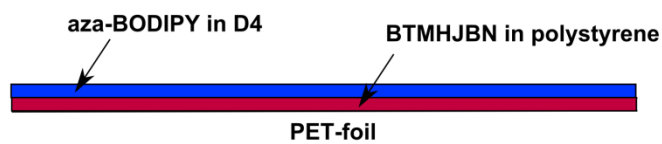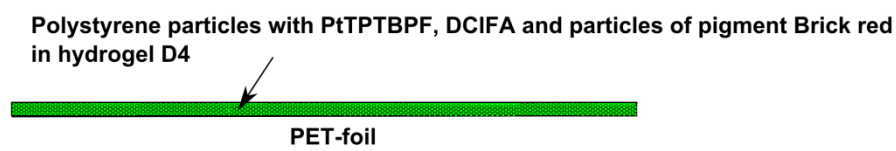
SI Figure 5.1 Schematic drawings of the different sensors are shown below.

5.6.1 Source Code of the MATLAB script

```matlab
%reads all '.tif'-Dateien of the folder and calculates the mean-value


close all
clear all

a=dir('*rgb*.tif');
b=dir('*nir*.tif');
% define dimensions of image
height = 966; % Pixel
width = 1296 % Pixel
depth = 4 % color channels plus nir channel
calculation=numel(a);%Dimension for saving of R-values
summe=zeros(height,width,depth);


% possibility to define region of interest
                % 1. Bild laden
    name='Folie1_0_pH3.56_rgb.tif'               %name=a(1).name;
    disp(name)
    % reads 3-dim-Matrix
    A=imread(name);
    A=double(A)./4096;
    A=A(:,:,2);



    % Bereich zur Auswertung manuell auswählen
    disp('Bereich zur Auswertung auswählen')
    [A_roi, xi, yi] = roipoly(A);


%     % Bereich zur Auswertung per Werte eingeben
%     xi = [213 220 262 306 361 407   433   424   394   359   310
263   226   213];
%     yi = [236.0000  285.0000  333.0000  352.0000  347.0000
314.0000 259.0000  204.0000  161.0000  140.0000  133.0000  150.0000
...
%          186.0000  236.0000];
%     imtau_roi = roipoly(im1, xi, yi);

    close;

    %create a txt file
myformat = '%45s %12s %12s %12s %12s %12s %12s %12s %12s %12s %12s
%12s %12s\r\n';
fid = fopen('results.txt','w');
fprintf(fid, myformat, 'Name            ', 'Grün/Rot1', 'Standardab.',
'NIR/Rot2', 'Standardab.', 'Grün', 'std', 'Rot1', 'std', 'Rot2',
'std', 'NIR', 'std');
fclose(fid);

%Matrix zum Speichern der R-Werte
ratio=zeros(height,width,calculation);
```

```matlab
%Matrix zum Speichern der NIR-Intensitäten
ratio2=zeros(height,width,calculation);

%return

for i=1:numel(a)
    name=a(i).name;
    disp(name)
    % reads 3-dim-Matrix
    A=imread(name);
    A=double(A);

     %read dark RGB image

    dunkel_RGB=imread('Blank_rgb.tif');
    dunkel_RGB=double(dunkel_RGB);

    %subtraction of dark RGB image
    A(:,:,1)=A(:,:,1)-dunkel_RGB(:,:,1);
    A(:,:,2)=A(:,:,2)-dunkel_RGB(:,:,2);
    A(:,:,3)=A(:,:,3)-dunkel_RGB(:,:,3);


    % extraction of color channels; usually red is channel 1, green
is 2,
    % blue is 3
    red1=A(:,:,3);
    red2=A(:,:,3)-A(:,:,2).*0.245;  %correction factor f= 0.245
    green=A(:,:,2);
    blue=A(:,:,1);



    name=b(i).name;
    disp(name)
    %reads 1-dim-Matrix
    A=imread(name);
    A=double(A);

    %read dark NIR image

    dunkel_NIR=imread('Blank_nir.tif');
    dunkel_NIR=double(dunkel_NIR);

    %subtraction of dark NIR image
    A(:,:,1)=A(:,:,1)-dunkel_NIR(:,:,1);

    % extraction of nir channel
    nir=A(:,:,1);

    % ratio: choose the channels you want to divide
    r=green./red1;
    r2=nir./red2;

    r_roi=A_roi.*r;
    r_roi2=A_roi.*r2;
```

```matlab
    ratio(:,:,i)=r_roi2;
    ratio2(:,:,i)=A_roi.*nir;




    % calculation of mean values and standard deviation. writes the
results
    % into vectors
    mean_r(i)=mean2(r_roi(find(r_roi > 0)));
    std_r(i)=std2(r_roi(find(r_roi > 0)));
    mean_r2(i)=mean2(r_roi2(find(r_roi > 0)));
    std_r2(i)=std2(r_roi2(find(r_roi > 0)));

    %calculate mean values of the nir, red and green channel
    s_green=A_roi.*green;
    s_red1=A_roi.*red1;   %s...signal
    s_red2=A_roi.*red2;
    s_nir=A_roi.*nir;

    mean_green(i)=mean2(s_green(find(s_green > 0)));
    mean_red1(i)=mean2(s_red1(find(s_red1 > 0)));
    mean_red2(i)=mean2(s_red2(find(s_red2 > 0)));
    mean_nir(i)=mean2(s_nir(find(s_nir > 0)));
    std_green(i)=std2(s_green(find(s_green > 0)));
    std_red1(i)=std2(s_red1(find(s_red1 > 0)));
    std_red2(i)=std2(s_red2(find(s_red2 > 0)));
    std_nir(i)=std2(s_nir(find(s_nir > 0)));


    %write the results from the vector into a txt file
    sname=['ratio_roi_',name(1:end-4),'.tif'];
    fid = fopen('results.txt','a');
    fprintf(fid,'%45s %12.4f %12.4f %12.4f %12.4f %12.1f %12.1f
%12.1f %12.1f %12.1f %12.1f %12.1f
%12.1f\r\n',sname,mean_r(i),std_r(i),mean_r2(i),std_r2(i),mean_green(
i),std_green(i),mean_red1(i),std_red1(i),mean_red2(i),std_red2(i),mea
n_nir(i),std_nir(i));
    fclose(fid);



    red1 = red1./4096;
    bwmaske=im2bw(red1,0.05);
    r=r.*bwmaske;
    r2=r2.*bwmaske;

    h1=figure;
            imshow(r);
            %title(imname);
            colormap(jet);
            caxis([0 3.6]);
            colorbar;

            sname=['ratio_roi_',name(1:end-4),'.tif'];
```

```matlab
            saveas(h1,sname);
            disp(['Gespeichert als: ',sname]);
            close(h1);

    h2=figure;
            imshow(r2);
            %title(imname);
            colormap(jet);
            caxis([0 2.5]);
            colorbar;

            sname=['ratio_roi2_',name(1:end-4),'.tif'];

            saveas(h2,sname);
            disp(['Gespeichert als: ',sname]);
            close(h2);


end

mw_r = mean_r'
std_r = std_r'
mw_r = mean_r2'
std_r = std_r2'


%create a txt file
myformat2 = '%45s %12s %12s %12s %12s\r\n';
fid2 = fopen('calibration.txt','w');
fprintf(fid2, myformat2, 'Name            ', 'R0/R', 'Standardab.',
'I0/I', 'Standardab.');
fclose(fid2);

for j=2:numel(a)
name=a(j).name;
disp(name)

Ra=ratio(:,:,2)./ratio(:,:,j);
Inten=ratio2(:,:,2)./ratio2(:,:,j);

mean_Ra(j)=mean2(Ra(find(Ra > 0.1)));
std_Ra(j)=std2(Ra(find(Ra > 0.1)));
mean_Inten(j)=mean2(Inten(find(Inten > 0.1)));
std_Inten(j)=std2(Inten(find(Inten > 0.1)));

%write the results from the vector into a txt file
sname=['ratio_roi_',name(1:end-4),'.tif'];
fid2 = fopen('calibration.txt','a');
fprintf(fid2,'%45s %12.4f %12.4f %12.4f
%12.4f\r\n',sname,mean_Ra(j),std_Ra(j),mean_Inten(j),std_Inten(j));
fclose(fid2);

end
```

"Science is a wonderful thing if one does not have to earn a living at it. One should earn one's living by work of which one is sure one is capable. Only when we do not have to be accountable to anyone can we find joy in scientific endeavor."

Albert Einstein

Part III

Co-authored publications in peer-reviewed journals

"Scissors cuts paper, paper covers rock, rock crushes lizard, lizard poisons Spock, Spock smashes scissors, scissors decapitates lizard, lizard eats paper, paper disproves Spock, Spock vaporizes rock, and as it always has, rock crushes scissors."

Sheldon Cooper

6 Co-authored publications in peer-reviewed journals

6.1 Enhanced and homogeneous oxygen availability during incubation of microfluidic droplets

Authors: Lisa Mahler, Miguel Tovar, Thomas Weber, Susanne Brandes, Martin M. Rudolph, **Josef Ehgartner**, Torsten Mayr, Marc T. Figge, Martin Roth, Emerson Zang

Comment The availability of oxygen is a crucial parameter in most microbial cultures because it affects the physiological state of cells and therefore the amount of produced biomass and proteins. Furthermore, the genotypic distinctiveness of cells is probably altered and different within microbial cultures if oxygen is not distributed uniformly within them. Microfluidic droplet techniques are emerging tools to culture and screen different types of cells. Despite the increasing use of these techniques only little is known about the actual oxygen concentration during droplet based cell culture experiments and how it actually influences the behaviour of cells. The published paper demonstrates the impact of oxygen availability during the incubation of biotechnological relevant microorganisms in microfluidic droplets. The publication features a 3D-printed storage device which was used to incubate the droplets with cells enclosed under defined conditions.

  My scientific contribution to this publication was the preparation and characterization of oxygen nanosensors, which were used to monitor the average oxygen concentration within the microfluidic droplets in the incubation device. Another contribution from my side was the training of other researchers in how to use the nanosensors and how to perform the oxygen measurements reliably. In detail, the nanosensors were based on poly(styrene-block-vinylpyrrolidone) nanoparticles and were stained with an oxygen indicator dye (PtTPTBPF) similar as described in chapter 4.2.2. The nanosensors were calibrated at different temperatures and in addition the influence of fluorinated solvents on the sensor performance was investigated. Fluorinated solvents are commonly used to generate microfluidic droplets and to supply the cells within droplets with oxygen. Quantitative analysis of oxygen by the nanosensors was possible and realized within this publication. The nanosensors visualized the oxygen concentrations and showed how the different culturing protocols affect the oxygen availability in the incubation device.

6.2 A microfluidically perfused three dimensional human liver model

Authors: Knut Rennert, Sandra Steinborn, Marko Gröger, Birgit Ungerböck, Anne-Marie Jank, **Josef Ehgartner**, Sandor Nietzsche, Julia Dinger, Michael Kiehntopf, Harald Funke, Frank T. Peters, Amelie Lupp, Claudia Gärtner, Torsten Mayr, Michael Bauer, Otmar Huber, Alexander S. Mosig

Comment Mimicking of organs and their functions for *in vitro* studies is an interesting challenge that fascinates many scientists around the world as it has the potential to revolutionize drug testing. Microfluidic devices called organs-on-chips have evolved in recent years to helpful tools and helped moving this challenge on step closer to the goal. However, organs-on-chips are still in their infancy and lots of tasks are waiting to be solved by researchers [1,2]. A sub-category of organs-on-chips, namely liver-on-chip deals with the development of liver organoids which should show the characteristic liver functions such as detoxification, protein production or glycogen storage [2]. Unfortunately, the liver has a complex structure and its functions are hard to mimic and to maintain in *in vitro* studies. The published paper demonstrates a new microfluidic platform for studying human hepatocellular physiology at a cellular level under conditions close to the physiological situation. Hopefully, this three dimensional human liver model can contribute to the advancement of this promising field.

  My scientific contribution to the publication was the preparation and characterization of integrated oxygen sensors, which consisted of a polystyrene matrix and a physically entrapped oxygen indicator dye (PtTPTBPF). The sensors were integrated by an airbrush spraying technique similar to that explained in chapter 3.2.2. The sensors were integrated into microfluidic biochips before the chip bonding process. The biochips were manufactured and bonded by microfluidic ChipShop GmbH (Jena, Germany), and were made from cyclic olefin copolymer. A simple chip holder and spraying stencils were designed and manufactured in-house for accurate and reproducible integration of the sensor spots within the biochip. The spraying stencils were made from polyethylene terephthalate foils and were tailored to the appropriate shape by a cutting plotter. The oxygen sensors were used to online monitor the cellular oxygen consumption of the whole liver organoid and allowed the assessment of the cellular activity. The sensors have proven their usefulness and are valuable tools for different kinds of cellular investigations where oxygen plays a role.

6.3 Fast pesticide detection inside microfluidic device with integrated optical pH, oxygen sensors and algal fluorescence

Authors: Islam B. Tahirbegi, **Josef Ehgartner**, Philipp Sulzer, Silvia Zieger, Alice Kasjanow, Mirco Paradiso, Martin Strobl, Dominique Bouwes, Torsten Mayr

Comment Pesticides are unloved necessities for the protection of our crops. Unfortunately, the misuse of those chemicals often exhibits severe environmental risks or even health risks to local inhabitants of different species especially in less regulated developing countries. The precise identification and quantification of pesticide is therefore an indispensable analytical task and is usually performed by chromatographic techniques such as HPLC/MS or GC/MS. In addition to these techniques, portable, fast, easy to handle and cheap pesticide detection platforms are necessary in order to assess the risk of a contamination or even a health hazard as soon as possible. One possible approach to achieve this analytical challenge could be the use of algal biosensors. Algae are aquatic photosynthetic organisms that consume carbon dioxide and produce and release oxygen during photosynthesis. Pesticides can show acute toxicity to algae and can block their photosynthetic pathways. Therefore, the combination of a unicellular freshwater algal species (*Chlamydomonas reinhardtii*) incorporated within a glass based microfluidic device with integrated oxygen and pH sensors forms a promising biosensing platform for pesticides. Glass is preferred as chip material because it is nontoxic for algae and impermeable for gases because the unwanted releases of gases into the microfluidic channel negatively affects the sensor performance.

  My scientific contribution to this publication was the development of oxygen and pH sensors suitable for integration within glass based microfluidic devices. The sensing chemistry of the oxygen sensor is discussed in detail in chapter 3. The integration protocol of the pH sensor which also contains a silanization step of the glass surface with APTES was based on a former developed unpublished protocol. The obtained biosensor was used for the detection of photosynthesis blocking pesticides in the nanomolar concentrate range. The presence of pesticides in tap water can be determined within two minutes by monitoring the photosynthetic oxygen production rate and the increase of the pH value because of the consumed carbon dioxide. The biosensor set-up should be seen as a promising starting point for further developments in this area in the future.

6.4 Ratiometric oxygen imaging to predict oxygen diffusivity in oak wood during red wine barrel aging

Authors: Ignacio Nevares, Torsten Mayr, Jesus Angel Baro, **Josef Ehgartner**, Raul Crespo, María del Alamo-Sanza

Comment Oxygen plays an ambivalent role during the winemaking process because on one hand it is needed especially during the early stages of the fermentation process and on the other hand it can have negative effects on the colour or on the flavour of a wine. Therefore, the controlled exposure of a wine to oxygen is of great importance for a winemaker. Oxygen intake into wooden wine barrels occurs not only through tiny gaps between the planks of a barrel but also by permeation of oxygen through the wood. It is a well-known fact in oenology that oxidation of wine occurs during the storage in oak barrels. However, less is known about the oxygen diffusivity of oak wood and how it is effected by the moisture content of the wood which typically increases during the wine aging process because of the prolonged contact time between wine and wood. Luminescent oxygen sensors are useful tools for studying these changes in oxygen diffusivity in oak wood because they allow the spatially resolved determination (imaging) of oxygen and thus provide insights into the wine barrel aging processes.

  My scientific contribution to this publication was the preparation and characterisation of the oxygen sensing films, the supply of a MATLAB script for data evaluation, explanations on how to use the sensing films and assistance in setting up the imaging system. The publication shows the useful application of sensing films similar to those such as presented in chapter 5. The sensing films consisted of an oxygen indicator dye (PdTFPP), a reference dye (MACROLEX® fluorescent yellow) and a polystyrene matrix. Both dyes were physically entrapped within the matrix. The films were fabricated by knife coating. A layer made from ELASTOSIL® E4 silicon rubber was knife coated on top of the sensing layer in order to protect the dyes from being leached out by ethanol. The sensor film visualized the change in the oxygen concentration during a simulated wine aging process of 125 days. This data provided useful information in how the oxygen diffusivity of the wine barrel is influencing by the moisture content.

6.5 List of abbreviations

APTES	(3-Aminopropyl)triethoxysilane
GC	Gas chromatography
HPLC	High performance liquid chromatography
MS	Mass spectrometry
PdTFPP	Palladium(II)-5,10,15,20-tetrakis-(2,3,4,5,6-pentafluorphenyl)-porphyrin
PtTPTBPF	Platinum(II) *meso*-tetra(4-fluorophenyl) tetrabenzoporphyrin

6.6 References

(1) Bhatia, S. N.; Ingber, D. E. *Nature biotechnology*, **2014**, *32* (8), 760–772.

(2) Zheng, F.; Fu, F.; Cheng, Y.; Wang, C.; Zhao, Y.; Gu, Z. *Small*, **2016**, *12* (17), 2253–2282.

"The highest forms of understanding we can achieve are laughter and human compassion."

Richard P. Feynman

7 Summary and conclusion

Sensors are urgently needed in microfluidics in order to monitor and control important process parameters at this miniaturized scale. The presented thesis demonstrates different sensor systems that achieved this goal for the two key parameters dissolved oxygen and pH, which are of great importance especially in cell based applications for monitoring and controlling the cell growth. The first presented system enables dissolved oxygen measurements within microfluidic platforms and is based on a measurement set-up consisting of integrated oxygen sensor films and an inexpensive and robust readout device that allows luminescent lifetime measurements in the frequency domain. The set-up enables the determination of oxygen up to a resolution of 0.06-0.22 hPa (approx. 3-9 µg/L of dissolved oxygen). An adapted version of this system was used to determine dissolved oxygen concentrations in a liver-on-a-chip platform. A further development of this set-up allows the determination of oxygen and pH and was used in a microfluidic biosensor for pesticide detection. The second presented system consisted of oxygen and pH nanosensors and a read-out device that enables simultaneous sensing of pH and oxygen by using a modified dual lifetime referencing algorithm. Oxygen concentrations can be determined at a resolution of 0.5-8.0 hPa (approx. 0.02-0.32 mg/L of dissolved oxygen) depending on the oxygen levels. The pH value can be determined at a resolution of 0.03-0.1 pH units within the dynamic range (apparent pK_a' 7.23 ± 1.0) of the pH nanosensors. The apparent pK_a' (7.2±0.1) is in the physiological range which is an interesting region for various applications, e.g. cell based microfluidic assays or organs-on-chips. The nanosensors were applied to study the impact of oxygen availability during the incubation of biotechnological relevant microorganisms in microfluidic droplets. The third presented system is capable of ratiometric imaging of oxygen, pH and both parameters simultaneous and consists of planar sensor films and a 2-CCD colour near infrared camera. The obtained knowledge during developing this set-up was applied for ratiometric oxygen imaging to predict the oxygen diffusivity of oak wood during red wine barrel aging. All presented set-ups were valuable tools for other researchers and allowed them to answer scientifically relevant questions. The development of these existing systems has not come to an end now and more work will be necessary to improve and adapt them for other applications. Besides this, other exciting sensing tasks such as the determination of glucose, lactate, potassium or sodium are waiting to be solved by luminescent chemical sensors in a robust and reliable way. The way to achieve this is probably meandering and more time consuming than thought however, science is similar to life a journey full of surprises with a hopefully satisfying outcome no matter how this will look like for each individual.

"The belief that one's own view of reality is the only reality is the most dangerous of all delusions."

Paul Watzlawick

Part IV

Appendix

MATLAB program to read out text files from Piccolo measurements

```matlab
% liest Daten aus piccolo file ein

dirdata=dir('*.txt');
dirsize=size(dirdata);
disp(dirsize)
disp(dirsize(1))
disp(dirdata(1).name)
disp(dirdata)


    %create a txt file
myformat = '%75s %20s %20s %20s %20s %20s %20s %20s %20s %20s %20s
%20s %20s %20s %20s\r\n';
fid = fopen('results.txt','w');
fprintf(fid, myformat, 'Name              ', 'dphi_Freq_1',
'Std_dphi_Freq_1', 'Int_Freq_1', 'Std_Int_Freq_1','dphi_Freq_2',
'Std_dphi_Freq_2', 'Int_Freq_2', 'Std_Int_Freq_2','dphi_Freq_A',
'Std_dphi_Freq_A', 'A', 'Std_A', 'B', 'Std_B' );
fclose(fid);


%.txt Öffnen öffnen
if (size(dirdata)>0)
    for i=1:dirsize(1)
        imname=dirdata(i).name;
        fid=fopen(imname);
        disp(['--------',imname]);


        %Suchen und Abspeichern der gewollten Werte aus .txt Datei
            [Y1,Y2,Y3,Y4,Y5,Y6,Y7,Y8]=textread(imname,'%f %f %f %f
    %f %f %f %f');


        %Dimensonen für Bildmatrix bestimmen
        s=size(Y1,1)

        x=[1:s];


        % Generating example 2-D plot
        hfig = figure;
        hax = axes;
        xdata = Y1;
        ydata = Y4;
        hline = line(xdata,ydata,'Marker','.');
        datacursormode on;
        dcm_obj = datacursormode(hfig);
```

```matlab
        h = msgbox('Enter drücken um fortzufahren');

        pause

        %Box für ROI-Eingabe
        prompt={'Anzahl der ROIs eingeben:'};
        name='ROIs';
        numlines=1;
        defaultanswer={'5'};
        answer=inputdlg(prompt,name,numlines,defaultanswer);
        Anzahl = str2num(answer{1});




        %Auswertung der ROIs

        for k=1:Anzahl

            %Box für Anzeige
        prompt={'Click line to display a data tip, then press
return.'};
        answer=msgbox(prompt);
        pause;


        info_struct = getCursorInfo(dcm_obj);
        value = getfield(info_struct, 'DataIndex');


        prompt={'Click line to display a data tip, then press
return.'};
        answer=msgbox(prompt);
        pause;


        info_struct2 = getCursorInfo(dcm_obj);
        value2 = getfield(info_struct2, 'DataIndex');

        A1=Y2(value:value2);
        A2=Y3(value:value2);
        A3=Y4(value:value2);
        A4=Y5(value:value2);
        A5=Y6(value:value2);
        A6=Y7(value:value2);
        A7=Y8(value:value2);
```

```matlab
        mean_dphi1=mean(A1);
        std_dphi1=std(A1);

        mean_Int1=mean(A2);
        std_Int1=std(A2);

        mean_dphi2=mean(A3);
        std_dphi2=std(A3);

        mean_Int2=mean(A4);
        std_Int2=std(A4);

        mean_dphiA=mean(A5);
        std_dphiA=std(A5);

        mean_A=mean(A6);
        std_A=std(A6);

        mean_B=mean(A7);
        std_B=std(A7);


        %write the results from the vector into a txt file
         sname=[imname(1:end-4),'.txt'];
         fid = fopen('results.txt','a');
         fprintf(fid,'%75s %20.4f %20.4f %20.4f %20.4f %20.4f
%20.4f %20.4f %20.4f %20.4f %20.4f %20.4f %20.4f
%20.4f\r\n',...
         sname,mean_dphi1, std_dphi1, mean_Int1, std_Int1,
mean_dphi2, std_dphi2, mean_Int2,std_Int2, mean_dphiA, std_dphiA,
mean_A, std_A, mean_B, std_B);
         fclose(fid);




    end

   print(hfig,'-dtiff',imname(1:end-4));


   close(hfig);

  end


end


fclose('all');
```

List of publications

Articles in peer-reviewed journals

Ehgartner, Josef; Strobl, Martin; Bolivar, Juan M.; Rabl, Dominik; Rothbauer, Mario; Ertl, Peter; Borisov, Sergey M.; Mayr, Torsten: Simultaneous determination of oxygen and pH inside microfluidic devices using core-shell nanosensors. Currently accepted in *Analytical Chemistry*. DOI: 10.1021/acs.analchem.6b02849.

Alamo-Sanz, María del; Nevares, Ignacio; Mayr, Torsten; Baro, Jesus Angel; Martínez-Martínez, Victor; **Ehgartner, Josef**: Analysis of the role of wood anatomy on oxygen diffusivity in barrel staves using luminescent imaging. In press: *Sensors and Actuators B*: Chemical. DOI: 10.1016/j.snb.2016.08.075.

Tahirbegi, I.Bogachan; **Ehgartner, Josef**; Sulzer, Philipp; Zieger, Silvia; Kasjanow, Alice; Paradiso, Mirco et al. (2016): Fast pesticide detection inside microfluidic device with integrated optical pH, oxygen sensors and algal fluorescence. In press: *Biosensors and Bioelectronics*. DOI: 10.1016/j.bios.2016.08.014.

Nevares, Ignacio; Mayr, Torsten; Baro, Jesus Angel; **Ehgartner, Josef**; Crespo, Raul; Alamo-Sanza, María (2016): Ratiometric Oxygen Imaging to Predict Oxygen Diffusivity in Oak Wood During Red Wine Barrel Aging. In: *Food and Bioprocess Technology*, S. 1–11.

Ehgartner, Josef; Sulzer, Philipp; Burger, Tobias; Kasjanow, Alice; Bouwes, Dominique; Krühne, Ulrich et al. (2016): Online analysis of oxygen inside silicon-glass microreactors with integrated optical sensors. In: *Sensors and Actuators B: Chemical* 228, S. 748–757.

Rennert, Knut; Steinborn, Sandra; Gröger, Marko; Ungerböck, Birgit; Jank, Anne-Marie; **Ehgartner, Josef** et al. (2015): A microfluidically perfused three dimensional human liver model. In: *Biomaterials* 71, S. 119–131.

Mahler, Lisa; Tovar, Miguel; Weber, Thomas; Brandes, Susanne; Rudolph, Martin Michael; **Ehgartner, Josef** et al. (2015): Enhanced and homogeneous oxygen availability during incubation of microfluidic droplets. In: *RSC Adv* 5 (123), S. 101871–101878.

Lasave, Liliana C.; Borisov, Sergey M.; **Ehgartner, Josef**; Mayr, Torsten (2015): Quick and simple integration of optical oxygen sensors into glass-based microfluidic devices. In: *RSC Adv* 5 (87), S. 70808–70816.

Ehgartner, Josef; Wiltsche, Helmar; Borisov, Sergey M.; Mayr, Torsten (2014): Low cost referenced luminescent imaging of oxygen and pH with a 2-CCD colour near infrared camera. In: *The Analyst* 139 (19), S. 4924–4933.

Glabonjat, Ronald A.; Raber, Georg; Jensen, Kenneth B.; **Ehgartner, Josef**; Francesconi, Kevin A. (2014): Quantification of arsenolipids in the certified reference material NMIJ 7405-a (Hijiki) using HPLC/mass spectrometry after chemical derivatization. In: *Analytical chemistry* 86 (20), S. 10282–10287.

Oral presentations

Ehgartner, J*; Strobl, M.; Sulzer, P.; Tahirbegi, I. B.; Kasjanow, A.; Ungerböck, B.; Rennert, K.; Mosig, A. S.; Mayr T.: Online analysis of oxygen and pH inside microfluidics with integrated optical sensors. – At: 12th ASAC JunganalytikerInnenforum. Graz, Austria on: 10.06.2016.

Ungerböck, B.*; Rennert K.; Keune, N.; Sulzer, P.; **Ehgartner J**.; Peters, S.; Dimitriev, R. I.; Borisov, S. M.; Mayr, T.; Mosig, A.S.; Gärtner, C.: Oxygen-sensor-enhanced Microfluidic Devices: Flexible Tools for Organ-on-a-chip Applications. – At: XIII EUROPT(R)ODE Conference on Optical Chemical Sensors & Biosensors. Graz, Austria on: 22.03.2016.

Del Alamo-Sanza, M.; Mayr, T.; Bar´o, J. A.*; **Ehgartner, J.**; Crespo, R.; Nevares, I.: Oxygen Imaging within a Barrel Oak Stave. Revealing the Key Factor in the Evolution of Oxygen Diffusivity in Oak Wood. – At: XIII EUROPT(R)ODE Conference on Optical Chemical Sensors & Biosensors. Graz, Austria on: 23.03.2016.

Ehgartner, J*; Strobl, M.; Sulzer, P.; Kasjanow, A.; Ungerböck, B.; Rennert, K.; Mosig, A. S.; Mayr T.: Online analysis of oxygen and pH inside microfluidics with integrated optical sensors. – At: Pre-conference 11th Workshop on Biosensors & Bioanalytical Microtechniques in Environmental, Food & Clinical Analysis. Regensburg, Germany on: 27.09.2015.

Mayr, T.*; **Ehgartner, J.**; Müller, B.; Ungerböck, B.: Strategies for application and integration of optical chemical sensors in microfluidic devices. - At: 7th Workshop of Chemical and Biological Micro Laboratory Technology. Ilmenau, Germany on: 25.02.2014.

Poster presentations

Ehgartner, J.*; Strobl, M.; Sulzer, P.; Kasjanow, A.; Bouwes, D.; Ungerböck, B.; Rennert, K.; Mosig, A. S.; Mayr, T.: Online analysis of oxygen and pH inside microfluidics with integrated optical sensors. At: XIII EUROPT(R)ODE Conference on Optical Chemical Sensors & Biosensors. Graz, Austria on: 20.-23.03.2016.

Gruber, P.*; Marques, M. P. C.; **Ehgartner, J.**; Mayr, T.; Baganz, F.; Szita, N.: Application of Optical pH Sensors for Reaction Monitoring in a Multi-Input Microfluidic Device. At: XIII EUROPT(R)ODE Conference on Optical Chemical Sensors & Biosensors. Graz, Austria on: 20.-23.03.2016.

Lasave, L. C.*; Borsiov, S. M.; **Ehgartner, J.**; Mayr, T.: A Versatile Approach for Integration of Oxygen Sensors into Glass-based Microfluidic Devices. At: XIII EUROPT(R)ODE Conference on Optical Chemical Sensors & Biosensors. Graz, Austria on: 20.-23.03.2016.

Tahirbegi, I. B.*; Kasjanow, A.; Paradiso, M.; **Ehgartner, J.**; Mayr, T.; Bouwes, D.: Sensitivity enhancement of optical sensors by microlenses inside microfluidics. At: XIII EUROPT(R)ODE Conference on Optical Chemical Sensors & Biosensors. Graz, Austria on: 20.-23.03.2016.

Fernandes, A. C.*; **Ehgartner, J.**; Semenova, D.; Mayr, T.; Sesay, A. M.; Gernaey, K. V.; Krühne, U.: Sensor integration in microbioreactor systems for high performance processes. At: XIII EUROPT(R)ODE Conference on Optical Chemical Sensors & Biosensors. Graz, Austria on: 20.-23.03.2016.

Ehgartner, J.*; Strobl, M.; Sulzer, P.; Kasjanow, A.; Ungerböck, B.; Rennert, K.; Mosig, A. S.; Mayr, T.: Online analysis of oxygen and pH inside microfluidics with integrated optical sensors. – At: 11th Workshop on Biosensors & Bioanalytical Microtechniques in Environmental, Food & Clinical Analysis. Regensburg, Germany on: 28.09.2015.

Ehgartner, J.*; Mayr, T.; Sulzer, P.; Müller, B.; Zorn, P. J.; Ungerböck, B.; Schulz, I.; Kasjanow, A.; Bouwes, D. M.; Krühne, U.: Chemische optische Sensoren zur Bestimmung des Sauerstoffgehalts und des pH-Werts in der Mikrofluidik. – At: ANAKON 2015. Graz, Austria on: 25.03.2015.

Müller, B.*; Jokic, T.; Strobl, M.; **Ehgartner, J.**; Ungerböck, B.; Mayr, T.: Luminescent pH- and oxygen sensitive nanobeads for microfluidic systems. At: XII EUROPT(R)ODE Conference on Optical Chemical Sensors & Biosensors. Athens, Greece on: 13.04.2014.

Ehgartner, J.*; Wiltsche, H.; Borisov, S.; Mayr, T.: Low cost referenced luminescent imaging with 2-CCD color-near infrared cameras. At: XII EUROPT(R)ODE Conference on Optical Chemical Sensors & Biosensors. Athens, Greece on: 13.04.2014.

Müller, B.*; **Ehgartner, J.**; Strobl, M.; Ungerböck, B.; Sulzer, P.; Mayr, T.: Nanosensor Particles for the Application in Microfluidics. At: 7th Workshop Chemical and Biological Micro Laboratory Technology. Illmenau, Germany on: 25.02.2014.

Ehgartner, J.*; Ungerböck, B.; Fellinger, J.; Sulzer, P.; Mayr, T.: Magnetic Sensor Particles: A new tool for the determination of oxygen in microfluidics. At: MICROTAS - 17th International Conference on Miniaturized Systems for Chemistry and Life Sciences. Freiburg, Germany on: 27.10.2013.

List of figures

List of tables

"In the end, it's not the years in your life that count. It's the life in your years."

Abraham Lincoln

Curriculum vitae

CV JOSEF EHGARTNER

Date of birth: 29.08.1985
Address: SCHÖRGELGASSE 13 I 8010 GRAZ I ÖSTERREICH
E-Mail: josefehgartner1@gmail.com
Phone: 0043 664 2259624

+ CURRENT OCCUPATION

05/2013 - University project assistant (Ph.D. position) at the Institute of Analytical Chemistry and Food Chemistry Graz University of Technology (TUG), Austria.
Ph.D. thesis: Development of luminescent oxygen and pH sensors for microfluidic applications.
Tasks: *Development of sensor systems and analytical measurement procedures for microfluidic devices in collaboration with industrial and academic partners. Drafting of scientific reports and papers. Presentation of research results at conferences and at European project meetings. Supervision of trainees, students and other employees.*

+ EDUCATION

10/2009 - 04/2013 M.Sc. in chemistry, master program at TUG
Master's thesis: *Evaluation of extraction procedures for arsenolipids in algae & growing the unicellular alga Dunaliella tertiolecta in batch cultures.*

03/2006 - 09/2009 B.Sc. in chemistry, bachelor program at TUG.

07/2005 - 02/2006 Military service, emergency medical technician.

09/2000 - 06/2005 Higher Technical Institute for civil engineering in Zeltweg, Austria.

+ ABROAD RESEARCH EXPERIENCE

07/2015 Centre of Applied Photonics INESC TEC, Porto, Portugal, *Advanced Study Course on Optical Chemical Sensors and Biosensors (ASCOS 2015).*

04/2012 - 08/2012 University of Canberra, Australia, *Growing of unicellular algae for speciation of arsenolipids and nutrient analysis of the algal media.*

06/2010 - 08/2010 Syracuse University, USA, *Summer school in the field of theoretical chemistry.*

+ TEACHING EXPERIENCE

2014 - Mentoring of project laboratories, bachelor and master theses.

2013 - Teaching assistant for laboratory courses in Analytical chemistry at TUG.

10/2011 - 02/2013 Teaching assistant during the winter semesters for General chemistry at University of Graz.

CV JOSEF EHGARTNER

Date of birth: 29.08.1985
Address: SCHÖRGELGASSE 13 I 8010 GRAZ I ÖSTERREICH
E-Mail: josefehgartner1@gmail.com
Phone: 0043 664 2259624

+ ADDITIONAL WORKING EXPERIENCE (only for Analytical Chemistry)

08/2008 & 08/2009 Trainee at the QLM - Qualitätslabor St. Michael
Tasks: *Microbiological tests and analysis of drinking water and waste water.*

+ PROGRAMMING I SOFTWARE

C ++ I FORTRAN I MATLAB I LabVIEW
Solid Works I AutoCAD I ArchiCAD
Gaussian I ORCA
Photoshop
MS Office

+ LANGUAGES

German - Native
English - C1
Spanish- A1

+ SOCIAL ACTIVITIES

2011 - 2012 Staff member of the students' union at TUG and responsible for social grants.

2009 - 2011 Vice chairman of the students' union at TUG and responsible for e.g. social affairs, internal communication, HTU GmbH, senate at TUG etc.

2006 - 2009 Staff member of the student representation Chemistry.

2005 - 2010 Emergency medical technician at the Austrian Red Cross.

2000 - 2007 Voluntary work at the parish Judenburg St. Nikolaus.

+ SCIENTIFIC INTERESTS

Chemistry I Analytical Chemistry I Microfluidics I Mass spectrometry I Optical Sensors I Liquid chromatography I Dye synthesis I Product development I Metabolomics I Drug targeting I Environmental science I Life sciences

+ PERSONAL INTERESTS

science I hiking I reading I climbing I cooking I running I swimming I photography I relaxing I soccer I traveling I social projects I politics I friendships I family